UNDERSTANDING THE EARLY STAGE OF CLUSTER FORMATION

A Dissertation

Submitted to the Faculty

of

Purdue University

by

Ke Shi

In Partial Fulfillment of the

Requirements for the Degree

of

Doctor of Philosophy

May 2019

Purdue University

West Lafayette, Indiana

THE PURDUE UNIVERSITY GRADUATE SCHOOL
STATEMENT OF DISSERTATION APPROVAL

Dr. Kyoung-Soo Lee, Chair

Department of Physics and Astronomy

Dr. Dimitrios Giannios

Department of Physics and Astronomy

Dr. John Peterson

Department of Physics and Astronomy

Dr. Paul F. Muzikar

Department of Physics and Astronomy

Approved by:

Dr. John Finley

Department of Physics and Astronomy

To my beloved Mom and Dad. Thank you for your love and support throughout my life.

ACKNOWLEDGMENTS

I would like to thank my advisor Dr. Kyoung-Soo Lee for her continuous support during my Ph.D study, who helped me a lot in thinking and writing like a scientist besides taught me knowledge in this field. This thesis owes a great deal to her guidance.

TABLE OF CONTENTS

LIST OF TABLES

LIST OF FIGURES

ABSTRACT

Shi, Ke PhD, Purdue University, May 2019. Understanding the early stage of cluster formation. Major Professor: Kyoung-Soo Lee.

Understanding the formation and evolution of galaxies is a crucially important task in modern astronomy. It is well known that galaxy formation is strongly affected by the environments they reside in. Galaxy clusters, as the densest large-scale structures in the Universe, thus serve as ideal laboratories to study how galaxy formation proceeds in dense environments. Clusters already began to form at $z > 2$, therefore to directly witness the early stage of galaxy formation in dense environments, it is necessary to identify progenitors of clusters ('protoclusters') and study their galaxy constituents within. In this thesis, I present two observational studies on high-redshift protoclusters at $z > 3$. Utilizing multiwavelength data and different galaxy selection techniques, significant galaxy overdensities are found in the two protoclusters, which are predicted to evolve into Coma-like clusters by present day. Various types of galaxies are identified in the protocluster, such as normal star-forming galaxies, massive quiescent galaxies and post-starburst galaxies. Together with extreme and rare sources such as giant Lyman-alpha nebulae and brighest cluster galaxy, they paint a picture of how different galaxy populations trace the underlying dark matter halos. Finally, the environmental impact on galaxy properties appears to be a subtle one for these protoclusters, which might depend on the galaxy population one chooses to study.

1. INTRODUCTION

1.1 A Brief History of the Universe

Our Universe started with a Big Bang in about 13.7 billion years ago. The earliest stage known as the Planck epoch lasted for about 10^{-43} seconds, during which the electromagnetic, weak and strong interactions are assumed to be unified with gravitation. After this epoch, gravitation was separated from the other forces and cosmic inflation [1–4] took place at $\sim 10^{-36}$ seconds. During the inflation epoch, the Universe expanded exponentially in a very short time period. The quantum fluctuations in this epoch were thus magnified to cosmic size, which became the seeds for later structure formation in the Universe.

The early Universe was extremely hot, with various kinds of elementary particles emerging and interacting with one another, forming into a "primeval soup" where the matter and radiation were strongly coupled. As the expansion went on, the Universe became less hotter. At about 375,000 years, the Universe cooled down to allow neutral atoms to form ("recombination" [5]). Photons were decoupled from other particles and the Universe became transparent for the first time. These photons then travelled freely in the Universe and are detected today as the well-known cosmic microwave background (CMB) [6].

From the CMB epoch till about several hundred million years, before the first stars were born, there were no sources of light besides the decoupled photons and the Universe looked dark in this epoch known as the "Dark Ages".

Around 400 million years [7], the first generations of stars formed, and subsequently galaxies have emerged. Galaxies formed in a hierarchical bottom-up way; When the density contrast reaches a threshold value, the matter overcomes the expansion of the Universe and collapses into a bound system via gravitational instability (Jeans instability [8]). They began as relatively small systems, and subsequently grew larger via accretion and mergers [9]. Clusters were formed as gravitational force brought galaxies together, and later became virialized systems.

The majority of the matter ($\sim$85%) in the Universe, however, is unseen from us as it doesn't interact with electromagnetic radiation and is thus invisible in the entire electromagnetic spectrum. This "dark matter" is thought to be non-baryonic in nature and have profound impact on structure formation. This is because on one hand, dark matter has the largest mass budget. On the other hand, unlike ordinary matter, dark matter is not affected by radiation and its density fluctuations would not be washed out by the dominant radiation force in the early Universe. Therefore, the gravitational potential from dark matter acts as a potential well for ordinary matter to fall in and form stars and galaxies.

The expansion of the universe is expected to slow down in a matter-dominated universe. However, observations of distant supernovae [10, 11] showed that the universe is currently accelerating owing to an element known as *dark energy* supplying negative pressure. Its nature remains unknown, with the simplest explanation being the "cosmological constant" model, and contributes $\sim$68% of the total energy in the present-day Universe [12].

The domination of dark energy and dark matter in the Universe leads to the current standard model of the Universe, known as the "ΛCDM" model, which serves as a framework for majority studies in galaxies and clusters. Fig. 1.1 summarizes the timeline of the Universe.

1.2 A Brief Introduction to Galaxy Formation and Evolution

1.2.1 Hierarchical Structure Formation

Understanding the formation and evolution of galaxies is a crucially important subject in modern astronomy and astrophysics. As mentioned in the previous section, structures like galaxies and clusters form in a hierarchical manner. Small density

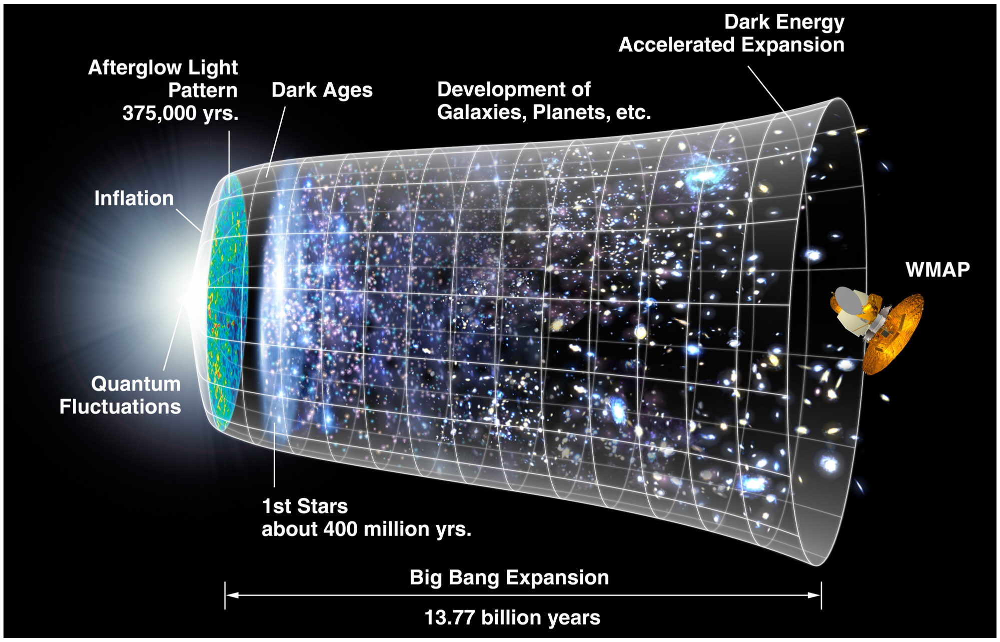

Fig. 1.1. This figure illustrates the evolution of the Universe from the Big Bang to the present. Credit: NASA / WMAP Science Team.

perturbations grow into nonlinear regime and break away from the cosmic expansion, collapsing into self-gravitating systems known as “dark matter halos”.

It is possible to use computer simulations to study how clusters and large-scale structures form. Fig. 1.2 illustrates the formation of large-scale filaments in the ΛCDM model. The frames show the evolution of structures in a 140 million light years box from redshift $z = 30$ to the present day. Initially at $z = 30$, when the age of the Universe was less than 1% of its current age, matter is uniformly distributed all over the place when the density fluctuations are still very small. Over time, the fluctuations grow larger, resulting in a wealth of structures from the smallest bright clumps which have sizes similar to those of galaxies to the large filaments. The filaments become more pronounced over time until $z < 1$ (the Universe was about half of its age) when dark energy became dominant and the growth of structures slowed down dramatically, and the structures seem to be “frozen” in the co-moving system of coordinates, as can be seen from the last two panels. In this thesis, we are particular interested in the epoch between $z = 4$ and $z = 1$, when the galaxy clusters were being formed.

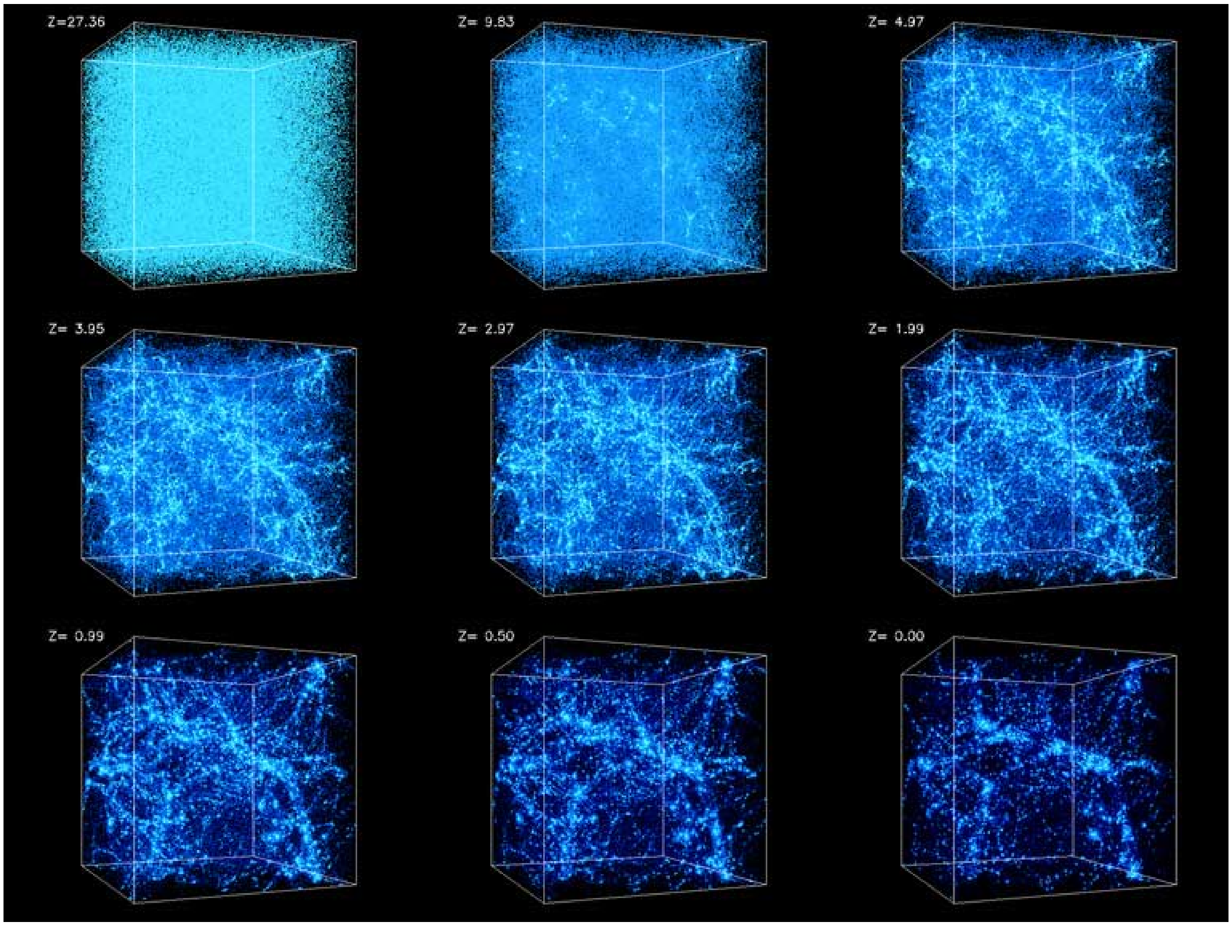

Fig. 1.2. Computer simulations of the formation and evolution of large-scale structures. Each frame portrays the structures in a 140 million light years box, from redshift of 30 to the present epoch (upper left z=30 to lower right z=0). Image credit: Simulations were performed at the National Center for Supercomputer Applications by Andrey Kravtsov (The University of Chicago) and Anatoly Klypin (New Mexico State University). Visualizations by Andrey Kravtsov.

1.2.2 Galaxy Formation

The above picture of large-scale structure formation is well understood and also in good agreement with observations. Galaxy formation, however, is much more complicated and poorly understood due to the complexity of various physical processes. One of the key processes that governs galaxy formation is so-called “feedback”, which are physical processes that prevent star formation. As the gas cools down and collapses under its own gravity, it may eventually from into stars, giving rise to a visible galaxy. However, supernovae explosions and stellar winds from massive hot stars may heat the surrounding gas, and even blow it out of the galaxy [14, 15]. Another important feedback source is active galactic nuclei (AGN), the active accretion phase of supermassive black holes (SMBH) at the centers of almost all massive galaxies. AGN release a vast amount of energy and is generally believed that it also efficiently heats and ejects the cold gas [16, 17]. Both stellar and AGN feedback processes can effectively suppress star formation, thus modulating the subsequent evolution of the host galaxy.

Environment also has a profound impact on the formation and evolution of galaxies. In the local Universe, galaxies in high dense clusters are mostly red, old and massive ellipticals or S0 (lenticular) galaxies that have quenched their star formation. On the contrary, younger star-forming galaxies such as spiral galaxies are generally found in the low density field. This is the well known “morphology-density” relation [18, 19], indicating that star formation activities are strongly suppressed for galaxies in high density environments than the low density counterparts. Fig. 1.4 illustrates this relation. In addition, existing studies suggest that cluster galaxies formed most of their stellar components at high redshift ($z > 2$), when the Universe was only several billion years old, with a swift shut-down of their star-formation and evolved passively since the last ∼10 billon years [20–25].

At high redshift ($z > 1.5$), some of the existing studies suggest that unlike the case of local clusters, galaxies in dense environments seem to show enhanced star-formation relative to the field [27–32], although it is still under debate as contrary evidence also exists [33, 34]. To understand how and when galaxy quenching happened, as well as to study the early environmental impacts, a dive into the early stage of cluster formation is needed.

1.2.3 The Early Stage of Clusters

Galaxy clusters are the most massive, virialized systems with masses $\geq 10^{14}$ $M_\odot$. Numerical simulations suggest that cluster-sized halos already begin to form at $z > 2$, as illustrated in Fig. 1.3, where we show the evolution of a massive cluster-sized halo ($\sim 10^{15} M_\odot$) in a dark matter simulation [13]. Similar to Fig. 1.2, this figure is a zoom-in into a centred cluster-size halo and its surroundings. The different panels show the dark matter density distribution at four different redshifts ($z \sim 6, 2, 1, 0$) and on three different scales (100, 40, 15 h^{-1} Mpc). The general region of a forming cluster ('protocluster') can already be identified as early as $z \sim 6$ in the form of modest density contrast in the dark matter distribution. Initially there are numerous small subhalos (bright clumps) in the matter distribution at $z \sim 6$ while the central massive halo has not been developed yet. Over time, the central halo emerges at $z \sim 2$ and grow larger through mergers, which eventually forms a cluster seen in the present-day Universe at $z = 0$.

Fig. 1.3 indicates that in priciple we can identify the progenitors of clusters (protoclusters) by looking for dark matter overdensities traced by galaxies in distant Universe. The ∼4 Gyr period between $z \sim 4$ and $z \sim 1$ is critical for the assembly of massive galaxies when the cosmic star-formation rate density (CSFRD) reached a peak and most of the stellar mass was assembled into individual galaxies [35]. Furthermore, recent simulations suggest that contribution of protoclusters to the CSFRD increases significantly with redshift, as illustrated in Fig. 1.5. The fractional CSFRD in clusters is rather small ($\sim 1\%$) at $z = 0$. As we move into the high redshift Universe, the fractional CSFRD in protoclusters increases to 20% at $z = 2$ and 50% at $z = 10$.

Meanwhile, the insets of Fig. 1.3 suggest that galaxy clusters formed 50% of their total stellar mass by z = 2. If we consider the whole 4 Gyr "Cosmic Noon" epoch at $1 < z < 4$, the Universe and present-day clusters formed about 50% and 75% of their total stellar mass, respectively. Therefore, distant protoclusters may be important in driving the early history of cosmic star-formation and mass-assembly. Observing protoclusters can also give us very important clues to the processes of galaxy formation in the densest environments, such as the infall of matter from the filamentary cosmic web, the gas fueling of star formation, interactions between galaxies, co-evolution of galaxies and their SMBHs, formation of brightest cluster galaxies (BCGs), etc. In the next section, we will discuss the observational methods for identifying these high-redshift protoclusters.

1.3 Observing Protoclusters and High-redshift Galaxies

Observationally, protoclusters are usually identified through measuring the galaxy overdensities in a certain surface area or volume. Galaxy overdensity is defined as $\delta = (\rho - \bar{\rho})/\bar{\rho}$, where ρ is the number density of galaxies within the measured region and $\bar{\rho}$ is the average number density of galaxies in the general field. However, it is a challenging task to identify protoclusters as they are far from virialized, and are distributed over large cosmic volumes with their angular sizes expected to span 20–30 arcminutes in the sky [36, 37], which make it observationally expensive to rely on blind spectroscopic surveys to study them with high precision. Moreover, the largest structures (those which will evolve into systems similar to the Coma cluster with their total masses exceeding $\sim 10^{15} M_{\odot}$) are rare with a space density of $\approx 2\times10^{-7}$ Mpc^{-3} (comoving) [37]. To date, only a handful of protoclusters have been found in the "blank-field" spectroscopic surveys [20, 33, 34, 38–42].

An alternative way to successfully identify protoclusters is by pre-selecting the surface overdensity regions traced by star-forming galaxies photometrically and follow them up with spectroscopy. There are two general methods to select these high redshift star-forming galaxies and we describe them here.

Lyman-Break Technique Lyman-Break Galaxies (LBGs) are the rest frame UV-selected star-forming galaxies that have a strong break at the Lyman limit 912Å. The break originates from the fact that photons whose wavelengths are shorter than 912Å are absorbed by the hydrogen gas in the star-forming regions of the galaxy and along the line of sight to us. At high redshift ($z > 2.5$), the break is redshifted into observed optical windows (>3200Å), enabling us to use optical filters to select those who "disappear" in the bluest filters.

Fig 1.6 illustrates this LBG technique. A galaxy appears to "drop out" in the bluest filter but can be clearly seen in the other filters. Using this drop-out technique, it is possible for us to identify high redshift galaxies without spectroscopy and to search for potential protocluster candidates. However, the disadvantage of this technique is that the typical redshift uncertainties of LBGs are fairly large, with $\Delta z \sim 0.3 - 0.5$ (corresponding to a comoving distance about 300-500 Mpc at $z \sim 3$), making it prone to the background or foreground interlopers when selecting overdense structures.

A number of protoclusters were identified using the LBG technique [38, 43–47]. It appears that LBGs generally have medium mass (up to a few $\times 10^{10}$ $M_\odot$) and medium dust extinction (E(B-V)$\sim$0.2). Their ages range from several million years up to 1 Gyr with a relatively high star-formation rate of several hundred solar mass per year [48, 49].

Lyα emitters To overcome the large redshift uncertainties associated with the LBG selection, another common method is to use a narrow band filter to select the galaxies that have strong emission lines due to their star formation activities. Lyα emitters (LAEs) are such type of galaxies that have strong emission lines at the hydrogen Lyα line of 1216Å (n=2$\rightarrow$n=1). The Lyα emission is a recombination line of a free electron and a proton from the excited hydrogen atom, which are ionized by young, massive and short-lived O and B type stars in the star-forming galaxies. Once again, at high redshift ($z > 2$) the Lyα line is redshifted into the optical windows and thus can be used as a method to select star-forming galaxies with ground-based telescopes.

Unlike the LBGs which are usually selected using broad-band filters (typical with a full width at half maximum of $\sim$ 1000Å), LAEs are selected using a narrow-band filter (FWHM $\sim$ 50Å). The use of a narrow-band filter enables a selection of galaxies in a much narrower redshift range, thus is advantageous in identifying protocluster candidates via galaxy overdensities with little contamination from fore-and background interlopers

To identify LAEs, a narrow-band filter which targets the Lyα line at the particular redshift and a broad-band filter with a same or close central wavelength are used. The broad-band filter probes the UV-continuum flux density of the sources and the Lyα emission is measured by comparing the narrow-band flux with the broad-band flux. Specifically, LAEs are usually selected by measuring the equivalent width (EW), defined as

$$\mathrm{EW} = \frac{F_{line}}{f_{cont}} \tag{1.1}$$

where F_{line} is the emission line flux and f_{cont} is the flux density in the continuum at the central wavelength of the line. Objects with large rest-frame EWs (typically > 20Å) are selected as LAEs.

Compared to LBGs, existing observations suggest that LAEs are less massive ($10^8 - 10^{10}$ M$_\odot$) and younger (several hundred million years old), with modest star-formation rate of several solar mass per year [50–52].

In the second part of this thesis, LAEs and LBGs are used to identify protoclusters. Besides these two methods, another approach is to use the Spectral Energy Distribution (SED) fitting technique. Galaxies emit electromagnetic radiation over the full wavelength range, and the distribution of energy over wavelength is referred to as the Spectral Energy Distribution (SED). SEDs are our primary source of information about the properties of galaxies as different physical processes dominating at different wavelengths leave their imprints on the shape of the spectrum. For example, young, massive stars emit most of their light in UV, thus the UV luminosity in the galaxy's SED is an indicator of the star-formation rate. The stellar mass of a galaxy is determined by its well-established stellar population which dominates the optical and near-IR parts of the spectrum, thus the optical/Near-IR radiation of the galaxy can give us information about its total stellar mass. When fitting different galaxy models to the observed SEDs as a whole, multiple physical properties of galaxies, such as stellar mass, star-formation rate and even redshift can be determined simultaneously.

Fig. 1.7 gives an example of the SED fitting result of a high-redshift galaxy. It is evident that SED fitting is a robust technique to obtain photometric redshift of the galaxies, in the absence of spectroscopic observations. In the first part of this thesis, protocluster galaxies are mainly selected using this SED fitting technique.

1.4 Outline of this Thesis

In this thesis, I present two studies on two different protoclusters at $z > 3$, identified using galaxies selected via photometric redshift as well as LAEs and LBGs. Located at $z = 3.13$ and $z = 3.78$ respectively, these two protoclusters give us opportunities to study the environmental impacts on galaxy formation and different galaxies constituents within at the early stage of cluster formation.

This thesis is organized as follows. In Chapter 2, I discuss our multiwavelength survey of a protocluster at $z = 3.78$. I discuss a detailed investigation of all galaxy types residing in one of the most massive forming clusters known to date. Their relative spatial distributions around the structure are also investigated and the scientific implications will be discussed. In Chapter 3, I present a study of another protocluster in which we focus on how a massive cosmic structure is traced by different galaxy populations. The environmental effects on galaxy properties are also discussed along with rare sources discovered within the protocluster. In Chapter 4, I summarize our main results from the two studies and conclude them in one framework.

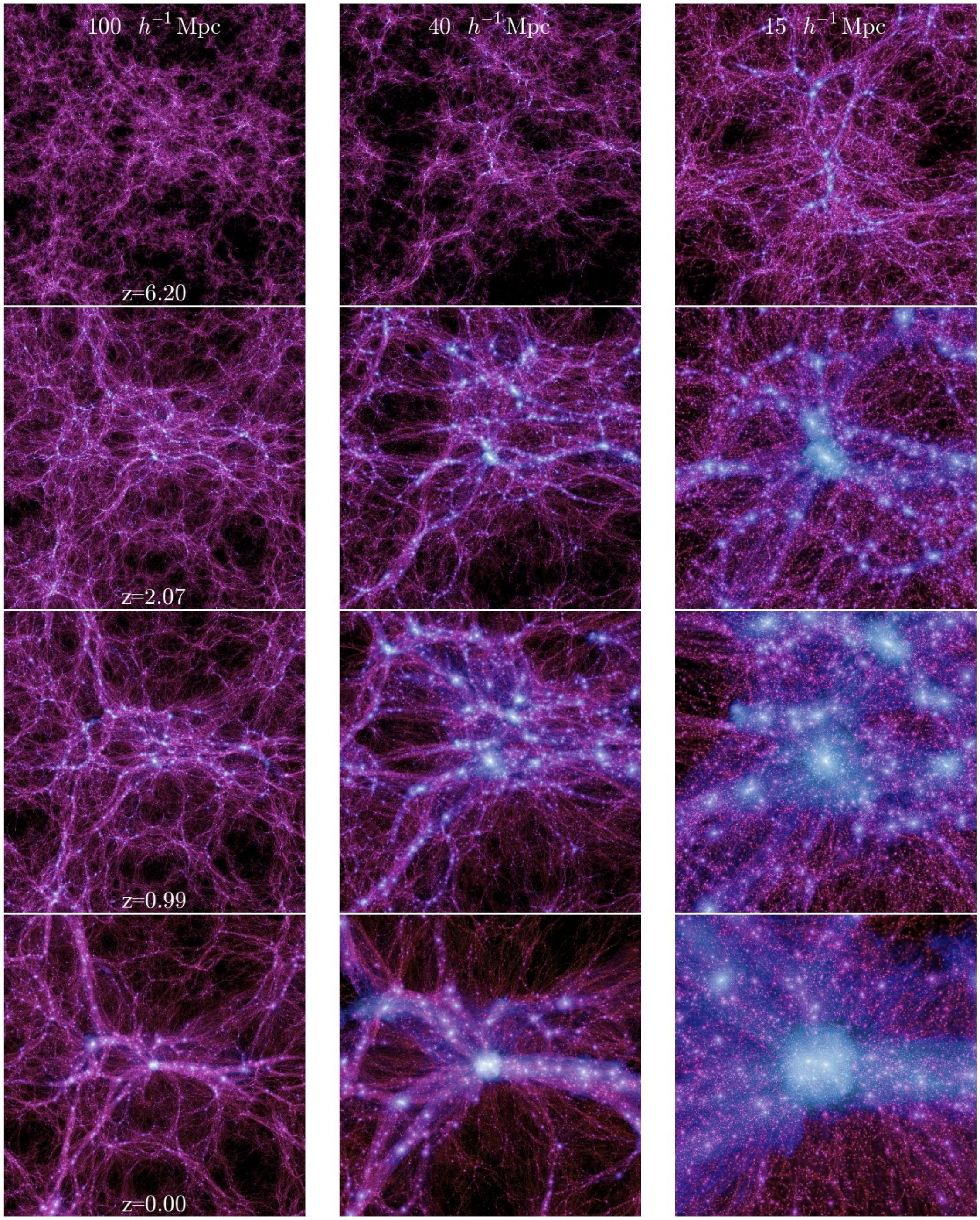

Fig. 1.3. The evolution of a massive Coma-like galaxy cluster in the Millennium II dark matter simulation. Dark matter distributions near the cluster are shown on different scales and at different epochs. Prior to $z \sim 2$ the "protocluster" can already be seen as the large-scale overdensity of dark matter. Figure from [13].

.

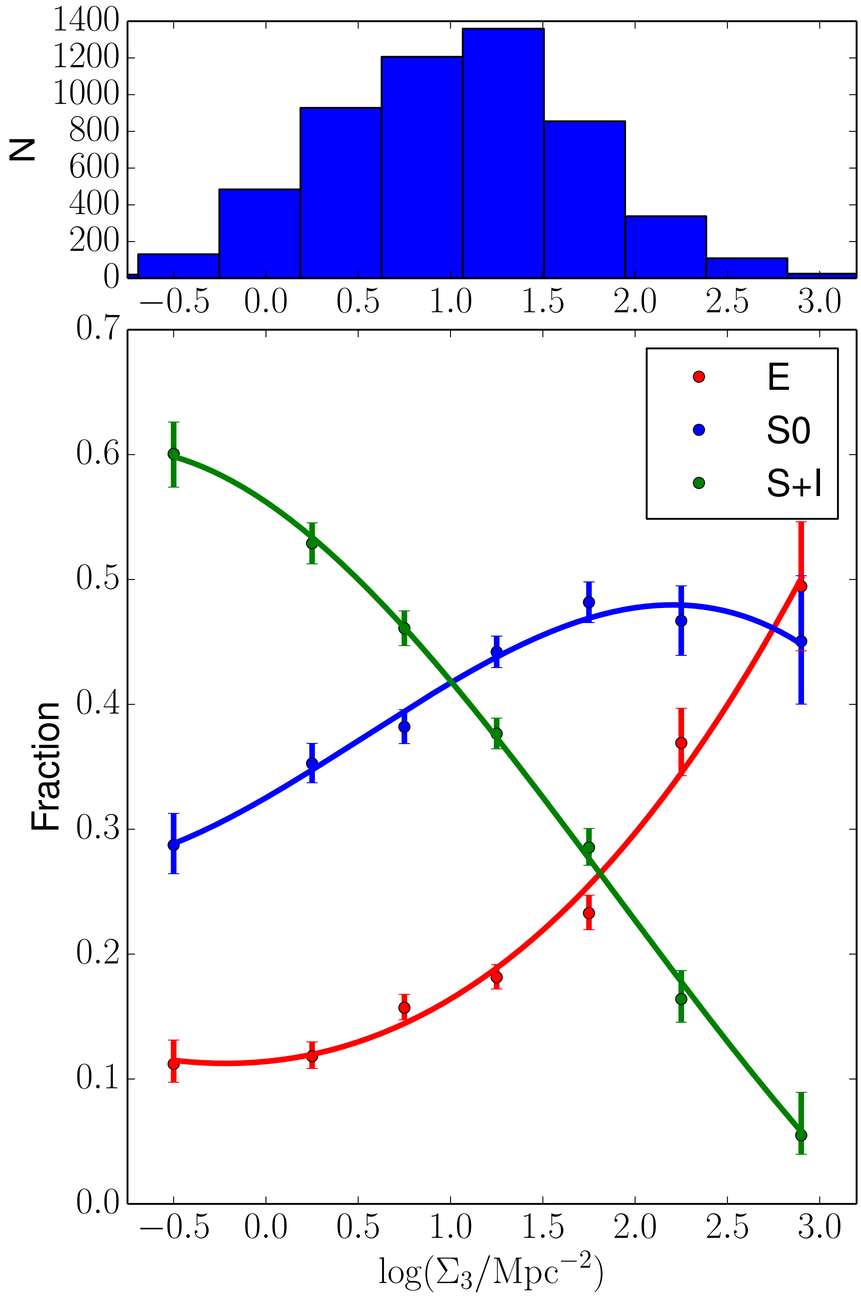

Fig. 1.4. The morphology-density relation is shown for spiral+irregular, S0 and elliptical galaxies. We can see that from low density (left) to high density environments (right), the galaxy populations change from being dominated by late-type (spiral and irregular) to early-type (elliptical and S0) galaxies. The upper histogram shows the number distribution of all galaxies over the projected density. From [26].

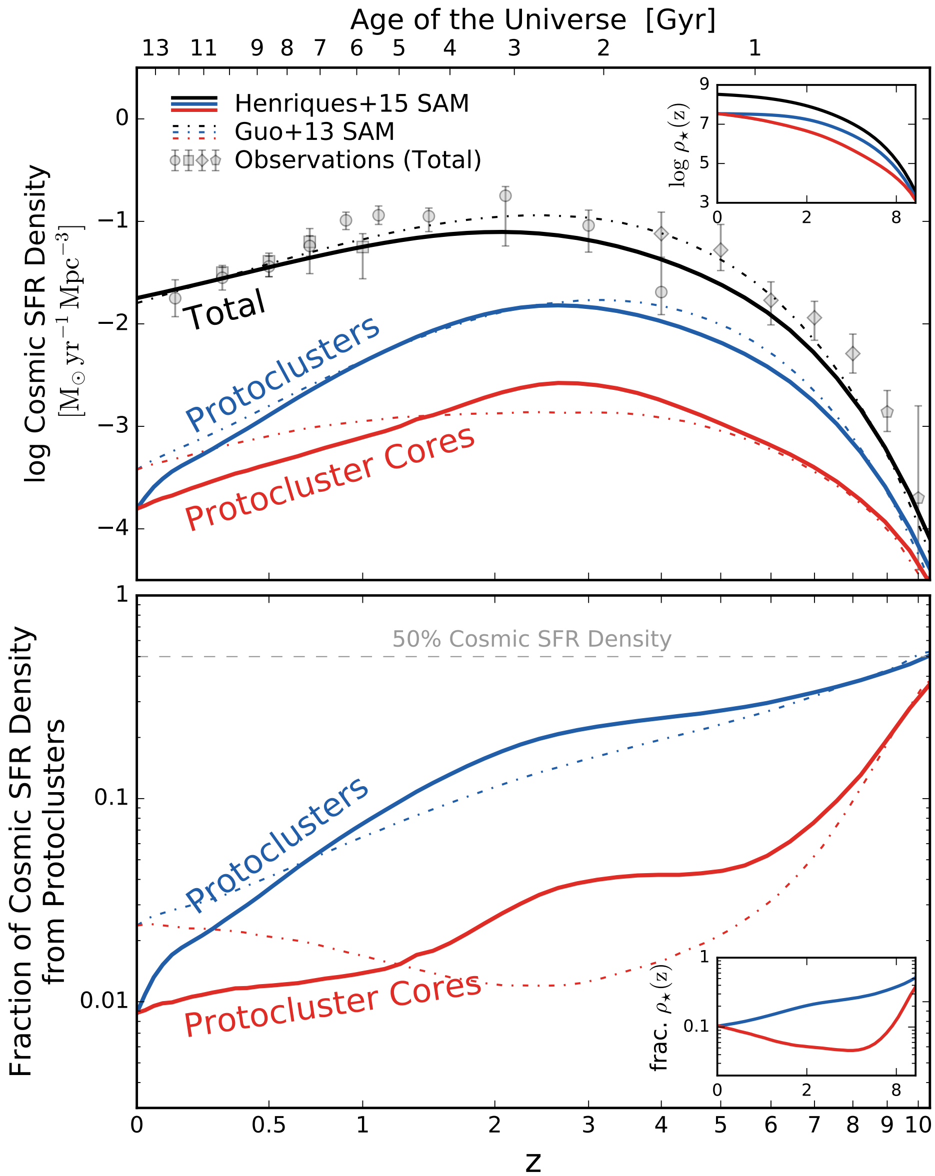

Fig. 1.5. Upper panel: Star-formation rate (SFR) density for all galaxies (black), protoclusters (blue), and cores (red). The associated stellar mass densities are shown in the inset. Data points show a set of observationally derived cosmic SFR density for comparison. Lower panel: Fractional contributions to the total cosmic SFR density of protoclusters (blue) and protocluster cores (red). The associated stellar mass density fractions are shown in the inset. From [36].

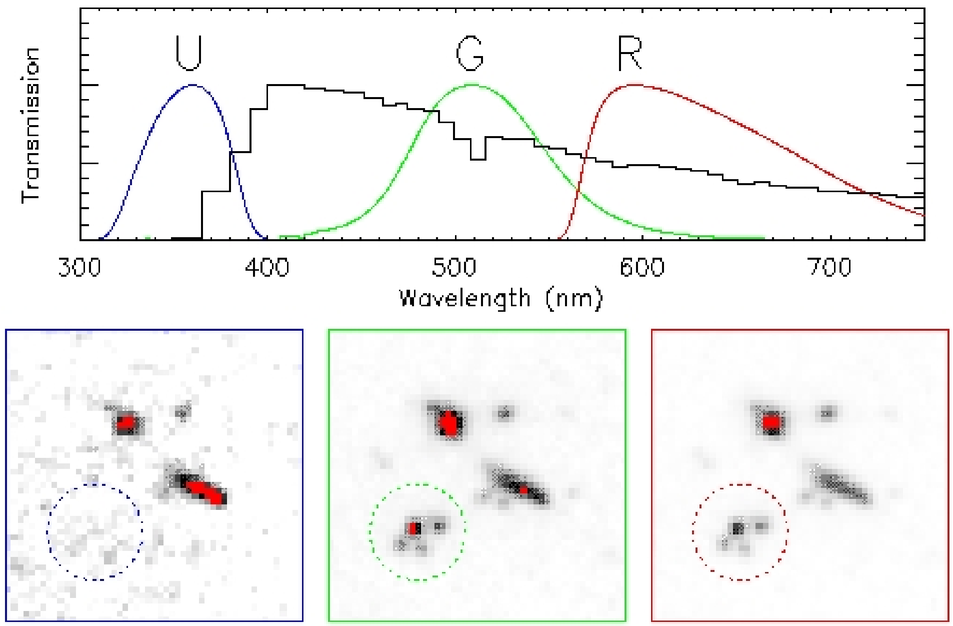

Fig. 1.6. Illustration of the LBG selection technique. The black line in the top panel shows a typical LBG spectrum at $z \sim 3$. The Lyman break can be seen between $300 - 400$ nm, which falls into the broadband U filter. The bottom panels show this galaxy observed in three different filters (U,G,R). The galaxy completely disappears in the bluest U filter but can be clearly seen in the other two filters. Image credit: Johan Peter Uldall Fynbo.

.

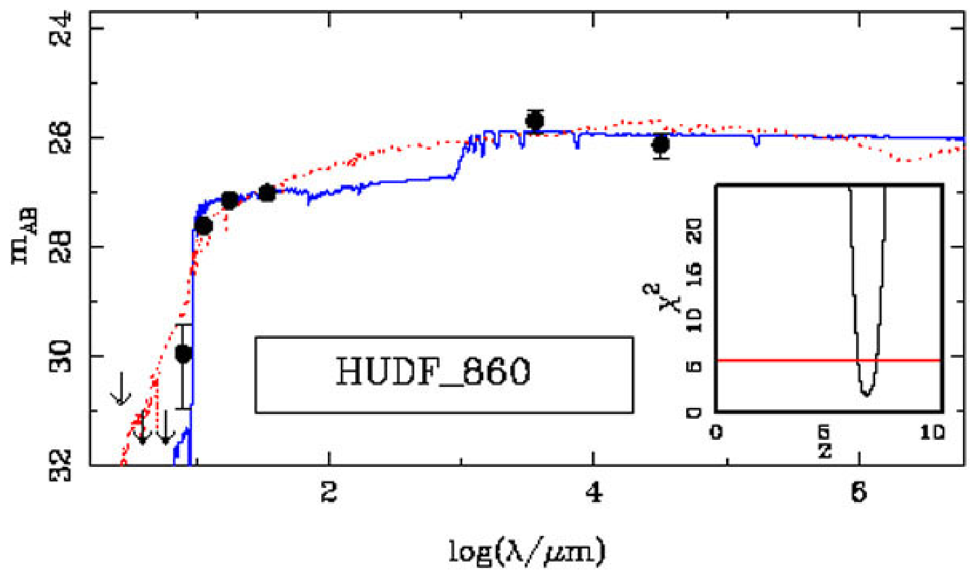

Fig. 1.7. An example of SED fitting analysis on a high-redshift galaxy. Not only redshift, but also age, star-formation history, dust extinction, mass and metallicity are all varied in search of the best-fit solution. The black points are the observed flux densities while the downside arrows denote the upper limits. The blue line is the best-fit model with redshift $z = 6.96 \pm 0.25$ and the red dotted line shows a fitting solution at low redshift. The inner panel indicates the fitted χ^2 values of the redshift. The low-z solution is clearly ruled out. From [53].

2. A CENSUS OF GALAXY CONSTITUENTS IN A COMA PROGENITOR OBSERVED AT $Z > 3$

In this chapter, in light of a spectroscopically confirmed protocluster PC217.96+32.3 discovered at $z = 3.78$ [45,46], we conduct a detailed census of its galaxy constituents. Besides the normal star-forming galaxies such as LAEs and LBGs reported in this protocluster [45, 46], we are interested in identifying evolved galaxies which have halted their star-formation. These galaxies are important for us to understand the history of massive galaxy formation in present-day clusters. In addition, we would like to study the environmental impacts on galaxy properties in this protocluster. To this end, we have obtained new near-IR data of this protocluster, which could provide us with information about the stellar mass of the galaxies, enabling us to study their properties in further details.

This chapter has been published as Shi et al. (2019) in Astrophysical Journal.

2.1 Abstract

We present a detailed census of galaxies in and around PC217.96+32.3, a spectroscopically confirmed Coma analog at $z = 3.78$. Diverse galaxy types identified in the field include Lyα emitters (LAEs), massive star-forming galaxies, and ultra-massive galaxies ($> 10^{11} M_{\odot}$) which may have already halted their star formation. The sky distribution of the star-forming galaxies suggests the presence of a significant overdensity ($\delta_{\rm SFG} \approx 8 \pm 2$), which is spatially offset from the previously confirmed members by 3–4 Mpc to the west. Candidate quiescent and post-starburst galaxies are also found in large excess (a factor of ∼8–15 higher surface density than the field) although their redshifts are less certain. We estimate that the total enclosed mass traced by candidate star-forming galaxies is roughly comparable to that of PC217.96+32.3 traced

by the LAEs. We speculate that the true extent of P217.96+32.3 may be larger than previously known, a half of which is missed by our LAE selection. Alternatively, the newly discovered overdensity may belong to another Coma progenitor not associated with PC217.96+32.3. Expectations from theory suggest that both scenarios are equally unlikely ($< 1\%$), in the cosmic volume probed in our survey. If confirmed as a single structure, its total mass will be well in excess of Coma, making this an exceptionally large cosmic structure rarely seen even in large cosmological simulations. Finally, we find that the protocluster galaxies follow the same SFR-M_* scaling relation as the field galaxies, suggesting that the environmental effect at $z \sim 4$ is a subtle one at best for normal star-forming galaxies.

2.2 Introduction

Local environment has a profound influence on the formation and evolution of galaxies. At low redshift, galaxies in dense cluster environments tend to be more massive, contain older stellar populations, have lower star formation rates and dust content, and a higher fraction have elliptical morphologies than their average field counterparts [21, 22, 54, 55]. The redshift evolution of the cluster red sequence and the properties of cluster ellipticals strongly support a scenario in which cluster galaxies underwent early accelerated formation followed by swift quenching [56–59]. While this general picture is accepted, the mechanisms responsible for the formation, evolution and quenching processes are still not well understood [60].

In high-density environments, the accretion rates of infalling gas and the frequency of galaxy interactions are expected to be higher, fostering enhanced star formation activities. A merger of gas-rich galaxies may include an ultra-luminous infrared galaxy (ULIRG) [61, 62] phase which efficiently converts the majority of their gas into stars over a short timescale. Dissipative gas-rich mergers may help the efficient feeding of gas into the central blackholes, triggering nuclear activity, which may quench star formation and create old, massive cluster ellipticals. [63]. High-density environments are therefore expected to consist of diverse galaxy constituents, including normal star-forming galaxies, ULIRGs, X-ray sources, AGN, and massive quiescent galaxies. A detailed census of diverse galaxy 'types' and their spatial distribution within the large-scale structure are essential to obtain a more comprehensive understanding of how the high density environment drives the evolution.

To directly witness the key epoch of cluster galaxy formation, one needs to identify the galaxy populations residing in young 'protoclusters'. In recent years, substantial progress has been made in the search for high-z protoclusters [64]. Searches around powerful radio sources at high redshift have identified significant galaxy overdensities [65–70]. A population of extremely dusty starburst systems, optically or X-ray-luminous AGN, and large Lyα nebulae are reported in some of the known protoclusters [71–79], in support of the theoretical expectations [80, 81]. The existence of massive 'red and dead' galaxy candidates at $z \sim 3$ offers tantalizing evidence that the formation of massive cluster ellipticals may have been well underway as early as 2 Gyr after the Big Bang [82].

The number of confirmed protoclusters and protocluster candidates has been increasing rapidly [33,40,41,47,83,84], offering a promising outlook for future protocluster studies; such as the impact of environment on the galaxy inhabitants, as well as the evolutionary link between unvirialized proto-structures and present-day clusters.

Despite this progress, a clear and coherent physical picture of how cluster environment influences galaxy formation has yet to emerge. We do not yet know how dense protocluster environments influence the galaxy therein: e.g., are rare systems such as radio galaxies, quasars, Lyα nebulae ubiquitous enough to be used as beacons of the highest density peaks of the universe? Do dense protocluster environments produce a different 'zoo' of galaxy constituents, or simply a scaled-up version of the average field? Addressing such questions may have an important cosmological implication: given their large pre-virialization volume and high galaxy overdensities, star formation in protoclusters can account for up to 30% of the cosmic star formation rate density at $z = 4$ [36].

Observationally, one of the main limitations has been the lack of our knowledge of the density structure of protoclusters. The angular size of the cosmic volume that will end up virialized by the present-day epoch is expected to be as large as 20 arcminutes – 30 arcminutes in the sky [37, 85], making it expensive to rely on blind spectroscopic programs to map out their structures with reasonable precision. To date, only a few systems exist with a detailed characterization of their sizes and density structures [45, 79, 86].

Another critical element in making progress is to obtain a detailed census of protocluster constituents. Understanding how different types of galaxy constituents are distributed within the large-scale structure is necessary to make a fair assessment of how the formation of galaxies is impacted by the environment in which they reside. For example, luminous Lyα nebulae are often found located at the outskirts or an intersection of the densest regions of a protocluster [79, 86]. Several studies reported that powerful AGN may suppress low-level star formation activity and produce a deficit of Lyα-emitting galaxies [87,88] although claims to the contrary also exist [89].

In this paper, we present a multi-wavelength study of galaxies along the sightline to the PC217.96+32.3 protocluster at $z = 3.78$, one of the most massive protoclusters discovered to date [45]. Existing spectroscopy has confirmed 48 members at z=3.76–3.81 (of which 34 lie at z=3.77–3.79) [46]. The locations of these members are indicated in Fig. 2.1. The three-dimensional 'map' of the spectroscopic members suggests that the structure is mainly composed of two large groups with a small velocity offset and of additional smaller groups falling in toward the center [46]. Given the level and angular extent of the galaxy overdensity, PC217.96+32.3 will likely collapse into a system with a present-day mass of $M_{\rm total} \geq 10^{15}{\rm M}_\odot$, making it one of the few spectroscopically confirmed Coma progenitors.

Having established the significance of the structure, we are motivated to take a broader view of the constituents of PC217.96+32.3; in particular, we are interested in identifying more evolved galaxies which may be more closely linked to massive cluster ellipticals in the present-day universe. To this end, we have conducted a deep near-

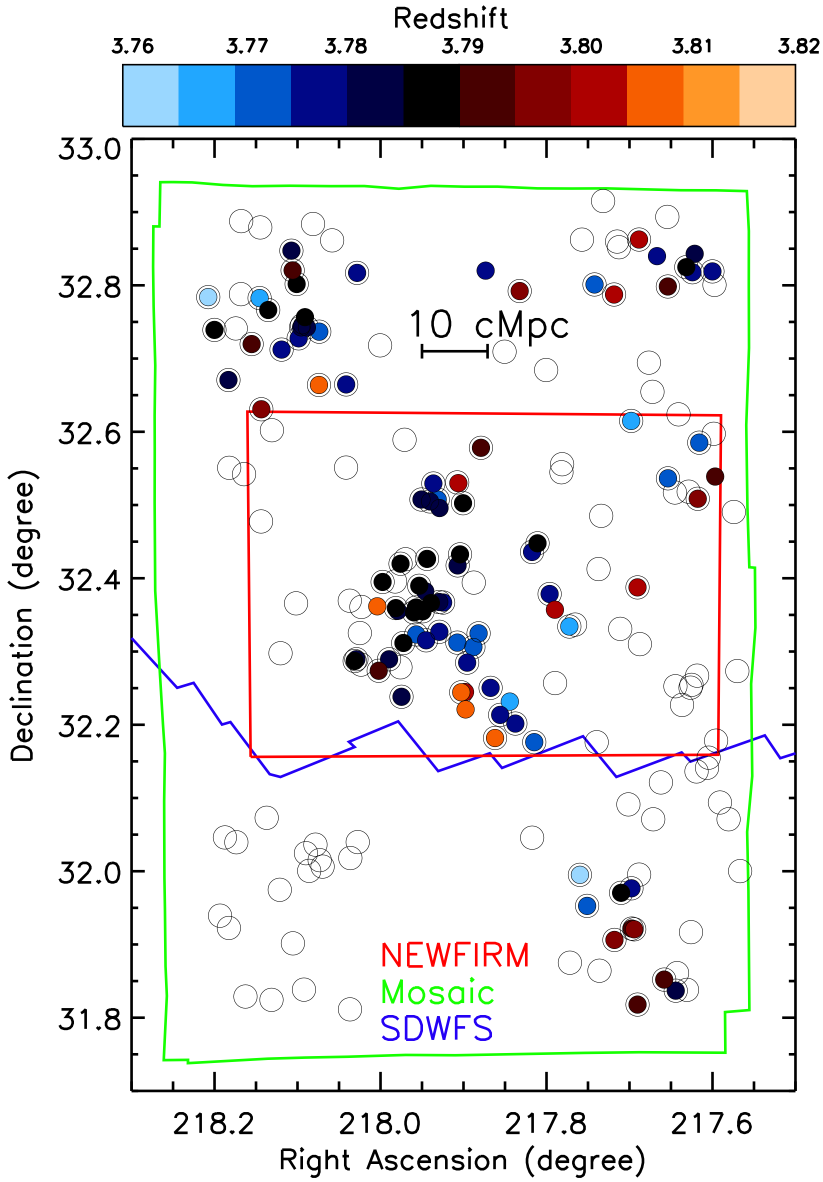

Fig. 2.1. The layout of our protocluster survey field is shown for the Mosaic ($B_W RI$: green), NEWFIRM (HK_S: red), and SDWFS data (blue to the north). The Subaru y-band data covers the field shown here in its entirety. Open circles denote the positions of photometrically selected LAEs, while filled circles show the spectroscopic sources in the range z=3.76–3.82, color coded by the redshift indicated by bar on top. PC217.96+32.3 is situated in the middle of our Mosaic field.

infrared imaging survey of the region, sampling the continuum emission at rest-frame visible wavelengths.

In this paper, we present new near-infrared H and K_S-band imaging on the central portion of the protocluster field (§2). Combining this with existing optical data from the NOAO Deep Wide-Field survey (NDWFS) [90] and mid-infrared data from the *Spitzer Space Telescope* [91], we identify a large overdensity of luminous galaxies in the region (§3). Population synthesis modeling of these galaxies suggests that they are likely to lie close to the redshift of the protocluster traced by the Lyman Alpha emitters (LAEs), although they have a somewhat different spatial distribution (§4). We discuss the masses, star-formation rates, and estimate the size of the overdensity in §4, and discuss the implications of finding such an overdense region in §5.

Throughout this paper, we make use of the WMAP7 cosmology $(\Omega_m, \Omega_\Lambda, \sigma_8, h) = (0.27, 0.73, 0.8, 0.7)$ from [92]. Distance scales are given in comoving units unless noted otherwise. Magnitudes are given in the AB system [93] unless noted otherwise. In the adopted cosmology, PC217.96+32.3 at $z = 3.78$ is observed when the universe was 1.7 Gyr old; $1'$ corresponds to the physical scale of 2.1 Mpc at this redshift.

2.3 Data and Photometry

The multi-wavelength data available in this field include the optical data taken with three broad-band filters ($B_W RI$: NOAO program IDs: 2012A-0454, 2014A-0164) using the Mosaic camera [94,95] on the Mayall telescope, and the *Spitzer* IRAC 3.6μm, 4.5μm, 5.8μm, and 8.0μm data taken as part of the Spitzer Deep Wide-Field Survey (SDWFS) [91]. As discussed in Dey et al. (2016) [46], the new optical $B_W RI$ data are combined with the reprocessed NDWFS data [90] to create the final mosaicked images.

We obtained y-band imaging from Hyper Suprime-Cam [96] on the Subaru telescope, which provides the field-of-view of 1.77 deg^2 and the pixel scale of $0''.168$. The observations were carried out on March 27, 2015 with typical seeing of $\sim 0.6''$, and consisted of 200 sec exposures with the total exposure time of 2.4 hours. The individual images were reduced and coadded using the HSC data processing pipeline [97]. The pipeline performed standard bias, dark, flat, and fringe calibrations, and the astrometry and photometry were calibrated based on Pan-STARRS1 surveys [98] before coadding.

In March 2015 and March 2016, we obtained deep imaging of the survey field using the NEWFIRM camera (NOAO program IDs: 2015A-0168, 2016A-0185) [99, 100] on the Mayall 4m telescope of the Kitt Peak National Observatory. The camera has a pixel size of $0.4''$ and covers a $28' \times 28'$ field of view. Images were obtained with H and K_S bands (KPNO filter no. HX (k3104) and KXs (k4102); λ_c=16310 and 21500 Å with the full-width-at-half-maximum (FWHM) of 3080 and 3200 Å respectively. We will refer to these filters as H and K_S band, hereafter). The pointing center – α=14:31:28.8, δ=32:23:24.0 (J2000) – was chosen to cover the known protocluster region in its entirety while sampling a sufficient flanking region outside of it. We used individual exposure times of 60 sec for both bands, and dithered the telescope between exposures up to $2'$ in random directions using the `DEEPSPARSE` dither pattern.

Each science frame is dark-subtracted and flat-fielded using the standard NOAO pipeline. We calibrate the astrometry using stars identified in the Sloan Digital Sky Survey DR7 catalog, and reproject each frame to a common tangent point with a pixel scale of $0.258''$ in order to match that of the optical data. The relative intensity scale of each frame was determined using the `mscimatch` task. The reprojected images were combined into a final stack using a relative weight inversely proportional to the variance of the sky noise. Only the frames with the delivered image quality of seeing $\geq 1.3''$ are included in the image stack. We trim the image borders whose exposure is less than 20% of the maximum exposure time, and obtain the final coadded mosaic with an effective area of $28' \times 35'$ (0.27 deg^2). The effective total exposure times of the mosaics are 12.1 and 18.7 hours for the H and K_S band, respectively. The photometric zeropoints are determined by cross-correlating the detected sources with the 2MASS point source catalog.

We resample the Spitzer SDWFS data to have a pixel scale of $0.774''$, i.e., three times larger than the optical/near-IR data. Having the pixel scales to be integer multiples of one another is necessary for extracting optical photometry via a template-fitting method (see later). The 5σ limiting magnitudes measured in a $2''$ diameter aperture are 26.88, 26.19, 25.37, and 25.10 AB in the optical data ($B_W RIy$), 24.05 and 24.83 AB in the near-IR data (HK_S), respectively. The seeing measured in the stacked images is $1.0''$ in the $B_W RI$ images, $0.6''$ in the y-band, and $1.2''$ in the HK_S bands. The sky coverage of our dataset is illustrated in Figure 2.1.

2.3.1 Multi-wavelength Catalog

We use the PSFEx software [101] to measure the point spread function (PSF) of each image out to a radius of $3''$. The two-dimensional PSFs are radially averaged to obtain the circularized PSF. Taking the worst-seeing data (K_S band) as the target PSF, we derive the noiseless convolution kernel for each image using the IDL routine `MAX_ENTROPY`. We use the full shape of the observed stellar profiles rather than assuming a function form such as Moffat profiles. The details of the PSF matching procedure are given in [102]. All optical and near-IR images are convolved with the appropriate kernels to create a set of PSF-matched science images.

Source detection and photometric measurements in the $B_W RIyHK_S$ bands are carried out running the SExtractor software [103] in dual mode on the PSF-matched images with the K_S band data as detection band. At the protocluster redshift ($z = 3.8$), the K_S band mainly samples the continuum emission at the rest-frame ≈ 4400Å.

The SExtractor parameter MAG_AUTO is used to estimate the total magnitude, while colors are computed from fluxes within a fixed isophotal area (i.e., FLUX_ISO). Colors measured in FLUX_ISO and FLUX_APER are in agreement with each other within 0.1 mag. As the images are PSF-matched, aperture correction is constant in all bands, and is given by the difference between MAG_AUTO and MAG_ISO estimated in the K_S band.

For the *Spitzer* IRAC images, we take a different approach as it is not practical to convolve all images to the FWHM of any IRAC PSF, which is much broader ($\sim 2''$). We use the TPHOT software [104] which performs 'template fitting photometry' similar to TFIT [105,106]. The software uses the information (source shape and position) supplied by a higher-resolution data and simultaneously fits the fluxes of multiple nearby sources to minimize residual flux. Since the FWHM of the K_S band PSF is not negligible compared to that of the IRAC data, we also derive the convolution kernel using the same procedure above. For the effective PSF of the IRAC bands, we rotate the published IRAC PSF by a series of position angles with which the SDWFS data were taken, and create a weighted average image.

Finally, all photometric catalogs are merged together to create the final multi-wavelength catalog, where the TPHOT-measured fluxes are considered identical to the MAG_ISO fluxes of the optical/near-IR bands. Given the completeness of the K_S band data, we only consider sources that have the signal-to-noise ratio (SNR) greater than 10, roughly corresponding to K_S magnitude of 24.0 mag. The final multi-wavelength catalog contains 27,845 sources.

2.3.2 Photometric Redshift and SED Modeling

We derive photometric redshifts with the CIGALE code [107] using the full photometric information. The reliability of the photo-z estimates is evaluated using the existing spectroscopic sources, which targeted a subset of UV-bright galaxies satisfying the Lyman Alpha Emitter (LAE) or Lyman Break Galaxy (LBG) color selection over a 1.2×0.6 deg^2 contiguous region in the PC217.96+32.3 field. The details of these selection methods in our survey field are discussed in [108] and [45]. Of the 164 sources at $z_{\rm spec} = 3.4 - 4.2$, 48 galaxies lie within the NEWFIRM coverage. Of those, only 17 galaxies are bright enough to be detected in the K_S band catalog with a photo-z estimate.

We find the redshift dispersion $\sigma_z/(1+z_{\rm spec})= 0.15$ where σ_z is the standard deviation of Δz ($\equiv z_{\rm spec} - z_{\rm phot}$). The large dispersion is due to three outliers which have $(z_{\rm spec} - z_{\rm phot})/(1 + z_{\rm spec}) > 0.2$. We find that their redshift probability density functions have two peaks, one at $z < 1$ and the other at $z \sim 4$; given that they are fainter than other galaxies, redshift degeneracy is caused by the fact that the spectral break between B_W and R is not strong enough to be unambiguously determined as a Lyman break. However, for all three galaxies the probability to lie at $z = 3.4 - 4.2$ (computed by integrating the photometric redshift probability density function in the interval, which we denote as p_z) is greater than 50%. Excluding these three galaxies, the redshift dispersion $\sigma_z/(1 + z)$ is 0.06.

After considering the photometric redshift constraints of our spectroscopic sources, we select protocluster candidate galaxies by requiring that $z_{\rm phot} = 3.4 - 4.2$ for the sources whose redshift probability density functions (PDFs) are singly peaked, and $p_z \geq 0.5$ for those with doubly peaked PDFs. All of the 17 spectroscopic members meet these criteria. The range $z_{\rm phot} = 3.4 - 4.2$ is chosen based on the photometric redshift error as discussed previously. A similarly inclusive range was used by [82], who studied the stellar populations in and around another protocluster.

After visual inspection, we remove the sources with potential contamination in the photometry including those that are too close to brighter sources or to the edges of the images. Our protocluster galaxy sample consists of 263 sources, which also includes the spectroscopic members of the structure.

We examine the rest-frame UV colors of our protocluster candidates to assess their overall similarities to broad-band color-selected LBGs. We match their positions to the I-band-selected photometric catalog used for the B_W band dropout selection [45, 108]. Of the 263 sources, 202 galaxies (77%) are detected in the I-band with the signal-to-noise ratio (SNR) ≥ 7. In Fig. 2.2, we show their locations on the $B_W - R$ vs $R - I$ color diagram. Of the 202 galaxies, 135 galaxies (67%) satisfy the formal LBG criteria, and an additional 22 galaxies (11%) are within 0.25 mag of the formal $B_W - R$ color cut. The galaxies outside the selection window tend to be fainter in the R and I bands ($R < 25.5$) while dropping out of the B_W band, which results in a weaker constraint on the $B_W - R$ color. However, their UV colors are generally similar to their UV-brighter cousins. Their $R - I$ colors are redder than those within the LBG selection criteria, which likely contribute to a weaker spectral break in the B_W band. Thus, we conclude that our photo-z estimate works relatively well for moderately dust obscured star-forming galaxies whose spectral energy distributions (SEDs) are similar to those of LBGs.

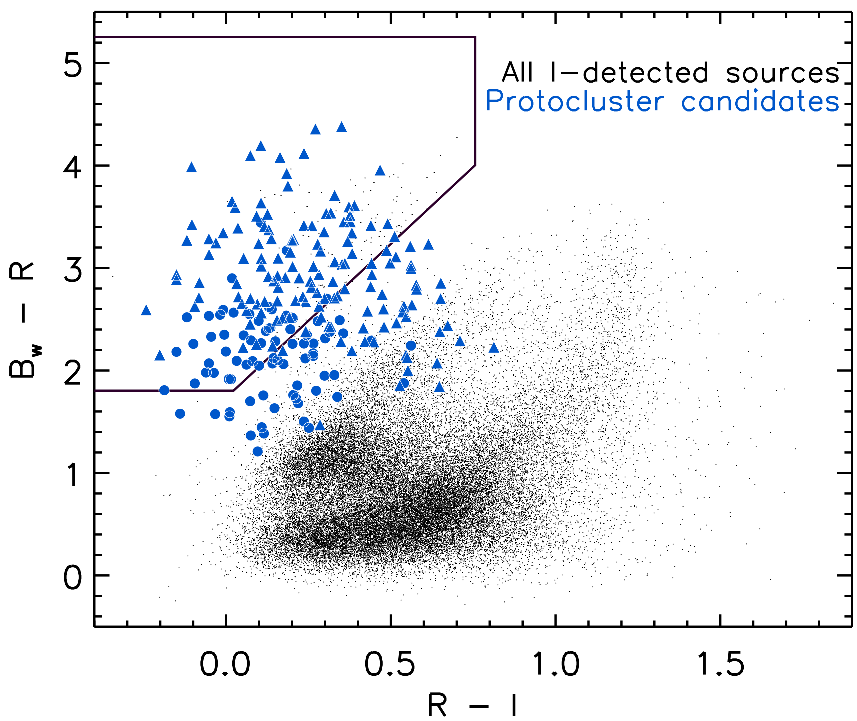

Fig. 2.2. The locations of the photo-z protocluster candidates on the $B_W - R$ vs $R - I$ diagram are shown together with all I-band detected sources (black dots). Galaxies that are undetected in the B_W band are shown as upward triangles. The formal LBG criteria to select galaxies at $z \sim 3.4 - 4.2$ are shown as polygon in the upper left corner [45]. The majority of our photo-z candidates would formally meet the LBG selection.

We determine the physical properties of the photo-z protocluster candidates using the CIGALE software. We use the stellar population synthesis models from [109], the dust reddening law from [110] with A_V values ranging from 0 to 5 in steps of 0.1 mag, solar metallicity, and Salpeter initial mass function [111]. We carry out three separate runs assuming a constant star formation histories, an exponentially declining SFH with τ values from 50 Myr to 10 Gyr in steps of 200 Myr, and a delayed star formation model. In Fig. 2.3 (left two columns), we show the best-fit SED model, population parameters, and redshift PDF (inset) for a subset of our sample. As can be seen in the figure, these photo-z candidates are mostly star-forming galaxies with a strong Lyα break and relatively blue UV slope. The best-fit star-formation rate implies they are actively forming stars at a relatively high level (up to several hundreds solar mass per year) with a moderate amount of dust (E$(B-V)\sim$0.1 – 0.2).

2.4 Balmer-break Galaxy Candidates in the Protocluster Field

2.4.1 Selection of galaxies with evolved stellar populations

As discussed in § 2.3.2, the photometric redshift technique is most effective in selecting LBG-like galaxies. Here, we use a set of color selection criteria tuned to isolate galaxies with a strong Balmer/4000Å break, a feature strongest in old stellar populations dominated by A and F stars. In this work, we use the following color criteria, which are similar to those found in the literature [67, 112–118]:

$$H - K_S > 1.2;$$
$$[3.6] - [4.5] < 0.5$$

The first condition imposes that a strong Balmer/4000Å break falls between the H and K_S bands, which occurs in the redshift range $z = 3.6 - 4.2$. Using the EZGAL software[1] [119] with the stellar population synthesis models from [109], we

[1]http://www.baryons.org/ezgal/

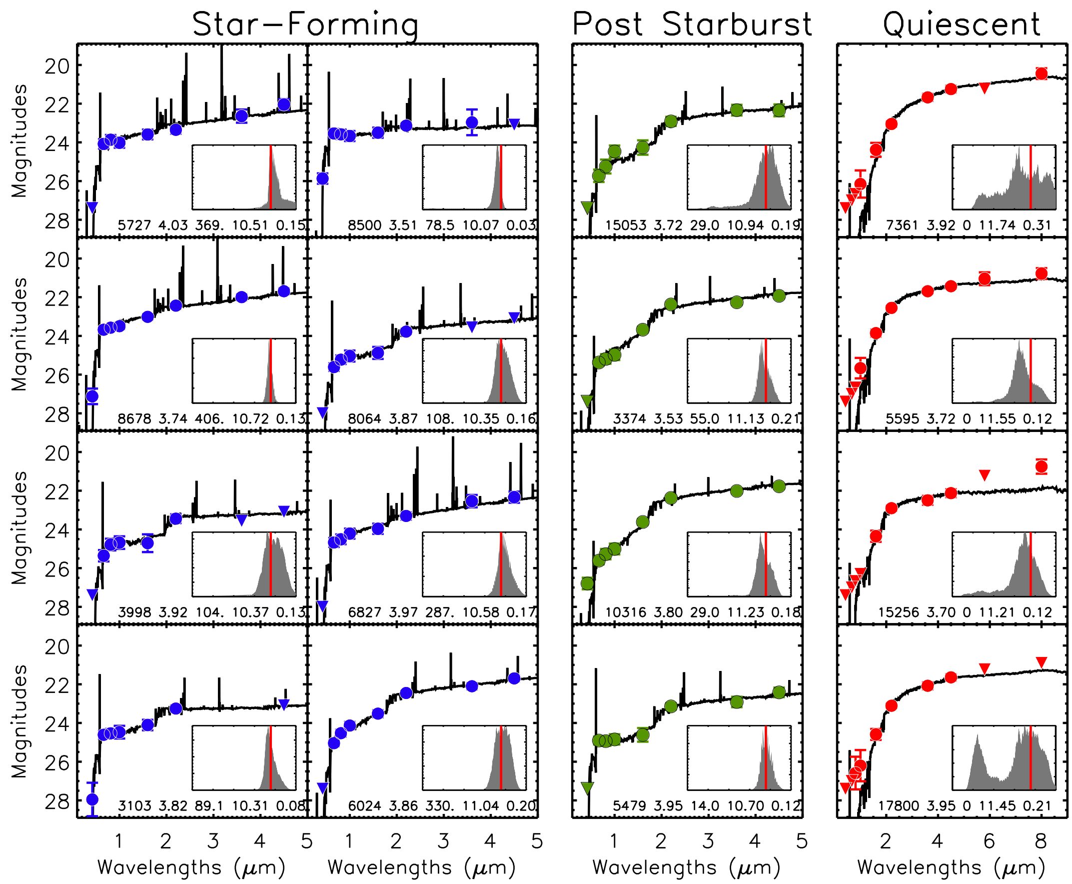

Fig. 2.3. Observed SEDs are shown for a subset of our galaxy candidates, which include normal UV-bright star-forming galaxies (blue), post-starburst candidates (green), and quiescent galaxy candidates (red). Filled circles represent our photometric measurements, while triangles denote 2σ limits in the case of non-detection. We also show the CIGALE redshift probability density functions as shaded grey regions (inset); the plotting range is $z = [0, 5]$. The redshift of PC217.96+32.3 is shown as a red vertical line. On bottom of each subpanel, we list object ID, best-fit photo-z, star formation rates (in units of $M_{\odot}$ yr^{-1}), $\log(M_{\rm star})$ (in units of $M_{\odot}$), and dust reddening parameter E$(B - V)$.

compute the $H - K_S$ colors of stellar population as a function of age, assuming three families of star formation histories: 1) instantaneous burst; 2) constant star forma-

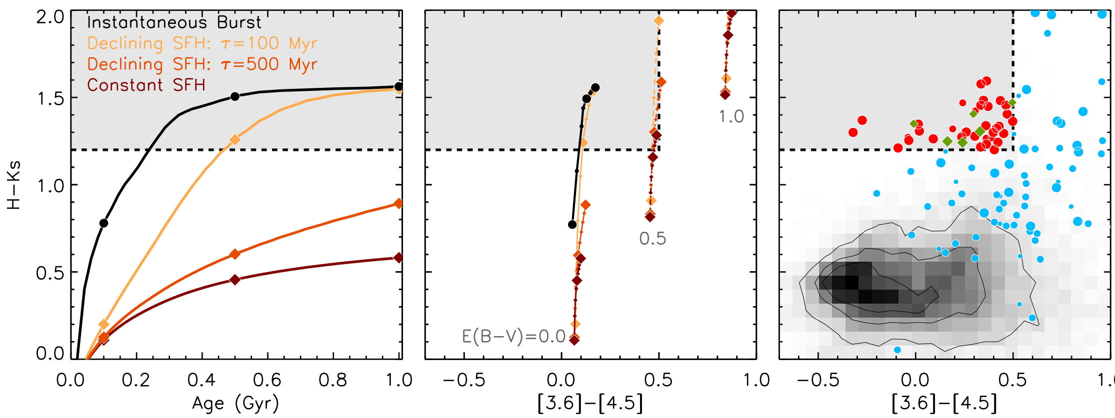

Fig. 2.4. *Left:* expected $H-K_S$ colors are shown as a function of population age for single burst (black), exponentially declining SFH with $\tau = 0.1$ Gyr (light orange), $\tau = 0.5$ Gyr (dark orange), and constant SFH (brown). Only the galaxies with relative quiescence can achieve the $H-K_S$ color cut (grey shades). *Middle:* the evolution of $H-K_S$ vs $[3.6]-[4.5]$ colors are shown for three dust reddening parameters E$(B-V)$=0 (solid), 0.5 (dashed), and 1.0 (dotted). Grey shaded region marks our selection criteria for the Balmer/4000Å break galaxies candidates. The circles in each model mark the population age of 0.1, 0.5, and 1 Gyr, from bottom to top. *Right:* The sources satisfying our BBG criteria are shown in red (R-band undetected) and green (R-band detected) symbols. A subset of photo-z protocluster candidates with robust $[3.6]-[4.5]$ color measurements are also indicated (light blue circles). The grey shades and contours show the distribution of all sources (25%, 50%, and 75% levels). The size of the symbols indicates the stellar masses of the galaxies, classified as $M_\star < 10^{10.5} M_\odot$ (small), $10^{10.5} M_\odot < M_\star < 10^{11} M_\odot$ (medium), and $M_\star > 10^{11} M_\odot$ (large).

tion histories (CSF); and 3) exponentially declining τ model (EXP models hereafter: SFR $\propto \exp[-t/\tau]$) with τ values of 0.1 Gyr and 0.5 Gyr. As illustrated in the left panel of Figure 2.4, a stellar population formed via a single instantaneous burst would meet this condition at age 250 Myr, while galaxies formed through a more extended star formation episode (τ=100 Myr) would take $\approx$400 Myr to attain the same strength.

The second criterion requires that the continuum slope at $\lambda_{\rm rest}$ =7000–9000Å is relatively flat, ensuring that the red $H - K_S$ color is not due to dust reddening. In the middle panel of Fig. 2.4, we illustrate the effect of interstellar dust assuming the reddening parameters E($B - V$)=0, 0.5, 1.0 and the extinction law from [110].

Using the above criteria, 56 galaxies are identified. Thirteen of them have power-law-like SEDs in the mid-infrared with typical brightness of $\approx$ 21 AB in the 5.8μm or 8.0μm bands; the $H - K_S$ colors range in $1.2 - 1.3$, on the low end of the color distribution. Four of them are also present in the *Spitzer* MIPS 24μm source catalog provided by [120]. These sources are likely heavily dust-obscured AGN which scatter into our selection. Of the thirteen galaxies, 7 (54%) and 8 (62%) of them meet the IRAC color criteria for high-redshift AGN selection proposed by [121] and [122], respectively. We remove all thirteen galaxies from our sample.

The final sample consists of 43 galaxies, which we refer to as Balmer break galaxy candidates (BBGs) hereafter. Seven galaxies are also our photo-z protocluster candidates. In the right-most panel of Fig. 2.4, we show the $H - K_S$ and $[3.6] - [4.5]$ colors of all K_S-band detected sources with reliable color measurements. The BBGs without (with) the photo-z estimate are shown in red (green), while the distribution of the remainder is indicated as greyscale and contours where the contour lines enclose the 68% and 95% of all galaxies.

Most BBGs are very faint at observed optical wavelengths (i.e., faint at rest-frame UV wavelengths). Of the 43 galaxies, only seven (16%) are detected at the 5σ level ($R \leq$ 26.2 AB) in the R-band while dropping out of the B_W band. The three brightest galaxies (in the R-band) formally meet the LBG color criteria. The remaining four likely have similar SED shapes to their R-brighter counterparts but are simply too faint to place strong enough constraints on the $B_W - R$ colors. All seven have photo-z probability distributions with a single peak at $z > 3.5$. The remaining 36 galaxies (84%) are formally undetected in the R band with a few detected at a lower significance.

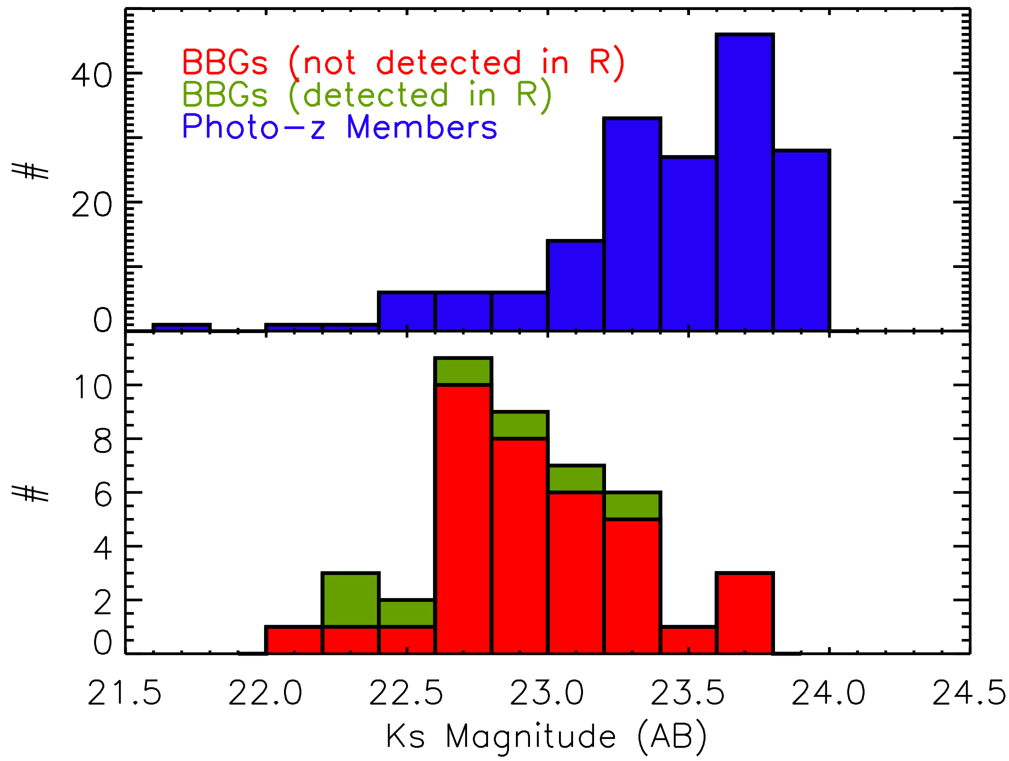

Fig. 2.5. Distribution of K_S-band magnitudes is shown for photo-z selected star-forming galaxies (top, blue histogram) and BBGs (bottom). As for the latter, those with and without R-band detection are indicated as green and red, respectively. The 2σ R band limiting magnitude is 27.2 AB. The R-band samples $\lambda_{\rm rest} \geq 1200$Å at $z \sim 3.8$.

In the K_S band, the BBGs have a mean $\langle K_S \rangle = 22.94 \pm 0.37$ AB (median 22.92), significantly brighter than the photo-z members, which have $\langle K_S \rangle = 23.44 \pm 0.40$ (median 23.50). In Fig. 2.5, we show the K_S band distribution of the photo-z (solid grey) and BBG candidates (hatched) where the BBGs are further split based on optical detection (labelled as 'UV-faint' and 'UV-bright'). The disparity between their K_S band brightness is driven by a selection effect: the IRAC color cut applied to the latter requires that they have to be bright enough in both IRAC 3.6μm and 4.5μm bands.

We construct the median SED for each BBG subsample by creating median image stacks and measuring aperture photometry [123]. The CIGALE software is run in the same manner as done for individual galaxies. The SED fitting results are summarized in Table 2.4.1. We find that optically faint BBGs are well fit by old stellar populations with little to no star formation, while the remaining seven galaxies are best-fit as young post-starburst systems. We refer to the two groups as 'quiescent' and 'post-starburst' BBGs, respectively. In the next two subsections, we discuss each category in further detail.

Table 2.1.
Physical properties of BBGs (stacked photometry)

SFH	Quiescent exp. decl. $\propto \exp[-t/\tau]$	Post starburst two populations $= C_{\rm old} \exp[-(t-t_{\rm old})/\tau_{\rm old}]$ $+ C_{\rm new} \exp[-(t-t_{\rm new})/\tau_{\rm new}]$	 exp. decl. $\propto \exp[-t/\tau]$	 CSF $= const$
$z_{\rm phot}$	3.58 ± 0.37	3.96 ± 0.26	3.95 ± 0.26	3.95 ± 0.26
$\log[M_{\rm star}/M_{\odot}]$	11.20 ± 0.07	10.99 ± 0.09	10.99 ± 0.10	10.95 ± 0.09
SFR ($M_{\odot}$ yr^{-1})	0 ± 2	114 ± 61	110 ± 69	172 ± 68
Age (Myr)	984 ± 324	395 ± 141	405 ± 154	358 ± 127
E$(B-V)$	0.08 ± 0.08	0.16 ± 0.04	0.16 ± 0.05	0.19 ± 0.03
τ (Myr)	50	100, 300	500	∞
$f_{\rm new}{}^{\dagger}$	-	≤ 0.1	-	-
χ_r^2	6.39	5.22	5.29	5.38

† the fraction of stellar mass formed in the second burst relative to the older population.

2.4.2 Quiescent Galaxy Candidates

In Fig. 2.6, we show sample postage stamp images of the quiescent BBGs. Most of the quiescent BBG candidates are detected only in 3 or 4 bands; the limited dynamic range in the wavelength coverage and shallow depths in the IRAC 5.8μm and 8.0μm bands result in poorly constrained photometric redshift estimates. While we return to the issue of redshift degeneracy later in this section, we fix the redshift of all quiescent BBGs to $z = 3.8$ in deriving their physical parameters, which is motivated by the

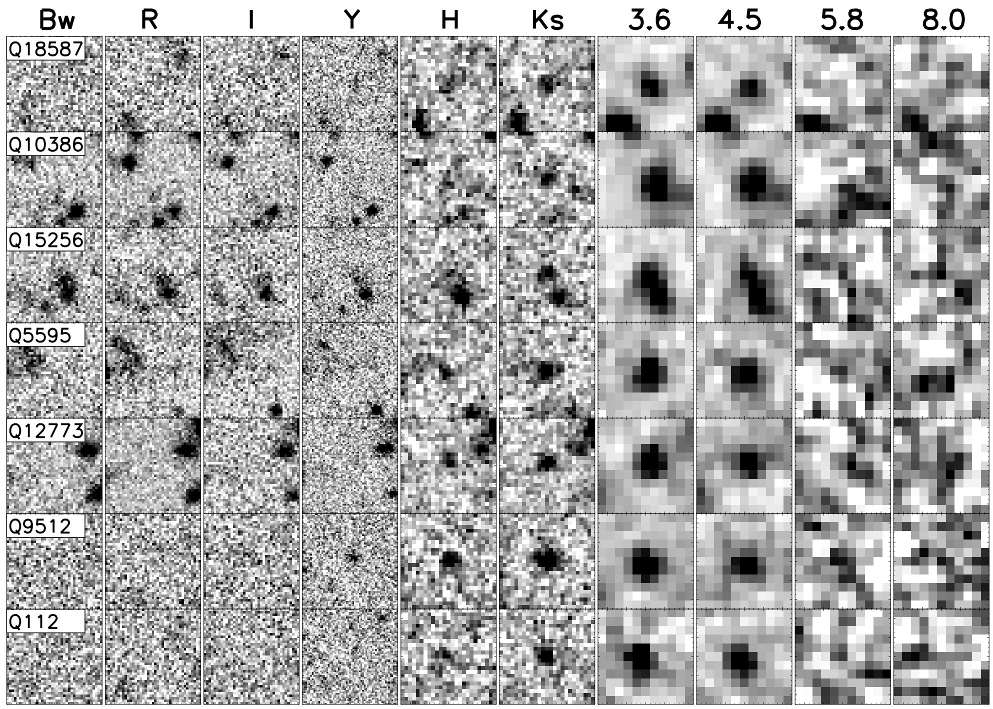

Fig. 2.6. Postage-stamp images of example quiescent BBG candidates. All images are 10″ on a side (north is up and east is to the left).

redshift of the protocluster in the field. Changing the redshift by $\Delta z = \pm 0.1$ would result a 5% change in mass.

Twelve BBGs show an excess flux in the 5.8μm and 8.0μm bands suggesting possible contamination by warm dust emission, possibly arising from hidden starburst or AGN. When we exclude the 5.8-8.0μm data from the SED fitting and refit their masses, the change in stellar mass is minimal (6%). This is consistent with the expectation based on infrared SEDs of high-redshift starburst/AGN systems that the flux contribution by AGN at $\lambda_{\rm rest} \leq 1-2$ μm is not significant [124,125]. The median value of the individual stellar mass measurements is log$\,[M_{\rm star}/M_{\odot}]$=11.30 ($\sigma$=0.29), consistent with that obtained from the stacked photometry (Table 2.1). The four most massive galaxies lie in the range log$\,[M_{\rm star}/M_{\odot}]$=11.7–11.9 (see Fig. 2.3); if confirmed, their masses already rival some of the brightest cluster galaxies in the local universe.

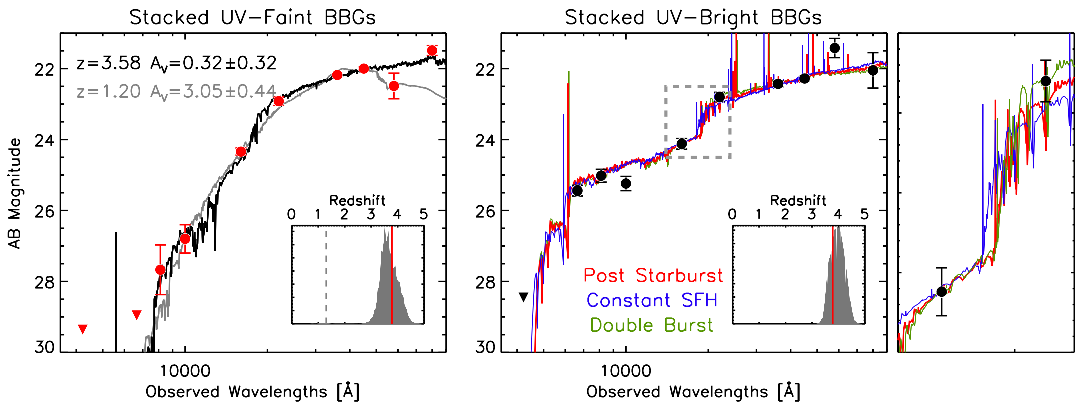

Fig. 2.7. Photometry performed on image stacks created for BBG candidates are shown together with the CIGALE-derived best-fit SEDs. Inset shows the redshift PDF as grey histogram where the redshift of PC217.96+32.3 is marked as vertical red line. *Left:* the median-stacked SED of the 36 optically faint BBGs is consistent with that of a very massive and evolved galaxy at $z \sim 3.6$ (black). The SED of an old and very dusty galaxy at $z = 1.2$ is shown in light grey, highlighting its similarity in optical and IR color to a quiescent galaxy at $z \sim 3.6$. However, for the lower redshift ($z < 1.5$) solution, a turnover in the grey model falls between $4.5 - 5.8\mu$m due to the stellar bump in the rest-frame 1.65μm. *Right:* the median-stacked SED of the 7 optically bright BBG candidates is shown with three best-fit models, namely post-starburst (red), constant SFH (blue), and double-burst (green); all three models have very similar SED shapes except for subtle differences near the Balmer/4000Å break. A zoom-in of the region outlined by a grey dashed box is shown on right (see §2.4.3).

The stacked SED of the UV-faint BBGs is consistent with an old (980 Myr) and very massive ($\approx 2 \times 10^{11} M_\odot$) galaxy with little star formation. When combined with the best-fit photometric redshift at $z_{\rm phot} = 3.58$, the formation redshift is at $z_{\rm f} \approx 6$. While similarly massive and old galaxies have been reported in the literature [117, 126, 127], the presence of such massive galaxies in large number may pose a considerable challenge to the hierarchical theory of galaxy formation.

The redshift PDF of the stacked SED (Fig. 2.7, left inset) is singly peaked at $z \approx 3.6$ strongly ruling out a lower-redshift ($z < 3$) solution. This gives us confidence that our quiescent galaxy sample is not dominated by heavily obscured lower-redshift sources. However, the photo-z constraints on individual galaxies are more ambiguous (Fig. 2.3). Only eleven of the thirty six galaxies have a singly peaked PDF at $z > 3$; the remainder shows a rather flat z-distribution or has two peaks. For the latter, the low-redshift solution typically lies at $z_{\rm phot} = 1.0 - 1.5$ and the high-z solution lies at $z_{\rm phot} = 3.5 - 4.0$.

The color degeneracy between an old quiescent galaxy at high redshift and a very dusty galaxy at lower redshift is well known. Dunlop et al. (2007) [128] reanalyzed the photometric data of a putative massive and quiescent galaxy at $z = 6.5$ named HUDF-JD2 [129], and showed that a very dusty ($A_V = 3.8$) galaxy at $z \sim 1.5 - 2.5$ is equally likely. The galaxy was later detected in the 16 μm and 22 μm bands lending further credence to the lower-z solution [130]. Similarly, Marchesini et al. (2010) [126] selected a sample of massive galaxies at $z = 3 - 4$ using the photometric redshift technique, and noted that nearly a half are equally well fit by very old and very dusty ($A_V \approx 3$) galaxies at $z < 3$, if such models are included in the spectral template set.

In the redshift range to which our BBG selection is sensitive, the strongest constraint comes from the IRAC 5.8μm and 8.0μm photometry. For galaxies at $z \leq 1.5$, these bands sample beyond the 1.65μm stellar bump which arises from the declining H^- ion opacity in the stellar atmosphere [131]. Indeed, when we repeat the SED fitting procedure while limiting the redshift range to $z < 2$, the best-fit solution is an old and heavily reddened galaxy at $z \approx 1.2$ ($A_V = 3.1 \pm 0.4$, 2.5 ± 1.4 Gyr) which is shown in Fig. 2.7 (left). Given the similarity of the rest-frame UV and optical colors of the two model fits, it is evident that flux measurements in the 5.8μm and 8.0μm band are important in breaking the redshift degeneracy.

Indeed, all of the BBGs with the 8.0μm detection have singly peaked redshift PDFs. In the image stack of the remaining 25 galaxies, we do not obtain a clear detection, and as a result, the redshift PDF is doubly peaked confirming our expectation. However, the non-detection is not surprising considering the sensitivity of the SDWFS data (5σ limit for a point source is 20.25 mag). If we assume Poisson noise (i.e., the most optimistic case), stacking 25 sources would result in the limiting magnitude of 22.0, which is very close to the measured 8.0μm flux from the full stack (see Fig. 7). Thus, the non-detection does not rule out the possibility that these 25 galaxies have similar SEDs to the 8.0μm-brighter counterparts but with slightly lower fluxes.

As a final check, we repeat our image stacking, photometry, and SED fitting procedure for 200 times while each time randomly excluding 7 BBGs (20% of the sample). We integrate the redshift PDF above $z = 3$ to obtain the formal probability P_3 for the high-redshift solution. In 73% of the time, the photometric redshift solution prefers the high-z solution ($P_3 \geq 0.5$). We conclude that the redshift ambiguity of the BBGs is mainly driven by the existing depth at the 8.0μm band and that deeper data will be necessary to place more stringent constraints on their redshift distribution.

Finally, we note that several studies reported a significant fraction of MIPS 24μm detections among massive quiescent galaxies [117, 126, 132, 133]. At z=3.0–4.5, the 24 μm samples $\lambda_{\rm rest} \approx$4–6 μm, where warm-hot dust continua or polycyclic aromatic hydrocarbons excited by star formation or AGN activity could contribute significantly to the flux. Exploration of such possibilities offers a promising avenue to learn about how the 'red-and-dead' galaxies form and what roles AGN activity and nuclear starburst plays in the process. We notice the submillimeter (ALMA+SCUBA2) detection a fraction of an arcsecond away from a confirmed post-starburst galaxy has been reported recently [127]. However, given the shallow MIPS coverage in the Boötes field (5σ detection limit is 250μJy), we are unable to quantify what fraction of our BBG candidates may harbor hidden AGN or starbursts.

2.4.3 UV-bright Balmer Break Galaxy Candidates: Post-starburst or normal star-forming galaxy?

The relatively strong Lyman break present in the seven optically bright BBGs places their redshift in the range $z_{\rm phot}$=3.6–4.0, giving us confidence that the H and K_S bands straddle the Balmer/4000Å break. The overall chi-square distribution obtained from our SED fitting procedure suggests that either delayed or exponentially declining SFH models with relatively short τ values (100–300 Myr) are preferred over constant SFH models, where the latter typically returns larger χ_r^2 values. The median fit value are $\log[M_{\rm star}/M_\odot]$=11.0 ($\sigma$=0.2) in stellar mass, 145 (σ = 42) $M_\odot$yr^{-1} in SFR, and 433 Myr (σ =23 Myr) in population age. In comparison, the CSF model returns higher values of SFR 205 (σ = 67) $M_\odot$yr^{-1} but similar stellar masses and ages. These values are also consistent with the stacking results shown in Table 2.1.

In Fig. 2.7 (right), we show the stacked photometry together with the best-fit SEDs assuming CSF (blue) and exponentially declining (red) models. The overall SED shapes are very similar in the entire range of the rest-frame UV-to-IR wavelengths with the exception of the K_S band sampling the rest-frame 4500Å. A zoom-in on the wavelength range near the Balmer/4000Å break is shown in the far right panel.

We also consider a scenario in which the galaxies are composed of two stellar populations formed at different times where the old population dominates the rest-frame optical emission while the UV emission originates from newly formed stars [134]. We explore a range of 'double burst' models as follows: the SFHs of both populations are modelled as exponentially declining functions with τ values ranging in $\tau = 10 - 1000$ Myr. The ages of the two populations are also allowed to vary. The fraction of stellar mass formed in the second burst relative to the old population, $f_{\rm new}$, is varied from 0.01 to 0.50. The minimum χ^2 is achieved at $f_{\rm new} \approx 0.05$ where a 200 Myr-old new burst is currently forming stars at rates of 114 $M_\odot$yr^{-1} (green line in Fig 2.7, right panel). The χ^2 values are similar out to $f_{\rm new} \leq 0.1$, but increase more rapidly at $f_{\rm new} \geq 0.2$ ($\Delta\chi^2 = 0.4$ and 0.9 at $f_{\rm new} = 0.2$ and 0.3, respectively). Thus, we conclude that the mass formed during the recent SF episode is small (<10%) compared to that of the evolved stellar population. The stellar population parameters obtained for all three different star formation histories are listed in Table 2.1.

Finally, we consider the possibility that the seven optically bright candidates are normal star-forming galaxies misclassified as BBGs due to the contamination of the K_S band flux by strong nebular emission such as [O III] and Hα [135–137]. Of particular interest to the present sample is the [O III] $\lambda\lambda 4959, 5007$ doublet, which falls into the K_S band at $z = 3.1 - 3.6$.

For all but two, the redshift PDF peaks at $z \geq 3.7$ even though the majority has a non-zero probability of lying in the range $z_{\rm phot} = 3.5 - 3.6$. For the remaining two, the peak of the PDF is $z \sim 3.6$. Schenker et al. (2013) [137] measured the rest-frame [O III] equivalent widths (EWs), and determined the median value of 280Å [138]. At $z = 3.5$, it would lead to a substantial overestimation of the K_S band continuum flux by 0.37 mag.

However, Malkan et al. (2017) [139] recently noted that a strong anti-correlation exists between [O III] EW and stellar mass such that the EW could be as low as 80Å in $M_{\rm star} \approx 10^{10}{\rm M}_\odot$ galaxies. The median stellar mass of our UV-bright BBGs is nearly an order of magnitude larger than this value. Similarly, only two galaxies in the Schenker et al. sample have UV brightness similar to our sample[2] whose EWs are 100Å and 150Å corresponding to a much less severe contamination of Δm of 0.15 and 0.21 mag, respectively. The trend of decreasing EWs with increasing mass and UV luminosity is likely the same, given the relatively tight correlation between the two quantities among star-forming populations [106, 140, 141].

We measure the mean [3.6]−[4.5] color to be 0.24 ± 0.16; Stark et al. (2013) [136] reported that the median [3.6]−[4.5] color is ≈ -0.23 mag for $3.8 < z < 5.0$ galaxies, significantly bluer than the ~ 0.1 mag color measured in their sample for the systems at $3.1 < z < 3.6$. The color difference is attributed to the presence of strong Hα emission in the former. The lack of excess 3.6μm band flux corroborates the possibility that nebular line contamination is not significant.

Given the color degeneracies between the above possibilities, discriminating a young post-starburst from a rejuvenated old galaxy will be harder, requiring detection of their respective spectroscopic signatures; these will include Balmer absorption lines for post-starburst galaxies [127, 134] and nebular lines such as [O II], [O III], Hβ, and

[2]The z_{850} magnitudes of the Schenker et al. galaxies are 24.4 and 25.3 AB; the magnitude range of our UV-bright BBGs is $I = 25.2 \pm 0.4$ and $Y = 25.0 \pm 0.6$ AB.

Hα, from the H II regions. Future James Webb Space Telescope spectroscopy will help resolve this issue unambiguously [142].

Regardless of their nature, we have uncovered a rare population of ultra-massive galaxies ($\sim 10^{11} M_\odot$) which may have recently halted their star formation, or are nearing the end of their star-formation activity.

A summary of all the 43 BBG candidates is given in Table 2.2.

2.5 A Massive Galaxy Overdensity?

2.5.1 Sky Distribution of Protocluster Candidates

We show the sky distribution of the photo-z protocluster candidates in the left panel of Fig 2.8; the surface density enhancement relative to the mean density is shown as both greyscale and contour lines. The true density enhancement is expected to be higher as the mean density computed from the entire field includes the galaxies in the overdense region. There is a clear indication of a large overdensity slightly south of the field center, outlined by the $1.5\bar{\Sigma}$ and $1.7\bar{\Sigma}$ lines. A smaller less significant one is found north of the field center. In the same figure, the sky distribution of known members of PC217.96+32.3 is shown in the middle panel; spectroscopic sources (which include both LAEs and LBGs) are color-coded by redshift. The density contour of the protocluster is constructed as before, but only using the LAE positions. Because our spectroscopic efforts were heavily focused on the LAE overdensity region, including the non-LAE members in the density calculation would artificially increase the overdensity.

Comparing the density maps of the photo-z and of protocluster LAEs, it is evident that they are not co-spatial. We perform a two-dimensional Kolmogorov-Smirnov (K-S) test [143, 144] to compare the the photo-z distribution with the LAE distribution, and find the p-value of 2.9×10^{-7}. Thus, it is extremely unlikely that they are drawn from the same parent distribution at random. The 2D K-S test has also been used in [145] to compare between different structures.

Table 2.2.
Catalog of BBG candidates

ID	R.A. (J2000)	Decl. (J2000)	B_W	R	I	y	H	K_S	[3.6]	[4.5]	[5.8]	[8.0]
Q112	217.953683	32.28450	>27.41	>27.02	>26.67	>26.34	24.53±0.29	23.21±0.10	21.98±0.15	21.56±0.14	>21.23	>20.90
Q2396	217.741855	32.32550	>27.41	26.36±0.37	25.89±0.47	25.47±0.37	24.27±0.23	23.00±0.14	22.96±0.26	22.56±0.22	>21.23	>20.90
Q3161	217.721483	32.19860	>27.41	>27.02	>26.67	>26.34	24.25±0.24	22.89±0.10	21.83±0.20	21.33±0.14	–	–
Q3268	217.943585	32.34119	>27.41	26.45±0.48	>26.67	25.98±0.76	24.10±0.32	22.70±0.14	22.15±0.20	21.68±0.18	>21.23	>20.90
Q3296	217.931437	32.20151	>27.41	>27.02	>26.67	24.78±0.46	24.06±0.33	22.69±0.13	22.51±0.63	22.78±0.53	–	>20.90
P3374	217.766615	32.34254	>27.41	25.37±0.16	25.19±0.25	24.98±0.27	23.68±0.15	22.37±0.08	22.26±0.14	21.93±0.12	20.84 ±0.35	20.22±0.16
P3433	218.098397	32.20417	>27.41	26.10±0.28	25.57±0.31	26.01±0.73	24.72±0.28	23.32±0.12	22.91±0.56	22.61±0.32	–	>20.90
Q4670	217.914775	32.22440	>27.41	>27.02	>26.67	>26.34	23.89±0.23	22.63±0.08	21.52±0.18	21.43±0.15	–	>20.90
Q4943	218.106545	32.37317	>27.41	26.55±0.38	>26.67	25.55±0.41	24.88±0.40	23.29±0.22	22.68±0.27	22.31±0.26	>21.23	>20.90
Q4948	218.027168	32.22880	>27.41	>27.02	>26.67	>26.34	24.63±0.29	23.28±0.15	22.75±0.53	22.74±0.36	–	> 20.90
P5479	218.107794	32.38329	>27.41	24.91±0.21	24.94±0.24	24.85±0.27	24.61±0.35	23.14±0.17	22.92±0.27	22.42±0.24	>21.23	>20.90
Q5595	217.762752	32.38484	>27.41	>27.02	>26.67	25.67±0.53	23.86±0.18	22.55±0.08	21.69±0.12	21.43±0.11	21.05 ±0.33	20.78±0.28
Q5788	217.833271	32.38915	>27.41	26.49±0.29	26.35±0.49	>26.34	24.62±0.26	23.19±0.11	22.96±0.23	22.65±0.21	>21.23	>20.90
Q6407	217.756014	32.40108	>27.41	>27.02	25.85±0.53	26.08±0.86	>25.05	22.93±0.15	22.90±0.37	22.64±0.33	>21.23	>20.90
Q6497	217.897260	32.25346	>27.41	26.61±0.78	25.85±0.69	24.97±0.50	23.98±0.29	22.68±0.11	21.84±0.36	22.16±0.39	–	>20.90
Q6936	217.732113	32.41123	>27.41	>27.02	>26.67	>26.34	>25.05	23.76±0.22	22.99±0.29	22.57±0.26	>21.23	>20.90
Q7103	217.884829	32.41509	>27.41	>27.02	>26.67	>26.34	>25.05	23.68±0.19	23.18±0.39	22.99±0.35	20.47±0.37	>20.90
Q7163	217.902270	32.41554	>27.41	>27.02	>26.67	25.31±0.50	>25.05	22.66±0.13	22.99±0.44	22.80±0.39	21.19±0.77	>20.90
Q7361	218.138166	32.41936	>27.41	>27.02	>26.67	26.15±0.70	24.39±0.36	23.05±0.14	21.68±0.18	21.25±0.18	>21.23	20.45±0.28
Q7775	218.095899	32.42599	>27.41	>27.02	>26.67	>26.34	23.99±0.19	22.79±0.12	21.53±0.14	21.13±0.14	20.51 ±0.24	>20.90
Q7961	217.658322	32.42931	>27.41	26.61±0.45	26.22±0.57	25.72±0.54	24.54±0.27	23.26±0.18	22.66±0.28	22.70±0.29	>21.23	20.53±0.33
Q8038	217.712417	32.43066	>27.41	>27.02	>26.67	>26.34	24.22±0.28	22.77±0.13	22.15±0.19	21.69±0.18	20.36 ±0.27	>20.90
Q8068	217.871038	32.43181	>27.41	>27.02	>26.67	26.12±1.07	24.33±0.27	22.75±0.16	21.72±0.24	21.39±0.23	20.27±0.44	>20.90
Q8108	217.737275	32.27759	>27.41	>27.02	>26.67	25.70±0.57	24.23±0.27	22.93±0.15	22.43±0.24	22.03±0.19	>21.23	>20.90
Q8847	217.978870	32.44496	>27.41	>27.02	>26.67	>26.34	24.25±0.25	22.97±0.16	22.10±0.22	21.79±0.21	20.22 ±0.28	>20.90
Q9512	217.951934	32.30146	>27.41	>27.02	26.02±0.54	24.70±0.26	23.45±0.12	22.24±0.06	21.47±0.10	21.56±0.10	>21.23	>20.90
P9576	217.865190	32.45845	>27.41	25.87±0.18	25.81±0.35	25.23±0.26	24.00±0.15	22.73±0.09	23.09±0.21	22.90±0.20	20.87±0.25	>20.90
Q10133	217.948664	32.46798	>27.41	>27.02	>26.67	25.82±0.55	24.12±0.24	22.79±0.10	21.87±0.15	21.51±0.14	>21.23	>20.90
Q10226	217.807902	32.47021	>27.41	>27.02	>26.67	>26.34	24.35±0.23	22.88±0.11	22.96±0.23	22.72±0.22	>21.23	>20.90
P10316	217.867090	32.47131	26.79±0.30	25.61±0.19	25.28±0.27	25.01±0.28	23.62±0.15	22.37±0.08	22.01±0.12	21.77±0.12	20.58±0.22	>20.90
Q10386	218.147692	32.47255	>27.41	>27.02	>26.67	>26.34	23.35±0.27	22.08±0.13	20.63±0.16	20.39±0.16	20.69 ±0.52	>20.90
Q10794	217.902578	32.48004	>27.41	>27.02	>26.67	>26.34	>25.05	23.71±0.17	23.17±0.43	22.72±0.34	20.95±0.55	>20.90
Q12526	217.897738	32.50942	>27.41	>27.02	>26.67	25.98±0.60	24.65±0.48	23.34±0.18	22.39±0.24	22.37±0.27	>21.23	20.80±0.52
Q12773	218.051315	32.51337	>27.41	>27.02	>26.67	>26.34	24.04±0.18	22.83±0.09	21.82±0.13	21.49±0.12	>21.23	20.55±0.21
Q13609	217.935053	32.52815	>27.41	>27.02	26.60±0.66	25.80±0.46	24.84±0.34	23.58±0.12	23.26±0.30	22.90 ±0.26	>21.23	>20.90
P15053	218.146435	32.55216	>27.41	25.73±0.32	25.25±0.36	24.47±0.31	24.27±0.37	22.92±0.23	22.34±0.28	22.35±0.31	>21.23	>20.90
Q15256	217.728406	32.55562	>27.41	>27.02	>26.67	>26.34	24.35±0.29	22.90±0.14	22.50±0.23	22.12±0.21	>21.23	>20.90
P15333	217.810823	32.55629	27.10±0.60	24.83 ±0.22	24.57±0.27	24.13±0.26	23.84±0.31	22.59±0.16	21.93±0.23	21.76±0.23	>21.23	>20.90
Q17001	218.005890	32.58427	>27.41	>27.02	>26.67	>26.34	24.65±0.31	23.19±0.11	22.27±0.17	21.94±0.17	>21.23	>20.90
Q17800	217.704266	32.59865	>27.41	>27.02	26.59±0.84	26.20±0.81	24.59±0.29	23.11±0.12	22.08±0.18	21.64±0.17	>21.23	>20.90
Q17832	217.993321	32.59982	>27.41	>27.02	25.80±0.41	25.04±0.30	24.25±0.29	22.77±0.12	22.53±0.22	22.18±0.20	>21.23	>20.90
Q17976	218.067814	32.60220	>27.41	>27.02	>26.67	25.85±0.53	24.34±0.26	23.09±0.13	22.19±0.18	22.23±0.19	>21.23	>20.90
Q18587	218.051648	32.61501	>27.41	>27.02	>26.67	>26.34	24.07±0.31	22.84±0.14	21.66±0.21	21.30±0.20	>21.23	>20.90

Notes: The letter in front of the ID number represents the type of BBGs: 'P' for post-starbursts and 'Q' for quiescent galaxies. In the case of non-detection, the corresponding 2σ limiting magnitude is given. The sign '–' is used when a source is out of image bounds or lies in the region with less than 20% of the maximum exposure time.

The largest photo-z overdensity runs in the NW-SE direction. While it partially overlaps with the southern end of PC217.96+32.3, it stretches further west to the region devoid of the LAEs. A smaller and less significant overdensity lies just north of the main overdensity, which also overlaps slightly with a small LAE group north of the main LAE overdensity. The larger overdensity is also closer to PC217.96+32.3, and thus most likely to have a physical connection to the confirmed protocluster. Being separated from each other, the physical association of the two photo-z overdensities is unclear. Thus, we focus on the larger overdensity in this work.

The shapes and locations of the photo-z and LAE surface overdensities are suggestive of a possible physical connection. One hypothesis is that they are part of a single structure where the photo-z overdensity lies in the foreground of the LAEs (i.e., at $z < 3.76$), and as a result any Lyα emission from galaxies in this region is missed by the LAE selection filter. In the right panel of Figure 2.8, we show the narrow-band filter bandpass converted to the redshift selection function (dashed line) together with the distribution of all spectroscopic sources in the range of $z = 3.70 - 3.90$. Most of the known members residing in the LAE overdensity lie at $z = 3.775 - 3.785$, i.e., the blue half of the filter response. The southern end of PC217.96+32.3 is composed of galaxies in the redshift range where the filter response falls off steeply. Existing spectroscopy reveals that three LAEs there have the line centroids outside the narrow-band filter, but are selected as LAEs because of their high line luminosities and broad line widths. The high concentration of $z \approx 3.77$ LAEs where the two overdensities overlap provides a circumstantial evidence that the LAEs only partially trace the true extent of a single very large structure.

Another possibility is that the photo-z overdensity is located further in the foreground of PC217.96+32.3 near a LBG overdensity at $z = 3.72$. Of the ten galaxies at $z = 3.721 \pm 0.04$ within our NEWFIRM coverage, three reside within the $\Sigma = 1.7\bar{\Sigma}$ region, and additional five lie just outside the $\Sigma = 1.5\bar{\Sigma}$ contour line. The significance of this spectroscopic overdensity is difficult to assess given the limited extent and depth of the existing spectroscopy. All confirmed LBGs – including the eight galaxies at $z \approx 3.72$ – either have relatively strong Lyα emission or high UV continuum luminosities. Further lending support to this possibility is G6025 (large white circle in Fig. 2.8), one of the eight galaxies that is unusually large (end-to-end length of ∼20 kpc) [146]. The ground-based morphology and large angular size are consistent with two UV-luminous galaxies involved in a major merger, a type of event that should occur more frequently in a dense environment.

Finally, the photo-z overdensity may represent a protocluster with no physical connection to PC217.96+32.3. The stacked redshift probability density function of protocluster candidates peaks at $z \approx 3.75$, but its width is not narrow enough to rule out the possibility that the true peak may be $\Delta z > 0.1$ away from the peak value, which would place the structure at > 20 Mpc away from PC217.96+32.3.

Multiple protoclusters in close proximity are unlikely, but not impossible. Kuiper et al. (2012) [145] noted that there may be two separate galaxy overdensities near MRC 0317-257, a radio galaxy at z=3.13. Similarly, a string of galaxy overdensities in the COSMOS field was found spanning over a line-of-sight distance of ~ 25 Mpc ($z = 2.42$, 2.44, 2.47, and 2.51) [76, 147–149]. With the limited spectroscopy, their physical connection remains unclear. Two additional LAE overdensities of smaller magnitudes exist just outside our NEWFIRM field north of PC217.96+32.3 [45], one of which was confirmed to be a galaxy overdensity [46]. In § 2.6.5, we return to this topic and evaluate the likelihood of multiple protoclusters in our survey volume.

2.5.2 Sky Distribution of Balmer Break Galaxy Candidates

Several previous studies have reported a high concentration of galaxies dominated by old stellar populations near known massive protoclusters [20, 82, 149, 150]. While those galaxies still await spectroscopic confirmation, such information would have important implications to the formation histories of massive cluster ellipticals. In this context, we investigate whether our BBGs are physically associated with the structure revealed by the photo-z overdensity.

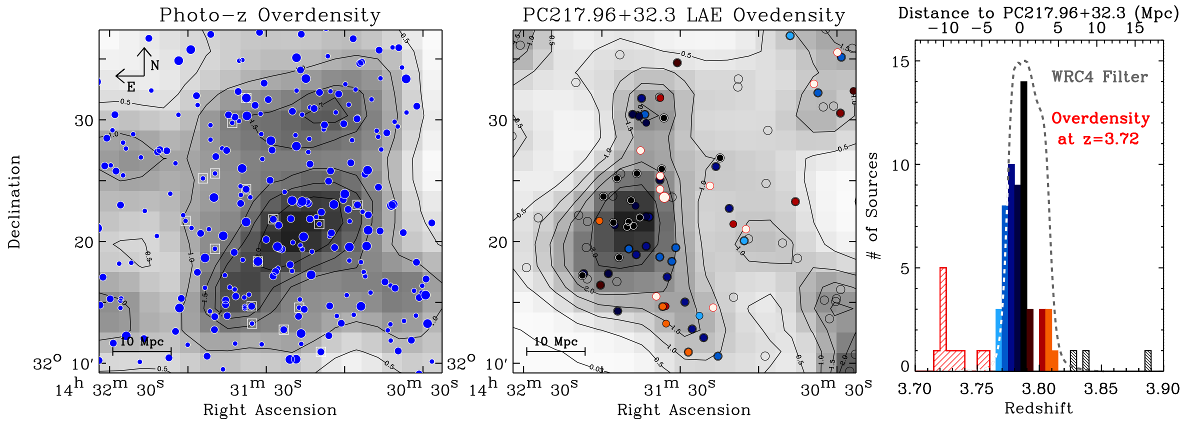

Fig. 2.8. *Left:* Grey shades and density contours show the distributions of photo-z member candidates (blue filled circles). White boxes indicate sources with known spectroscopic redshifts. The surface density map is created by smoothing the positions of each galaxy by a 4.7″-FWHM Gaussian kernel. Symbol sizes indicate galaxy's stellar masses as $M_\star < 10^{10.5}\mathrm{M}_\odot$ (small), $10^{10.5}\mathrm{M}_\odot < M_\star < 10^{11}\mathrm{M}_\odot$ (medium), and $M_\star > 10^{11}\mathrm{M}_\odot$ (large). A comoving distance scale is indicated on bottom left corner. *Middle:* density contours show the LAE distributions. The spectroscopic members are color-coded by redshift indicated in the right panel. Six LAEs near the lower redshift cutoff of our LAE selection ($z = 3.770 - 3.804$) lie close to the photo-z overdensity peak. *Right:* Histogram of spectroscopic sources at $z = 3.70 - 3.90$. Top abscissa indicates the corresponding line-of-sight distance (physical) measured from the structure redshift at $z = 3.783$. The LAE redshift selection function (dashed line) is converted from the narrow-band filter bandpass. A smaller overdensity at $z \approx 3.72$ (red hatched histogram) is identified from our spectroscopic survey; the locations of these sources are indicated in the middle panel as white symbols outlined by red circles. Among them is G6025 – an unusually large (20 kpc) galaxy at $z = 3.72$ reported by [146] – shown as the largest circle. The three sources at $z > 3.82$ (dark hatched histogram) are not LAEs and thus are not used in our analysis.

In Fig. 2.9 we show the locations of the 43 BBG candidates overlaid on the photo-z (left) and LAE (right) density maps. The BBGs seem to avoid the most overdense regions of both the LAEs and photo-z candidates. Only one quiescent galaxy candi-

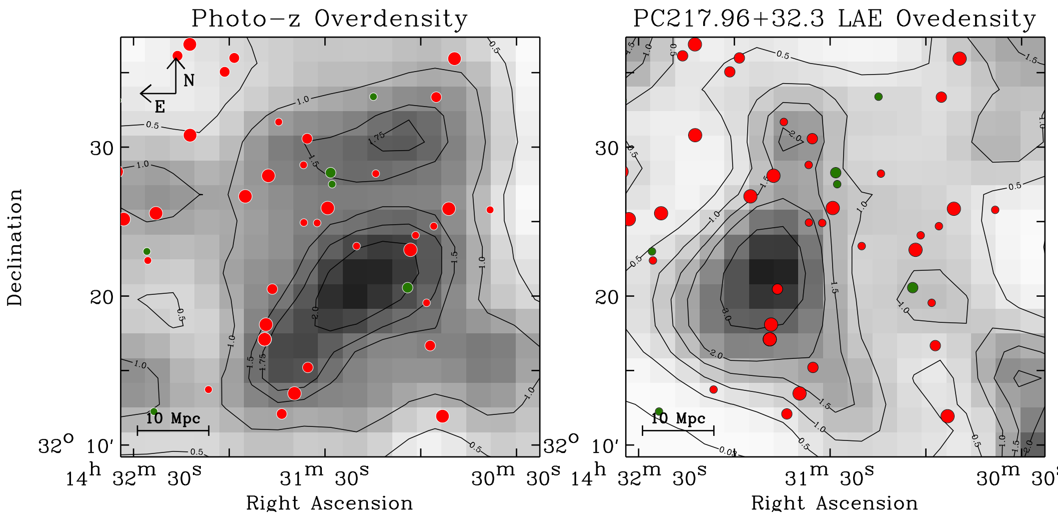

Fig. 2.9. The sky positions of the BBG candidates are overlaid on the density contours of photo-z (left) and of the LAE members of PC217.96+32.3 (right). Galaxies whose SEDs are consistent with young post-starbursts (see § 2.4) are shown in green, and quiescent galaxy candidates are indicated in red. None of the quiescent galaxy candidates is included in our photo-z sample. Large, medium, and small symbol sizes denote their estimated stellar masses corresponding to $\geq 2.5 \times 10^{11} M_{\odot}$, $(1.2 - 2.5) \times 10^{11} M_{\odot}$, and $< 1.2 \times 10^{11} M_{\odot}$, respectively.

date lies near the LAE core, and two additional sources are near the $3\bar{\Sigma}_{\rm LAE}$ line. Only three BBG candidates locate near the $2\bar{\Sigma}_{\rm photoz}$ contour line. The relative void of all types of galaxies potentially associated with the structure in the southern corner and northern end of the field is also noteworthy. The fact that the same regions are well populated with lower-redshift sources perhaps suggests that the void is not artificially created by the presence of bright sources such as saturated stars or large galaxies.

We perform a 2D K-S test using the BBG and LAE distributions, and find the p-value of 3×10^{-4}, indicating the significant disparity between the spatial distributions of the two samples. The same test using the BBG and photo-z distributions result in the p value of 0.05. The K-S test evaluates the similarity of two univariate samples by constructing their cumulative distributions and computing their maximum distance. Because multivariate samples can be ordered in more than one way, multi-dimensional

K-S tests lack the statistical rigor of the 1D test, and thus need to be understood in the context of carefully controlled tests. To this end, we populate the survey field with two *a priori* known distributions and perform the 2D K-S test to quantify the range of the p values. For each test, we create 1,000 separate realizations.

First, we create two random distributions, each matching the number of BBGs and photo-z sources. We obtain the mean (median) p value of 0.30 (0.27) with the standard deviation (σ) of 0.21. Second, we compare the photo-z sample with a randomly chosen subset of itself consisting of 43 sources (matching the number of BBGs), which result in the p value of 0.37 (0.36; $\sigma = 0.21$). These tests suggests that we can reliably rule out the possibility that the LAEs and BBGs – having 3×10^{-4} – are drawn from the same parent distribution.

The relationship between the BBGs and photo-z candidates, however, is less clear with $p = 0.05$. Comparison of the photo-z distribution with 43 randomly distributed sources yields the p value of 0.11 (0.07, $\sigma = 0.12$), comfortably bracketing the measured p value. Thus, we cannot statistically rule out the possibility that the BBG positions are not correlated with those of photo-z members. Spectroscopic redshifts are necessary for progress.

2.5.3 Estimate of true overdensity and descendant mass

We assess the significance of the structure by estimating the range of the true galaxy overdensity given the observed level of the surface density enhancement. The transverse size of the photo-z overdensity is computed by interpolating the $1.5\bar{\Sigma}$ isodensity contour, which yields 139 arcmin^2 or 26.4 Mpc^2 (physical) at $z = 3.78$. Since physical scale remains constant within 2% at $z = 3.65 - 3.85$, our subsequent estimate of the overdensity and masses should be relatively insensitive to the precise redshift of the structure. We assume that the line-of-sight distance from the front to back of the structure is 15 Mpc; this is motivated by the fact that the effective diameter of the progenitors of massive present-day clusters lies in this range [37]. The redshift distribution of the known members of PC217.96+32.3 ranges over $z = 3.77 - 3.79$ is consistent with this expectation (see the right panel of Figure 2.8).

We infer the range of the intrinsic galaxy overdensity by performing Monte Carlo simulations as follows. In each run, we create a mock field containing one protocluster with a galaxy overdensity δ_g in the middle by populating points randomly in the (α, δ, z) space. The "protocluster region" is defined as a rectangle. The overall number of sources and the transverse area of the protocluster match those of the data. An intrinsic galaxy overdensity, δ_g, is chosen at random in the range $\delta_g = 1 - 20$. We divide the redshift range $[3.4, 4.2]$ into 40 bins with a binsize of $\Delta z = 0.02$, corresponding to the stepsize of 15 Mpc in comoving line-of-sight distance. Taking δ_g as intrinsic overdensity, the number of true members is $N_{\rm proto} = (1+\delta_g)N_{\rm phot}/(40+\delta_g)$ where $N_{\rm phot}$ is the total number of observed protocluster candidates in the field, and populate them at random within the protocluster region. Setting $\delta_g = 10$ (5) means that 58 (35) galaxies are part of the structure. The remainder ($N_{\rm phot} - N_{\rm proto}$) are assigned randomly assuming a uniform distribution in both transverse and line-of-sight positions. We construct the surface density map of the mock image using the identical procedure as described previously, and estimate the mean surface density enhancement within the protocluster region.

We repeat the above procedure 10,000 times and obtain the empirical relation between the true overdensity and surface overdensity. The scaling relation is well-behaved and nearly linear. Given the observed surface overdensity (the mean enhancement is 1.81 within the $1.5\bar{\Sigma}$ iso-density contour), we estimate that the intrinsic overdensity of the structure is $\delta_g = 5.5 - 10.2$ with the median value of 7.8. The value is comparable to the redshift overdensities found for several known protoclusters. Steidel et al. (2005) [20] measured a redshift overdensity of $\delta_g \sim 7$ for a $z = 2.30$ structure. Based on the VIMOS Ultra Deep Survey [151], Lemaux et al. (2014) [33] and Cucciati et al. (2014) [40] reported the inferred redshift overdensity of $\delta_g = 10.5 \pm 2.8$ and $\delta_g = 12 \pm 2$ for a protocluster at $z = 3.28$ and $z = 2.90$, respectively. These values are larger than that determined for the SSA22 protocluster at $z = 3.09$, $\delta_g \sim 3.5 - 4.0$ [38, 39, 86, 152–154].

To investigate how sensitive the inferred δ_g value is to the transverse area of the surface overdensity, we rerun the simulations using the iso-density of $1.3\bar{\Sigma}$ and $1.6\bar{\Sigma}$; lowering the density contrast effectively increases the effective area, while raising it has the opposite effect. We find that the estimate of the underlying overdensity is relatively insensitive to a specific choice of density contrast used to estimate the extent of the structure. However, our test does not include the possibility that the surface overdensity is systematically overestimated either due to Poisson shot noise or a superposition of another unrelated group of galaxies. Given the lack of spectroscopy in the region, we currently have no way of quantifying this possibility. If the surface overdensity region is reduced by 20%, the δ_g value would decrease to 3.9–7.0.

Based on the inferred galaxy overdensity δ_g, we estimate the descendant mass of the underlying structure, i.e., the total mass enclosed within the overdense region which will be gravitationally bound and virialized by $z = 0$, which can be expressed as:

$$M_{z=0} = (1 + \delta_m)\langle\rho\rangle V \tag{2.1}$$

where $\langle\rho\rangle$ is the average matter density of the universe ($= [3H_0^2/8\pi G]\Omega_0$), δ_m is the matter overdensity, and V is the comoving volume of the galaxy overdensity. With the adopted cosmology, Equation 3.6.1 is equivalent to $M_{z=0} = [3.67 \times 10^{10} M_\odot]$ $(1 + \delta_m)$ $[V/(1\ \mathrm{cMpc})^3]$. The two overdensity parameters, δ_g and δ_m, are related through the equation $1 + b\delta_m = C(1 + \delta_g)$ where C denotes a factor correcting for the effect of redshift-space distortions [38], and b is galaxy bias. Given the lack of details to assume otherwise, we use the C in the case of spherical collapse: $C(\delta_m, z) = 1 + \Omega_m^{4/7}(z)[1 - (1 + \delta_m)^{1/3}]$. As for galaxy bias, we adopt $b = 3.5$. Our choice is justified by the fact that the majority of our photo-z sources lie in the observed UV luminosity range comparable to those of $L \geq L^*_{\mathrm{UV}}$ LBGs at $z = 3 - 4$. The bias value of the latter has been estimated through measurements of their clustering properties [155–157]. We solve the above equations for δ_g and use Equation 2.1 to obtain the mass estimate.

The enclosed mass in the photo-z structure is $(7.9 \pm 1.0) \times 10^{14} M_\odot$ given the overdensity δ_g of 7.8 ± 2.4. The inferred dark matter overdensity is $\delta_m = 1.39 \pm 0.3$. Increasing the bias value to $b = 4$ would decrease the mass by 10%.

2.6 Discussion

2.6.1 The prevalence of massive quiescent galaxies in protocluster environment

We evaluate how the number of massive quiescent galaxies ($\geq 10^{11} M_\odot$) in our field compares with that expected in an average field. Based on K_S-selected galaxies in the 1.6 deg^2 COSMOS/UltraVISTA field, Muzzin et al. (2013) [158] estimated that at $z = 3 - 4$, the cumulative number density of galaxies with $M_{\rm star} \geq 10^{11} M_\odot$ is $(1.4^{+2.2}_{-0.5}) \times 10^{-6}$ Mpc^{-3}. In our survey field ($28' \times 35'$), one expects to find $2.5^{+3.9}_{-0.8}$ BBG-selected quiescent galaxies. Similarly, Spotler et al. (2014) [159] identified 6 quiescent galaxies above $M \geq 10^{11} M_\odot$ in the ZFOURGE survey corresponding to the surface density of 0.015 ± 0.006 arcmin^{-2}, such that 3.7 ± 1.5 quiescent galaxies are expected in our field. We assume in the above calculations that the selection function takes the form of a top hat filter in the range $z = 3.6 - 4.2$ where the $H - K_S$ color samples the Balmer/4000Å break. The relative change of angular diameter distance in this range is 6%, and should result in 12% in the expected number depending on the redshift distribution of BBGs.

Taking the Muzzin et al. (2013) [158] measurement as the field average, the implied overdensity of massive quiescent galaxies is $\delta\Sigma_{\rm BBG} \sim 16$! Excluding all of our post-starburst BBG candidates (assuming all are strong [O III] emitters at $z \sim 3.4$), the remaining BBGs correspond to $\delta\Sigma_{\rm BBG} \approx 13$. Using the Spitler et al. (2014) [159] estimates, the overdensity is $\delta\Sigma_{\rm BBG} = 11$ (9) with (without) the potential [O III] emitters.

We also compare the observed abundance of quiescent galaxies with that measured in the SSA22 protocluster at $z = 3.09$. Kubo et al. (2013) [82] used color criteria tuned to $z \sim 3$ ($i' - K > 3$, $K - [4.5] < 0.5$, and $K < 23$), and identified 11 massive galaxies ($> 10^{11} M_{\odot}$) concentrated near the overdensities of other types of galaxies with the surface density of 0.10 ± 0.03 arcmin^{-2}. In comparison, the overall surface density of BBGs in our field is 0.06 ± 0.01 arcmin^{-2}. Within a smaller rectangular region ($15' \times 16'$) in which the surface density of photo-z sources is enhanced by 50% (Figure 2.9, left), we find 21 quiescent BBGs there in, corresponding to the surface density of 0.09 ± 0.02 arcmin^{-2}. All errors are given assuming Poisson shot noise. Considering the change of angular diameter distance, the surface density per unit comoving transverse area is 0.027 ± 0.008 Mpc^{-2} and 0.021 ± 0.004 Mpc^{-2} for the SSA22 and the present structure, respectively. Similarly, Lemaux et al. (2014) [33] estimated that the implied overdensity of massive ($\geq 10^{10.8} M_{\odot}$) red galaxies in a $z = 3.29$ protocluster is $\delta_g = 25.1 \pm 15.2$.

A large population of massive quiescent galaxies found in our field implies that the formation of cluster galaxies occurred in shorter timescales and at earlier times than the field galaxies. Our results confirm an early onset of cluster red sequence [33, 160]. This is in a broad agreement with star formation histories of present-day cluster ellipticals inferred from absorption line studies [56]. Little to no evolution of the cluster red sequence out to $z \sim 1.4$ further strengthens this expectation [55, 161].

The sky distribution of BBGs appears to trace the full extent of the large scale structure rather than being concentrated in the highest density environments. Few are found in either LAE or photo-z overdensity peaks (see §2.5.2). We speculate that BBGs may be the central (and most massive) inhabitants of the massive halos that are in the process of merging. The implication is that they were quenched long before the final coalescence of the structure which occurred much later. Therefore, the quenching of massive cluster ellipticals is caused by the early onset of the 'mass quenching' rather than by any environmental effect suppressing their formation [162]. This is in line with a study of intermediate-redshift galaxy clusters by [163], who found that the level of star formation in cluster environment declines below that in the average field only at $z < 1.4$ [29]. Recent discoveries of compact galaxy groups in protocluster environments support this view, as a fraction of quiescent galaxies in such a group is observed to be low [149, 164].

2.6.2 Diverse types of galaxies tracing a massive protocluster

In this work, we have identified protocluster member candidates by employing two selection methods, namely photo-z selected star-forming galaxies and Balmer break galaxies. When combined with a population of LAEs in the same field [45, 46], these samples showcase diverse types of inhabitants residing in a very overdense cosmic structure.

In Fig. 2.10, we show SFR, stellar mass, and sSFR values measured for our sample galaxies. The estimates for the photo-z candidates are made on individual galaxies. As for the quiescent BBG candidates, we fix the redshift to $z = 3.8$ for the SED fitting (see § 2.4.2 for discussion on redshift degeneracy); for the UV-bright BBGs with robust photo-z estimates, we fix the redshift to the best-fit value.

As for the LAEs, while they have robust redshift estimates, they are too faint at infrared wavelengths to yield robust estimates of stellar population parameters on an individual basis. Instead, we perform image stacking on their positions, and measure the parameters based on the aperture photometry on the stacked images. A total of 150 LAEs are used for stacking analysis after removing those too close to nearby bright sources. To estimate the range of their physical parameters, we randomly draw a subset of the LAEs, and perform image stacking, aperture photometry, and SED fitting procedure. Their distributions of stellar population parameters shown in Figure 2.10 are based on 2,500 such realizations. Since median stacking is insensitive to significant outliers, the distribution of their physical parameters should be taken as a lower limit rather than the full range spanned by the LAEs.

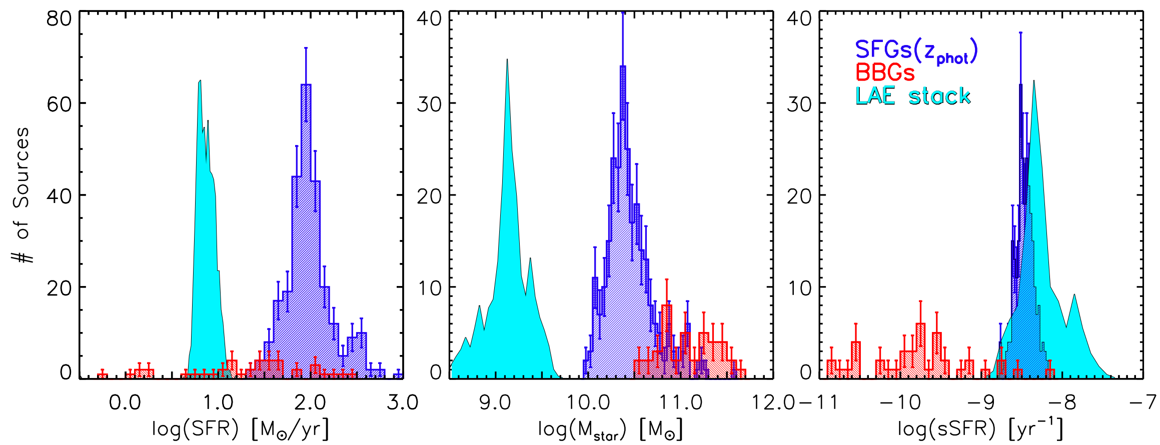

Fig. 2.10. The distributions of star formation rates (left), stellar masses (middle), and specific SFRs (right) are shown for the LAE protocluster members (cyan) and photo-z protocluster candidates (blue) and BBG candidates (red). The errors reflect the Poisson uncertainties. For clarity, finer binsizes are used for the photo-z sources than for the BBGs. As for the LAEs, stellar population parameters are derived from bootstrap realizations of image stacking analyses (see text). In all panels, the LAE distribution is rescaled to have the same peak height as the photo-z members.

The sample galaxies span a wide range of SFRs and stellar masses: the lack of overlap is at least in part driven by the selection effect. The lack of photo-z candidates at $M_{\rm star} < 10^{10} M_\odot$ is tied to the sensitivity of our K_S band data. A 10σ detection ($K_{S,\rm AB}$=24.0) corresponds to the rest-frame optical luminosity of a $z = 3.8$ galaxy with stellar mass $\approx 10^{10.2} M_\odot$, assuming an exponentially decaying star formation history with the τ value of 0.5 Gyr. The paucity of galaxies with SFR $< 50\ M_\odot \rm yr^{-1}$ is also driven by the same mass limit, given the correlation between SFR and $M_{\rm star}$. The large median mass of the BBGs is driven by the IRAC color selection as discussed in Sec 2.4.1. The steep decline in the number of galaxies at SFR $> 150\ M_\odot \rm yr^{-1}$ [165] is likely further helped by the photo-z selection which is biased against redder (dustier) galaxies than typical LBGs. The intrinsic distribution of these parameters spanned by different types of galaxies remains uncertain: such information will require careful analyses of deeper multiwavelength data and the modeling of their respective selection biases, which are outside the scope of this paper.

The measured overdensities of different galaxy types highlight how they trace the same underlying large scale structure(s). Such measures are more robust against any selection biases mentioned previously as any such bias should apply equally to field and cluster galaxies, and thus should minimally impact their spatial distributions. The observed surface overdensity of photo-z galaxies is $\delta\Sigma_{\rm phot} \approx 1.5$, similar to that of the LAEs over the same general area. However, we show in § 2.5.3 that the spatial overdensity of the photo-z galaxies is much larger, $\delta_g = 7.8 \pm 2.4$, than that of the LAEs. This is because the former is distributed over a much larger line-of-sight distance (i.e., larger Δz), and as a result, its surface overdensity is substantially diluted by the interlopers. It is also possible that the narrow band Lyα filter 'misses' the core of the protocluster, and is only picking up the outer parts of the protocluster. In comparison, the surface overdensity of BBGs of the region is much higher at $\delta\Sigma_{\rm BBG}$ $\approx$9–16.

If all types of galaxies we consider here (LAEs, BBGs, and photo-z candidates) trace the same underlying structure represented by a matter overdensity δ, the implication would be that more massive BBGs are far more biased tracers of the matter distribution than less massive star-forming galaxies. Our findings are consistent with the expectation from existing clustering studies, that more luminous/massive galaxies have larger biases [50, 155, 156, 166–169].

One corollary to the luminosity/mass-dependent bias is that, everything being equal, low-mass low-bias galaxies such as LAEs are the least biased (thus most reliable) tracers of the density distribution within the large-scale structure. Using LAEs to 'map out' the protocluster environment has additional advantages including the relative ease of redshift identification through the narrow-band selection technique and the abundance of low-luminosity galaxies implied by the steep faint-end slope of the UV luminosity function at this redshift range [139, 170–172]. Given the difficulties of obtaining spectroscopic redshifts for faint distant galaxies, LAEs offer the best practical means to survey the local environment of massive protoclusters, thereby allowing for studying the impact of local environment on its galaxy constituents [82, 164, 173]. While large numbers of protocluster candidates are being identified from wide-field deep surveys [47, 174], the lack of narrow-band observations targeting these structures will remain a main challenge in utilizing these structures to elucidate the physics in the main epoch of cluster formation.

2.6.3 Impact of local environment on stellar populations

The primary challenge in investigating the environmental effect on protocluster constituents is the lack of spectroscopic redshifts, which prevents unambiguous confirmation of cluster membership and inhibits a robust mapping of the density profile of the cluster. Because our selection methods target a relatively broad range of redshift, all galaxy samples are expected to contain and may be even dominated by interlopers not associated with the structure we wish to probe. These considerations testify to the clear need of spectroscopic information in making progress.

One possible way to discern any environment trend is to compare the galaxy statistic measured in a protocluster field with that obtained in a field without any strong density enhancements.. Provided that the environmental effects are strong and a substantial number of galaxies in the sample belong to the protocluster, a qualitative trend may be identified through this comparison [176]. However, a comparative study is only meaningful if the two datasets are well matched in depth, dynamic range, and wavelength coverage, which determine the precision with which photometric redshifts and stellar population parameters of the galaxies can be measured.

With these caveats in mind, we compare the properties of protocluster candidates with those of a control sample. The control sample is constructed from the COSMOS15 catalog [177] where the sources whose best-fit photo-z solution lies in the range $z_{\rm phot} = 3.4 - 4.2$ are selected. After removing galaxies with multiple peaks in the photo-z PDFs, the sample consists of 19,318 sources. We run the CIGALE software using the identical setup as previously, assuming constant SFHs for the both samples. While it is unrealistic to expect that all galaxies have constant SFHs, we are interested in the comparison of the two samples and not in exploring the full behavior of galaxies. A different SFH choice would generally shift measured quantities in the same direction for most galaxies, and thus would not change our conclusions. Finally, we note that the photo-z precision for the COSMOS galaxies is expected to be much better ($\sigma/(1+z) \sim 0.02 - 0.03$) than for our sample ($\sigma/(1+z) \sim 0.06$) thanks to the better imaging depth and finer wavelength sampling in the optical/near-IR wavelengths. While the larger uncertainty can introduce a larger scatter in the overall distribution of a derived quantity, it will not impact our ability to discern any mean relation between two different quantities.

In the left panel of Figure 2.11, we show the locations of our photo-z sources and of LAEs on the SFR-$M_{\rm star}$ plane together with those of the control sample. A prediction from a semi-analytic model [175] is also shown. Both our photo-z candidates and LAEs occupy the same region as the field galaxies, suggesting that they obey the same star formation 'main sequence' scaling relation, consistent with existing studies [40, 178, 179]. From the same figure, it is evident that the COSMOS datasets can probe galaxies down to much lower masses than the present dataset. The mismatch of the sensitivities of the two datasets renders it challenging to compare how the number counts in bins of SFR or stellar mass differ in the these samples.

To investigate possible environmental trends, we divide the photo-z sample into several environmental bins and color-code them accordingly where darker shades represent higher densities. Given the uncertainties in the extent and center of the structure, we define local environment using the LAE and photo-z surface densities. The results are shown in top middle and right panels. The overall correlation – measured for each subsample in mass bins of $\Delta \log M_{\rm star} = 0.25$ – is shown in solid lines. The SFR-$M_{\rm star}$ scaling laws measured from these subsamples are generally similar to that measured in the COSMOS sample.

We detect a hint of enhanced star formation activity in the highest photo-z overdensity subsample. Four galaxies deviate from the field average by 0.3-0.4 dex (a factor of 2–3). The overall scaling relation in this bin has a slightly higher normalization (i.e., $\sim$0.1 dex higher SFR in a given stellar mass bin) although the scatter is substantial. Interestingly, the same bin also lacks massive galaxies above $\log M_{\rm star} = 10.8$. The high-mass high-SFR end is well populated by galaxies residing in all environments. All in all, the environmental effects on star-forming galaxies appear to be minimal.

The lack of detectable environmental effects on the galaxy properties is puzzling. Uncertain cluster membership surely plays a role in diluting any existing trend by misplacing a subset of galaxies into a wrong density bin. However, should there be an excess of high-mass or high-SFR galaxies in dense environments, our analyses would have captured it as the regions most likely to be dense are counted as such in one or the other scenario. Hence, our analysis suggests that the environmental effect on star formation is likely a subtle one.

Alternatively, most of the enhanced star formation is perhaps obscured from our view by dust. Koyama et al. (2013) [30] reported that while sSFRs are higher for galaxies in cluster environment than those in the field, the trend emerges only when the mid-infrared budget of the SFR is properly accounted for. They argued that their result may be explained if a higher fraction of nucleated dusty starbursts exist in cluster environments where dust properties are significantly different from normal star-forming galaxies, such that applying the same dust correction as the field galaxies would underestimate the true SFRs.

The lack of extreme star-formers in our sample (in both field and protocluster) is also in part a selection effect. Extremely dusty starbursting galaxies would not be included in our sample, as they would not have a strong enough spectral break for us to identify them robustly, or perhaps, are entirely invisible in the optical or infrared wavelengths. We therefore cannot test for the prevalence of dusty starburst systems in dense environments reported by several studies [76, 77]. Testing these hypothesis will require deeper infrared and submillimeter coverage of the field.

2.6.4 Search for Extreme Sources in the Protocluster Field

The presence of powerful radio galaxies has been used as a signpost of highly overdense regions [65–69, 80, 145, 176, 180]. Likewise, highly overdense structures appear to harbor powerful AGN observed as X-ray or submillimeter luminous sources, or giant Lyα nebula [39, 73, 74, 76, 77, 181].

Motivated by these findings, we search the existing radio and X-ray source catalogs to look for a sign of enhanced AGN activity. We cross-match the *Chandra* X-ray point-source catalog of the Boötes field [182] with our photo-z, BBG, and LAE positions, and find no match. The XBoötes survey sensitivity of the full band (0.5–8 keV) is 7.8×10^{-15} ergs cm^{-2} s^{-1}. Lehmer et al. (2009) [74] studied X-ray detected sources in and around the SSA structure at $z = 3.09$, and found that the X-ray flux for the confirmed members range in $(0.3 - 5.0) \times 10^{-15}$ ergs cm^{-2} s^{-1}. Thus, non-detection merely suggests that even the brightest X-ray sources in SSA22 would lie below the XBoötes detection limit.

We also search for radio counterparts of our protocluster candidates (both photo-z and BBG candidates) in the radio source catalog based on deep Low Frequency Array (LOFAR) 150 MHz observations (Tasse et al. in prep). The rms noise of of the data is 59 μJy/beam. Using the matching radius of $2''$, no counterpart is found. We also compare our source positions against the photometric redshift catalog of the same LOFAR-detected sources constructed following the method presented in [183, 184], which covers roughly two thirds of our survey field and only half of the photo-z overdensity region. This is because the bottom one third of our survey field lies outside of the NDWFS field [90]. Once again, no credible counterpart is identified. In addition, we cross-match our candidates with deep Westerbork Synthesis Radio Telescope (WSRT) 1.4-GHz catalog covering Boötes field [185], and find no counterpart.

Therefore, we can rule out the presence of any high-redshift radio source with the flux density > 0.2 mJy in the probed redshift range.

Apart from the limited survey sensitivities, non-detection of powerful AGN in the protocluster member candidates is perhaps not surprising. As discussed previously, the majority of our photo-z candidates, by design, resemble LBGs with a clean spectral break. This requirement effectively removes all galaxies that are either dusty starbursts or AGN with power-law-like SEDs similar to those identified by [77] in the COSMOS field; robust identification of such galaxies will require improved sensitivities and wavelength baseline.

2.6.5 The plausibility of a very large structure

We assess how likely it is to find both structures or one very large structure in our survey volume. We utilize a catalog containing 2,731 simulated clusters identified from the Millennium I+II runs as described in [37]. The minimum cluster mass is $10^{14}h^{-1}M_{\odot}$ at $z = 0$. The comoving volume of the simulation is $(500/h)^3$ Mpc^3 or 0.364 Gpc^3. Our survey volume is estimated conservatively to be 2.13×10^6 Mpc^3 assuming a flat redshift distribution at $z = 3.4 - 4.2$ over a $28' \times 28'$ area, which is 0.6% of the Millennium volume.

We randomly pick a region matching our survey volume, and record the number of clusters therein and the position and the mass of each cluster. The procedure is repeated 500,000 times. The median (mean) number of clusters is found to be 16.0 (16.5) with a standard deviation of 5.2; i.e., our survey volume is large enough to contain multiple clusters.

If the LAE and photo-z overdensities are part of a single very large structure, its combined mass would be enormous. In Dey et al. (2016) [46], based on the level and extent of the LAE overdensity alone, we estimated that the enclosed mass is $> 10^{15}M_{\odot}$. As discussed in § 2.5.3, the photo-z overdensity should contain a comparable mass. Given that the two overdensities only partially overlap (and the regions of the peak overdensities do not overlap), a conservative limit on its combined mass is in the range of $(1.5-2.0)\times10^{15}M_{\odot}$. We find the probability of these scenarios to be 4.4% and 0.8%, respectively. In the entire Millennium volume, eight and one structures exist with masses above $1.5\times10^{15}M_{\odot}$ and $2\times10^{15}M_{\odot}$ respectively, corresponding to the comoving number density of $(2.2\pm0.8)\times10^{-8}$ Mpc^{-3} and $(2.7\pm2.7)\times10^{-9}$ Mpc^{-3}, respectively. The most massive structure in the Millennium simulations has a total mass of $2.4\times10^{15}M_{\odot}$. The observational counterpart of such an ultramassive cluster may be the El Gordo system, which is a merging pair of Coma-analogs at $z=0.87$ [186].

To test the possibility that the two overdensities are unrelated structures, we search for the cases in which there are two Coma-like clusters (i.e., each with mass $\geq10^{15}M_{\odot}$). This occurs only 3.6% of the time. Finally, we assess how unlikely it is that the photo-z overdensity lies at $z=3.72$ (see discussion in § 2.5), which would put the distance between the two at 47 Mpc or 10 proper Mpc. Only four distinct pairs of Coma analogs exist in the Millennium sample that are within 10 Mpc (physical) from each other. Two of those pairs have the physical separation of 5.2 Mpc and 5.3 Mpc from each other, and the other two at 9.3 Mpc and 9.8 Mpc. The separation for the latter is comparable to that between PC217.96+32.3 and the putative overdensity at $z=3.72$ [146]. The likelihood of such a configuration falling into our survey is 0.8%. These considerations show that both scenarios are extremely unlikely to occur by chance, but also that it is not impossible.

The overall density of the regions in and around PC217.96+32.3 is remarkably high. Apart from the two overdensities we discuss here, two other LAE overdensities lie within $\sim$ 10 Mpc (physical) north of of PC217.96+32.3 [45], one of which is spectroscopically confirmed and has the estimated descendant mass of $\approx6\times10^{14}M_{\odot}$ [46]. Given the distances between these system, it is unlikely they will coalesce into a single structure within the Hubble time, but rather, will evolve separately and form structures similar to local superclusters [187, 188].

2.7 Summary

Utilizing the multi-wavelength dataset taken in the sightline of PC217.96+32.3, a spectroscopically confirmed protocluster at $z = 3.78$, we have detected continuum-faint LAEs [45,46], UV-luminous star-forming galaxies, candidates of passive galaxies and of young post-starburst galaxies with a strong Balmer/4000Å break. Together, these constituent galaxies span 2–3 orders of magnitudes in both stellar masses and SFRs, highlighting diverse galaxy types residing in and around one of the largest structures discovered to date. Although we do not have spectroscopic redshifts for the new candidate protocluster members, the photometric redshift estimates suggest that they lie at or near the redshift of PC217.96+32.3. Based on our analyses, we conclude the following:

[1] A significant overdensity $\delta_g \approx 7.8 \pm 2.4$ of massive star-forming galaxies is present in the field. The extent of the newly identified photo-z overdensity only partially overlaps with that of the previously known and spectroscopically confirmed members, which are mostly LAEs; the two are offset by 3–4 Mpc in the east-west direction. While the origin of this separation is unclear, we speculate that the true extent of the structure may be larger than previously thought with a complex geometry only a part of which is traced by the LAE sample. This is presumably because the redshift of the main portion of the overdensity puts the Lyα emission just outside the bandpass of the narrow-band filter used for the LAE selection. If the combined overdensity traces a single structure, a conservative estimate would place its total mass in the range of $(1.5 - 2.0) \times 10^{15} M_{\odot}$, making it a singularly large cosmic structure rarely seen in cosmological simulations. However, we cannot rule out that the galaxy distributions are produced by a chance projection of two unassociated protoclusters at $z \sim 4$, each of which will evolve into a Coma-like cluster by $z = 0$. The likelihoods of both scenarios are extremely low ($< 1\%$).

[2] We find a large excess ($\delta\Sigma_{\rm BBG} \approx 9$–16) of ultramassive ($\sim 10^{11} M_{\odot}$) galaxies exhibiting a strong Balmer/4000Å break. Their SEDs are consistent with those of passively evolving galaxies and of young post-starburst galaxies entering into quiescence. The sky distribution of BBGs appears to trace the full extent of the large scale structure rather than being concentrated in the highest density environments. We speculate that BBGs may represent the central and most massive inhabitants of the dark matter halos that are in the process of merging. Quenching of massive cluster ellipticals occurred in the epoch when the high-density environment did not adversely impact star formation activities therein, and long before these galaxies become part of a single coalesced structure. If confirmed, the presence of massive and quiescent galaxies as early as $z \sim 3.8$ would push back the formation epoch of the cluster red sequence to beyond $z_f \approx 5$ in the largest clusters such as Coma.

[3] Stellar population parameters measured for all member candidates span several orders of magnitude in the dynamic range of stellar masses, SFRs, and specific SFRs, showcasing the diverse constituents inhabiting the underlying large scale structure. We find that the protocluster galaxies obey the same SFR-$M_{\rm star}$ scaling relation as the field galaxies. Our results suggest that the environmental effect on the stellar population properties of galaxy constituents is a subtle one at best. Alternatively, the impact of local environment manifests itself in producing extremely dust starburst systems, which would entirely elude our selection of galaxy candidates.

[4] While all galaxy types (LAEs, LBGs, and BBGs) show significant overdensities in the region, the BBGs show the largest overdensity. If they trace the same underlying structure, our results would be consistent with the theoretical expectation that more massive galaxies are more biased tracers of the underlying matter. These results highlight the usefulness of using low-mass galaxies such as LAEs as the least biased visible tracers in quantifying the large-scale structures around massive protoclusters such as the one we have studied. Sensitive LAE surveys are therefore an efficient

method to characterize large scale structure at high redshift, discover protoclusters, and as tracers of the physical processes responsible for cluster formation.

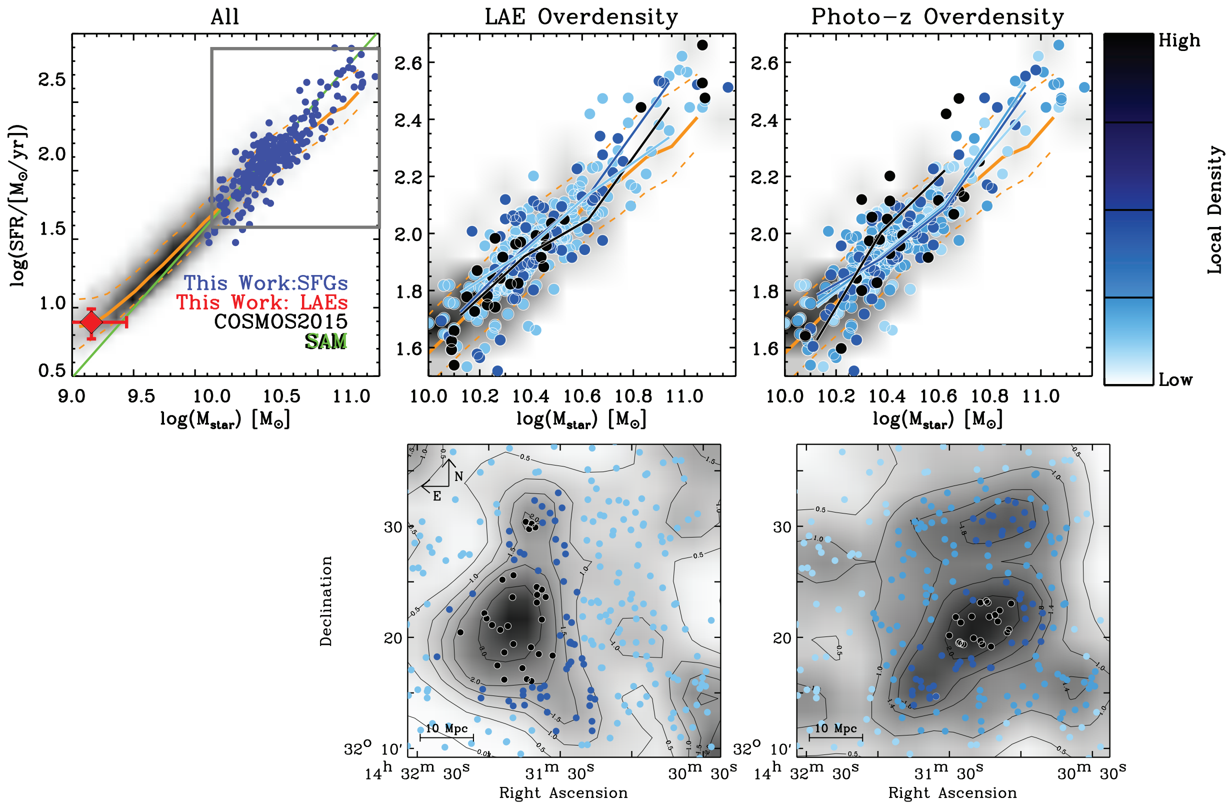

Fig. 2.11. *Top left:* the location of photo-z protocluster candidates (blue circles) and LAEs (red diamond) on the SFR-$M_{\rm star}$ space. The latter measurements are based on median image stacking. Grey scales show the distribution of COSMOS field galaxies at the same redshift range, and are color coded by the source density in each bin. The median scaling relation and the 16th/84th percentiles determined for the average field are shown in all top panels as solid and dashed orange lines, respectively. A prediction from a semi-analytic model by [175] is indicated by a green line. *Middle and right panels:* A zoom-in on the parameter space populated by our photo-z candidates. Each galaxy is color coded by its approximate local environment determined based on the surface density of the LAEs (top middle) and photo-z member candidates (top right) such that darker shades represent higher environmental densities. The sky distribution of the same galaxies are shown in bottom panels with the density maps (identical to those in Figure 2.8) overlaid. In both panels, the scaling relation is recomputed for each environmental density bin. The same scaling law is obeyed by all environmental bins although there is a hint that the galaxies residing in the highest photo-z overdensities appear to have higher SFRs than the rest.

3. HOW DO GALAXIES TRACE A LARGE SCALE STRUCTURE?: A CASE STUDY AROUND A MASSIVE PROTOCLUSTER AT $Z = 3.13$

In the previous chapter, we investigated in details the different galaxy constituents in the $z = 3.78$ protocluster. An intriguing result from our study is that there seems to be a spatial segregation between the LAE overdensity and photo-z overdensity. While the reason is still unclear, we begin to wonder: is this segregation between different galaxy populations a unique feature in this particular protocluster or it can also be found in other protoclusters? In this chapter, motivated by a LBG overdensity at $z = 3.13$ discovered by Toshikawa et al. (2016) [47] in the D1 field of the Canada-France-Hawaii-Telescope Legacy Survey (CFHTLS), we examine this issue in more details. We conduct a narrow-band survey to select LAEs, and compare with the distribution of LBGs to see how the underlying large scale structure is traced by different types of galaxies. In addition, for the $z = 3.78$ protocluster, we did not find obvious environmental impacts on the photo-z galaxies within the protocluster. In this chapter, we would also like to check if the environmental effect exists on the LAEs in the overdense environment.

This chapter has been submitted as Shi et al. (2019) in Astrophysical Journal.

3.1 Abstract

In the hierarchical theory of galaxy formation, a galaxy overdensity is a hallmark of a massive cosmic structure. However, it is less well understood how different types of galaxies populate the underlying large scale structure. Motivated by the discovery of a $z = 3.13$ protocluster, we examine how the same structure is populated by Lyα-emitting galaxies (LAEs). To this end, we have undertaken a deep narrow-band imaging survey using an O III filter, which samples Lyα emission at this redshift. Of the 93 LAE candidates identified within a $36' \times 36'$ (70×70 Mpc^2 comoving) field, 21 galaxies form a significant surface overdensity ($\delta_{\Sigma,\mathrm{LAE}} = 3.3 \pm 0.9$). Intriguingly, the Lyman break galaxy (LBG) overdensity is spatially segregated from the LAE overdensity. One possible interpretation is that they trace two separate structures of comparable masses ($\approx 10^{15} M_\odot$) where the latter is hosted by a halo assembled at an earlier time. We speculate that the dearth of Lyα-emitting members in the LBG overdensity region may signal the role of halo assembly bias in galaxy formation within clusters, which would suggest that different search techniques may be biased accordingly to the formation age of the host halo. We also find that the median Lyα- and UV luminosity is 30–70% higher for the protocluster LAEs relative to the field. This difference cannot be fully explained by the galaxy overdensity alone, and may require either a top-heavy mass function or a higher star formation efficiency for protocluster halos. While the existence of rare sources such as a luminous Lyα blob and an ultramassive ($\approx 2 \times 10^{11} M_\odot$) galaxy found near the galaxy overdensities paints a picture consistent with the expected early growth in cluster galaxy assembly, further investigation is needed to elucidate a clearer physical picture.

3.2 Introduction

In the hierarchical theory of structure formation, initial small density fluctuations give rise to the formation of first stars and galaxies. These structures subsequently grow larger and more massive via mergers and accretion [9]. In this context, galaxy clusters provide a unique laboratory to study how galaxy formation proceeded in the densest cosmic structures. In the local universe, cluster galaxies form a tight ‘red sequence’ [189, 190] and obey the ‘morphology-density’ relation [18, 19], showcasing the impact of dense environments on the star formation activities of the inhabitants.

In addition, existing studies strongly suggest that cluster galaxies experienced early growth at an accelerated pace followed by swift shutdown of their star formation, and have been evolving passively in the last ≈ 10 Gyr [20, 22–25, 30, 176].

The presence of massive quiescent galaxies in clusters out to $z \sim 1$ argues that the negative impact of dense environments must become less pervasive at earlier times, and that the star formation-density relation may even reverse [27–32, 163, 191] although it is still a matter of debate when this reversal occurs [192]. While the enhanced level of star formation activity in young forming clusters would certainly be consistent with the general expectations of cluster formation, direct evidence of this observational picture needs to come from distant galaxies residing in 'protoclusters' at $z > 2$, the epoch in which much of star formation activity and subsequent quenching are expected to have occurred.

Young protoclusters are far from virialized, and are distributed over large cosmic volumes with their angular sizes expected to span $10'$–$30'$ in the sky [37,85]. Moreover, the largest structures (those which will evolve into systems similar to Coma with their final masses exceeding $\sim 10^{15} M_{\odot}$) are extremely rare with a comoving space density of $\approx 2\times10^{-7}$ Mpc^{-3} [37]. Combined with their optical faintness, these characteristics make it observationally challenging to robustly identify protoclusters, and to conduct a complete census of their constituents for those confirmed.

Nevertheless, some protoclusters have been confirmed thanks to deep extensive spectroscopy of 'blank fields' [20, 33, 38–42, 149], which give us a glimpse of diverse galaxy types residing in protoclusters, such as luminous Lyα nebulae, dusty star-forming galaxies, and massive and quiescent galaxies. Studying these galaxies in details will ultimately lead us to a deeper understanding of how a brightest cluster galaxy (BCG) and cluster elliptical galaxies formed.

Another critical avenue in understanding cluster formation is a detailed characterization of their large-scale environments. Such information will pave the way to understand how galaxies' star formation activity is linked to their immediate local density. One efficient way to do so is to pre-select candidates of overdensity regions photometrically and follow them up with spectroscopy. Given the expected high star formation activity, a selection of star-forming galaxies (such as Lyman break galaxies, LBGs hereafter) can provide a reasonable candidate pool, albeit not a complete one [43, 45–47, 193], from which possible overdensity structures may reveal themselves as higher surface density regions [37]. Alternatively, a line-emitter selection utilizing a narrow-band sampling strong emission lines such as Lyα or Hα has emerged as a popular choice as it allows sampling of a small slice of cosmic volume, which is advantageous in defining environments with minimal contamination from fore- and background interlopers [23, 68, 79, 176, 180, 194–198].

Given that a galaxy overdensity is a hallmark of massive cosmic structures, any method that is able to detect them should, in principle, serve us equally well in identifying progenitors of massive clusters provided that their galaxy biases are well understood. Understanding how different galaxy populations trace the underlying large-scale structure – not only LBGs and Lyα emitters (LAEs) but also other types such as AGN and dusty star-forming galaxies that have been reported to reside in abundance in dense protocluster environments – can illuminate the early stages of cluster elliptical formation, and also help us fine-tune the search techniques in the future in the era of wide-area surveys such as Large Synoptic Survey Telescope and Hobby-Eberly Dark Energy Experiment.

In this paper, we present a follow-up study of a galaxy overdensity in the D1 field of the Canada-France-Hawaii-Telescope Legacy Survey (CFHTLS). The structure 'D1UD01' was discovered as a result of a systematic search of protoclusters conducted by Toshikawa et al. (2016) [47] where candidate structures were identified based on their prominent surface densities of LBGs at $z \sim 3-5$. Follow-up spectroscopy confirmed five galaxies at $z = 3.13$ located within 1 Mpc of one another, lending confidence to the possible existence of a highly overdense structure. At this redshift, Lyα emission is conveniently redshifted into a zero-redshift [O III] filter, providing us a unique opportunity to explore how line-emitting galaxies are populated in a massive structure identified and characterized in an independent method.

This paper is organized as follows. In § 2, we present the new narrow-band ($o3$) imaging of a subsection of the CFHTLS D1 field containing a confirmed protocluster at $z = 3.13$. Combining the new observations with the existing broad-band data, we identify a sample of LBGs and LAEs, and conduct a search for Lyα nebulae in the field (§ 3). In § 4, we measure their angular distributions and identify possible overdensity regions. In § 5, we discuss the masses of their descendants, examine a possible trend of star formation activity with local environment, and speculate the implications based on these results. A search for a proto-BCG is also presented. Finally, a summary of our results is given in § 6.

We use the WMAP7 cosmology $(\Omega, \Omega_\Lambda, \sigma_8, h) = (0.27, 0.73, 0.8, 0.7)$ from [92]. Distance scales are given in comoving units unless noted otherwise. All magnitudes are given in the AB system [93]. In the adopted cosmology, $1''$ corresponds to the angular scale of 7.84 kpc at $z = 3.13$.

3.3 Data and photometry

3.3.1 New observations

In September 2017, we obtain narrowband imaging of the protocluster candidate 'D1UD01' and the surrounding region in the D1 field, one of the four Canada-France-Hawaii-Telescope Legacy Survey deep fields. The pointing center is [α, δ]=[36.316°, −4.493°]. The data is taken with the Mosaic 3 Camera [95] on the Mayall 4m telescope of the Kitt Peak National Observatory (NOAO Program ID: 2017B-0087). The KPNO no. k1014 ($o3$ filter, hereafter) is used, with a central wavelength of 5024.9Å and a full-width-at-half-maximum (FWHM) of 55.6Å. The $o3$ filter samples redshifted Lyα line in the range $z = 3.132 \pm 0.023$, spanning a line-of-sight distance of 44 Mpc.

The individual exposure time of 1200 sec is used with small-offset dithers (`FILLGAP`) optimized to fill in CCD chip gaps. We discard the frames taken with seeing $> 1.3''$. We identify and remove a handful of frames which appear to have been taken when the guide star was temporarily lost, resulting in the sources to leave visible trails in the image. The total exposure time of the new imaging is 14.0 hr. The mosaic image has a native pixel scale of $0.25''$.

We calibrate the astrometry with the IRAF task `msccmatch` using the stars identified in the CFHTLS deep survey catalog [199], and re-project each image with a pixel scale of $0.186''$ using the tangent point of the CFHTLS images. The relative intensity scale is determined using the IRAF task `mscimatch`. The reprojected frames are then combined into a final image stack using a weighted average, with the average weight inversely proportional to the variance of the sky noise measured in the reprojected frames. We trim the images removing the area near the edges with less than 20% of the maximum exposure time, and mask areas near bright saturated stars. The final mosaic has an effective area of 0.32 deg^2 with a measured seeing of $1.2''$.

As most of our observations were taken in non-photometric conditions, we calibrate the photometric zeropoint using the CFHTLS broad-band catalogs. The central wavelength of the g band is 4750Å, reasonably close to that of the $o3$ filter at 5024.9Å. We define a sample of galaxies that have the g-band magnitude of 21–25 mag with the blue $g - r$ colors ($g - r \leq 0.2$), and determine the $o3$ band zeropoint such that the median $o3 - g$ color is zero. We further check our result by plotting the $g - r$ colors vs $o3 - g$ colors for all photometric sources. We confirm that the intercept in the $o3 - g$ colors is zero.

In conjunction with the new $o3$ data, we use the deep $ugriz$ images available from the CFHTLS Deep Survey [199]. The broad band images are trimmed to have the identical dimension to the $o3$-band data. The photometric depth (measured from the sky fluctuations by placing $2''$ diameter apertures in random image positions) and native image quality of these bands are summarized in Table 3.1; their filter transmission curves are illustrated in Figure 3.1.

Table 3.1.
Data Set

Band	Instrument	Limiting magnitude† (5σ,AB)	FWHM ($''$)
u	MegaCam/CFHT	27.50	0.8
g	MegaCam/CFHT	27.82	0.8
$o3$	Mosaic-3/Mayall	25.21	1.2
r	MegaCam/CFHT	27.61	0.8
i	MegaCam/CFHT	27.10	0.8
z	MegaCam/CFHT	26.30	0.8

† 5σ limiting magnitude measured in a 2$''$ diameter aperture.

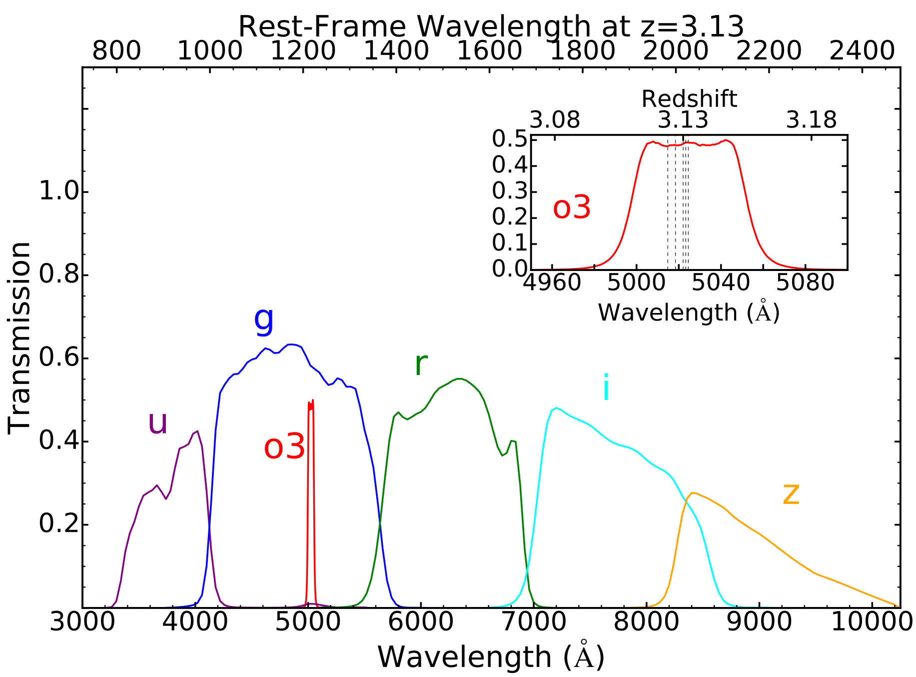

Fig. 3.1. Total throughput (filter+mirror+optics+CCD response) of the filters used to identify Lyα emitters in this work. The rest-frame wavelength range at z = 3.13 is shown on the top axis. The inset zooms in on the $o3$ filter region. The corresponding redshift range of Lyα emission is indicated on top. The spectroscopic redshifts of the five confirmed members are indicated by dotted vertical lines.

3.3.2 Photometry

We create a multiwavelength photometric catalog as follows. First, we homogenize the PSFs of the broad-band data to match that of the worst-seeing data, i.e., the $o3$ image (FWHM=1.2″). The radial profile of the PSF in each image is approximated as a Moffat profile with the measured seeing FWHM, and a noiseless convolution kernel is derived using the IDL routine `MAX_ENTROPY`. The broad band data is then convolved with their respective kernels to create a PSF-matched image.

We create the narrow band catalog by running the SExtractor software [200] in the dual image mode. The $o3$ band image is used for detection, while photometric measurements are performed in all the broad band images. The SExtractor parameter MAG_AUTO is used to estimate the total magnitude, while colors are computed from the fluxes within a fixed isophotal area (i.e., FLUX_ISO). As the images are PSF-matched, aperture correction in all bands is assumed to be given by the difference between MAG_AUTO and MAG_ISO estimated in the detection band. A total of 43,940 sources are detected in the $o3$ image. We also use the broad-band-only catalog released as part of the CFHTLS final data release[1] (referred to as a 'T0007' version, hereafter); the T0007 catalog contains 249,771 sources where a gri selected χ^2 is used as a detection image.

3.4 Analysis

3.4.1 Lyα-emitting Galaxies at $z \sim 3.13$

The primary goal of this paper is to investigate a possible presence of a large scale structure in and around the five spectroscopic sources at $z = 3.13$ discovered by Toshikawa et al. (2016) [47]. The $o3$ filter is ideally suited for this task as redshifted Lyα emission falls into it at $z = 3.13 \pm 0.02$. The redshift selection function, converted from the filter transmission, is illustrated in the inset of Figure 3.1. The Lyα-based

[1] `https://www.cfht.hawaii.edu/Science/CFHTLS/cfhtlsfinal releaseexecsummary.html`

spectroscopic redshifts of the five galaxies confirmed by [47] are marked as vertical dashed lines.

We adopt the following criteria to select LAE candidates at $z = 3.13$:

$$\begin{aligned} & o3 - g < -0.9 \quad \wedge \quad \mathrm{S/N}(o3) \geq 7 \\ & \wedge \quad [\; u - g > 1.2 \quad \vee \quad \mathrm{S/N}(u) < 2 \;] \end{aligned} \tag{3.1}$$

where the symbols $\vee$ and $\wedge$ are the logical "OR" and "AND" operators, respectively, and S/N denotes the signal-to-noise ratio within the isophotal area. The $u - g$ color criterion requires a strong continuum break falling between the two filters to ensure that the source lies at $z \geq 2.7$.

To design the selection criteria, we synthesize the colors by generating model galaxies spanning a range of rest-frame UV continuum slope, Lyα emission line equivalent width (EW), and Lyα luminosity. The galaxy's spectral energy distribution (SED) is constructed assuming a constant star formation history observed at the population age of 100 Myr, with an initial mass function from [111] and solar metallicity. We account for attenuation by intergalactic hydrogen using the HI opacity given by [201], and assume that the interstellar extinction obeys the reddening law of [110] .

To the reddened, redshifted galaxy SED, we add a Lyα emission with a Gaussian line profile centered at $1215.67(1+z)$Å and an intrinsic line width of 3Å. The redshift $z = 3.13$ is assumed. Given that the $o3$ filter is much wider than the line width, exact values assumed for the line width are not important as long as they reproduce the observed galaxy colors and line FWHM reasonably well. The Lyα limiting luminosity from the above criteria is $\approx 10^{42.3}$ erg s^{-1}. No extinction is applied to the Lyα line as it represents the observed luminosity.

In the left panel of Fig. 3.2, we show the expected $o3 - g$ and $g - r$ colors for different reddening values with different line luminosities. For the Lyα luminosities indicated in the same panel, we assume a continuum g band magnitude of 25.5 mag, which is based on the median value of our LAE sample. Finally, we stress that our photometric criteria (Equation 3.1) are sensitive to the line equivalent width and

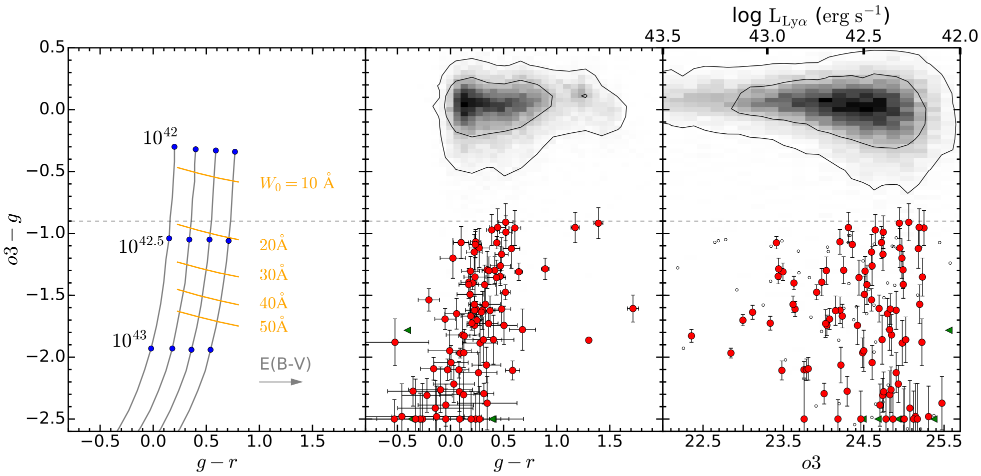

Fig. 3.2. *Left:* Theoretical tracks for LAEs of different luminosities and dust reddening in the $o3 - g$ vs $g - r$ color diagram. The grey lines show the color evolution with increasing Lyα luminosities (from top to bottom) at four reddening values (E$(B - V) = 0 - 0.3$ in steps of 0.1 from left to right). Blue points show the Lyα luminosities, $10^{42.0}$, $10^{42.5}$ and $10^{43.0}$ erg s^{-1} at the continuum g band magnitude of 25.5. Orange lines represent the Lyα rest-frame equivalent widths (W_0) of 10, 20, 30, 40, and 50Å. The $o3-g$ color cut (dashed horizontal line) approximately corresponds to $W_0 \geq 20$Å. *Middle:* the color-color diagram for all $o3$ detected sources. The two contour lines enclose 68% and 95% of the sources. Galaxies that satisfy the LAE criteria are indicated as red circles; those undetected in g or r band are shown as green triangles. Galaxies with $o3 - g \leq -2.5$ are shown at the color position of -2.5. *Right:* $o3 - g$ color as a function of $o3$-band magnitude. Sources that do not meet the $u - g$ color cut are shown in open circles. The approximate Lyα luminosities corresponding to the $o3$ magnitude are indicated on the upper abscissa.

redshifts of the source, but not to the choice of IMF and metallicity adopted to create the base galaxy SED. For example, if a sub-solar metallicity ($Z = 0.008$) is assumed, the $g - r$ colors would be bluer by 0.04 mag while the $o3 - g$ colors would remain unchanged.

The middle and right panel of Fig. 3.2 show the color-color and color-magnitude distributions of the $o3$-detected sources. The adopted selection criteria (Equation 3.1) correspond to the rest-frame equivalent widths ≥ 20Å at the target redshift range, and result in 94 LAE candidates. Their $g - r$ colors suggest that the majority are consistent with being relatively dust-free with a few exceptions. The LAE candidates are distributed over a $\approx 4,365$ Mpc^2 (1156 arcmin^2) field. With the exception of *six* (green triangles in Fig 3.2), all have robust continuum detections in the g or r band.

Based on the photometric data, we derive the physical properties of our LAE candidates including the rest-frame Lyα EW (W_0), Lyα luminosity ($L_{\mathrm{Ly}\alpha}$), UV continuum luminosity at the rest-frame 1700Å (L_{1700}), and UV spectral slope (β: defined as $f_\lambda \propto \lambda^\beta$). The Ly$\alpha$ luminosity and EW are derived following the prescription given in [102], which fully takes into account the Lyα forest attenuation in the relevant filters. The UV slope is computed from a linear regression fitting of the riz photometric data; the continuum luminosity L_{1700} is then extrapolated from the i-band flux density assuming the slope β. These quantities are listed in Table 3.2.

Four galaxies in our LAE sample are significantly redder ($g - r > 1.0$) than the majority. We check them in the image to verify these sources are real and robust detections. One is likely an AGN with an extremely high UV luminosity ($r = 21.7$ mag) and a point-like morphology. The other three may be more dust reddened than the other 90 LAE candidates. Dusty LAEs are rare, but have been reported in the literature [202, 203], some of which are IR-luminous galaxies detected in mid-infrared surveys. Assuming the dust law from [110] , their UV slope β values correspond to the color excess of the stellar continuum E($B - V$) of 0.20, 0.16, and 0.23, respectively, compared to the median value of 0.10 for the full LAE sample. These values are comparable to those measured for dusty LAEs with *Herschel*/PACS detection studied by [202].

Table 3.2.: Catalog of LAE candidates

ID	R.A. (J2000)	Decl. (J2000)	$\log(L_{\mathrm{Ly}\alpha})$ [erg s^{-1}]	$\log(L_{1700})$ [erg s^{-1} Hz^{-1}]	$W_{0,\mathrm{Ly}\alpha}$ [Å]	LBG	$o3-g$	$g-r$	$o3$	β
LAE11899	36.331703	-4.62293	42.27±0.14	28.20±0.09	20.1±8.3	1	-1.05±0.13	0.52±0.06	24.68±0.19	-1.8±0.2
LAE31361	36.147567	-4.34230	43.01±0.04	28.49±0.04	49.2±6.8	1	-1.65±0.06	0.29±0.04	23.11±0.07	-1.8 ± 0.4
LAE33092	36.133734	-4.31694	42.46±0.11	28.10±0.09	35.6±12.8	1	-1.40±0.14	0.43±0.09	24.40±0.19	-2.5 ± 0.7
LAE34191	36.112236	-4.30260	42.82±0.06	28.64±0.04	22.9±3.8	1	-1.12±0.05	0.44±0.03	23.37±0.08	-2.1 ± 0.5
QSO30046	36.461127	-4.36170	43.87±0.00	29.49±0.00	81.6±1.3	0	-1.96±0.01	1.30±0.01	21.06±0.01	-3.9 ± 0.5
LAB17139	36.082992	-4.54653	43.32±0.03	28.62±0.03	63.3±7.3	0	-1.81±0.05	0.13±0.05	22.37±0.06	-2.6 ± 0.8
LAE1223	36.548107	-4.78182	42.62±0.10	28.21±0.08	33.3±10.1	1	-1.38±0.11	0.17±0.07	23.99±0.16	-1.6 ± 0.1
LAE3003	36.544044	-4.75342	42.42±0.11	28.00±0.10	37.6±13.3	1	-1.48±0.15	0.18±0.12	24.52±0.18	-1.1 ± 0.2
LAE3007	36.347336	-4.75314	(42.03)	(27.09)	(123.3)	1	-1.65±0.19	<-0.41	25.69±0.75	(-1.7)
LAE3622	36.559838	-4.74334	42.18±0.15	27.74±0.13	44.3±22.4	1	-1.59±0.16	0.33±0.14	25.18±0.28	-1.2±0.1
LAE3833	36.399597	-4.74040	42.70±0.04	28.33±0.04	42.0±5.9	1	-1.54±0.06	0.52±0.05	23.85±0.07	-1.9±0.2
LAE4290	36.580112	-4.73362	(42.56)	(27.09)	(482.1)	0	<-4.30	–	24.49±0.11	(-1.7)
LAE4423	36.532995	-4.73160	(42.21)	(27.05)	(130.1)	1	-2.33±0.26	-0.46±0.59	25.29±0.19	(-1.7)
LAE4564	36.196192	-4.73027	42.53±0.05	27.60±0.10	95.3±21.4	0	-2.15±0.12	-0.35±0.24	24.42±0.09	-0.3±0.2
LAE4614	36.531916	-4.72931	42.38±0.10	28.15±0.09	29.6±9.7	1	-1.31±0.16	0.47±0.10	24.56±0.15	-1.3±0.5
LAE5378	36.626309	-4.71876	42.41±0.10	27.45±0.13	174.8±93.0	1	-2.51±0.21	0.24±0.24	24.78±0.22	-2.0±1.7
LAE7142	36.383586	-4.69378	42.41±0.12	28.05±0.10	35.5±13.6	1	-1.43±0.16	0.32±0.10	24.52±0.19	-1.4±0.2
LAE7560	36.517002	-4.68750	42.32±0.07	27.68±0.08	48.4±12.4	1	-1.61±0.12	0.06±0.11	24.83±0.13	-2.6±0.5
LAE8382	36.475010	-4.67657	42.77±0.04	28.35±0.04	34.4±5.0	1	-1.39±0.05	0.21±0.04	23.64±0.07	-1.9±0.1
LAE8783	36.262082	-4.67020	42.37±0.06	27.41±0.10	106.5±29.2	1	-2.21±0.14	-0.22±0.24	24.83±0.12	-1.1±0.4
LAE9355	36.224172	-4.66214	42.78±0.03	27.99±0.03	87.3±11.6	1	-2.07±0.07	0.08±0.09	23.79±0.06	-1.4±0.7
LAE9436	36.416560	-4.66001	42.11±0.13	27.28±0.17	52.5±25.1	1	-1.72±0.19	-0.52±0.32	25.38±0.25	-0.8±2.3
LAE9589	36.276072	-4.65831	42.60±0.06	27.95±0.06	48.2±10.4	1	-1.63±0.08	-0.05±0.10	24.14±0.11	-1.9±1.0
LAE9596	36.207723	-4.65882	42.79±0.04	28.27±0.02	47.1±6.4	1	-1.61±0.06	0.24±0.05	23.65±0.07	-2.0±0.2
LAE11088	36.513041	-4.63546	42.34±0.11	27.62±0.12	71.0±30.2	1	-1.89±0.18	0.28±0.17	24.97±0.22	-2.4±0.8

continued on next page

Table 3.2.: Catalog of LAE candidates

ID	R.A. (J2000)	Decl. (J2000)	$\log(L_{\mathrm{Ly}\alpha})$ [erg s^{-1}]	$\log(L_{1700})$ [erg s^{-1} Hz^{-1}]	$W_{0,\mathrm{Ly}\alpha}$ [Å]	LBG	$o3-g$	$g-r$	$o3$	β
LAE11215	36.449218	-4.63364	42.26±0.08	27.26±0.14	167.9±81.2	1	-2.50±0.23	0.09±0.34	25.15±0.18	-1.7±2.4
LAE11424	36.531781	-4.63014	42.29±0.16	28.18±0.10	18.8±8.3	1	-1.00±0.12	0.39±0.05	24.61±0.21	-2.0±0.4
LAE11535	36.066720	-4.62925	42.89±0.07	28.87±0.06	33.1±7.8	0	-1.42±0.09	0.89±0.04	23.34±0.12	0.5±0.5
LAE11926	36.472781	-4.62227	42.31±0.07	27.60±0.10	95.7±29.5	1	-2.17±0.15	0.03±0.19	24.97±0.14	1.5±0.3
LAE12763	36.481400	-4.60974	42.72±0.04	27.87±0.05	127.9±26.0	0	-2.31±0.08	0.31±0.09	23.99±0.09	-2.2±0.3
LAE12872	36.438421	-4.60755	42.46±0.09	27.99±0.08	30.6±9.9	1	-1.29±0.12	0.19±0.08	24.53±0.17	-2.5±0.1
LAE12900	36.049683	-4.60644	42.22±0.10	27.04±0.23	227.1±206.1	1	-2.80±0.29	-0.26±0.58	25.27±0.21	-0.1±3.6
LAE13337	36.189058	-4.60115	(42.33)	(27.21)	(150.2)	1	-2.43±0.21	-0.29±0.41	24.97±0.13	(-1.7)
LAE13519	36.344731	-4.59843	42.57±0.08	28.05±0.07	46.9±12.8	1	-1.62±0.11	0.23±0.09	24.21±0.14	-1.7±0.7
LAE13642	36.256098	-4.59568	(42.16)	(27.12)	(144.9)	1	-2.40±0.25	-0.13±0.42	25.38±0.16	(-1.7)
LAE13732	36.281673	-4.59482	42.29±0.10	28.53±0.07	23.3±7.0	0	-1.16±0.13	1.39±0.04	24.70±0.14	-1.2±0.5
LAE14869	36.431008	-4.57703	42.61±0.08	28.15±0.08	48.5±14.5	1	-1.72±0.12	0.37±0.09	24.05±0.16	-1.3±0.1
LAE16775	36.263772	-4.54861	42.19±0.15	27.96±0.11	22.7±10.7	1	-1.12±0.16	0.27±0.09	24.94±0.23	-1.8±0.1
LAE17045	36.598313	-4.54491	42.43±0.06	27.63±0.09	79.5±20.9	1	-1.99±0.14	0.00±0.16	24.65±0.12	-1.7±1.2
LAE17728	36.171767	-4.53675	42.80±0.06	28.26±0.05	45.2±9.3	1	-1.57±0.07	0.22±0.05	23.62±0.11	-2.4±0.1
LAE18151	36.253813	-4.52938	42.48±0.11	28.24±0.08	21.5±7.2	1	-1.07±0.10	0.24±0.05	24.20±0.16	-2.4±0.1
LAE18455	36.221296	-4.52418	42.14±0.08	27.23±0.12	150.2±68.3	0	-2.40±0.22	0.35±0.28	25.45±0.18	-2.9±2.2
LAE18514	36.153655	-4.52340	42.27±0.10	27.76±0.11	63.5±24.7	1	-1.87±0.18	0.31±0.17	25.00±0.19	0.2±0.1
LAE19027	36.069764	-4.51725	42.65±0.05	28.06±0.05	55.7±10.0	1	-1.74±0.08	0.23±0.07	24.04±0.09	-1.7±0.1
LAE19205	36.177991	-4.51562	42.85±0.06	28.64±0.05	33.6±6.0	1	-1.39±0.07	0.64±0.04	23.41±0.10	-1.4±0.4
LAE19465	36.190375	-4.51029	42.53±0.09	28.47±0.08	70.6±22.0	0	-1.92±0.11	1.72±0.05	24.38±0.17	-1.4±0.4
LAE19469	36.103684	-4.51081	42.86±0.05	28.56±0.04	34.1±5.8	1	-1.40±0.06	0.47±0.04	23.39±0.09	-1.7±0.4
LAE19503	36.103966	-4.50951	42.53±0.06	28.22±0.06	31.7±6.9	1	-1.34±0.11	0.42±0.06	24.21±0.10	-2.0±0.4
LAE19965	36.570704	-4.50256	42.31±0.16	28.13±0.11	26.0±12.5	1	-1.22±0.13	0.48±0.06	24.69±0.25	-1.5±0.1
LAE20057	36.184999	-4.50057	(42.32)	(27.09)	(427.9)	0	-2.98±0.33	<-0.37	25.05±0.18	(-1.7)

continued on next page

Table 3.2.: Catalog of LAE candidates

ID	R.A. (J2000)	Decl. (J2000)	$\log(L_{\rm Ly\alpha})$ [erg s^{-1}]	$\log(L_{1700})$ [erg s^{-1} Hz^{-1}]	$W_{0,\rm Ly\alpha}$ [Å]	LBG	$o3-g$	$g-r$	$o3$	β
LAE20136	36.169522	-4.49970	42.32±0.11	27.67±0.12	59.6±24.5	1	-1.79±0.16	0.11±0.16	24.87±0.22	-1.6±1.1
LAE20210	36.184859	-4.49883	42.34±0.07	27.59±0.10	96.0±31.9	1	-2.13±0.16	0.26±0.17	24.90±0.15	-1.6±1.0
LAE20309	36.272384	-4.49789	42.52±0.10	28.69±0.07	22.8±6.8	1	-1.15±0.12	1.17±0.04	24.11±0.14	-1.1±0.3
LAE20334	36.210326	-4.49665	42.30±0.12	27.76±0.11	49.3±21.0	1	-1.63±0.15	0.30±0.12	24.89±0.23	-2.3±0.3
LAE20391	36.574596	-4.49574	42.22±0.11	27.89±0.09	31.1±11.2	1	-1.32±0.15	0.35±0.09	24.97±0.18	-2.2±0.8
LAE21289	36.075996	-4.48283	42.40±0.06	27.51±0.10	114.1±37.1	1	-2.25±0.16	0.08±0.19	24.78±0.14	-1.7±0.1
LAE21315	36.078332	-4.48304	42.62±0.07	27.96±0.09	87.5±27.6	1	-2.09±0.14	0.34±0.14	24.19±0.15	-0.7±0.1
LAE21887	36.143396	-4.47564	42.94±0.05	28.29±0.05	102.8±20.7	1	-2.18±0.08	0.58±0.07	23.41±0.10	-1.5±1.2
LAE21996	36.137965	-4.47260	42.67±0.08	28.07±0.08	59.4±17.7	1	-1.75±0.11	0.36±0.09	24.00±0.16	-2.8±1.2
LAE22629	36.470213	-4.46346	42.34±0.09	27.93±0.08	49.0±15.7	1	-1.66±0.12	0.48±0.09	24.78±0.17	-1.3±0.8
LAE23293	36.058462	-4.45461	43.13±0.02	28.39±0.03	73.4±7.2	1	-1.94±0.04	0.09±0.04	22.88±0.05	-1.8±0.3
LAE23302	36.337272	-4.45334	42.25±0.08	27.21±0.16	132.0±60.0	0	-2.33±0.22	-0.14±0.35	25.15±0.18	-2.1±2.8
LAE23320	36.057467	-4.45327	42.37±0.09	27.52±0.13	117.0±52.2	1	-2.28±0.19	0.12±0.23	24.85±0.20	-0.9±0.1
LAE24442	36.133481	-4.43661	42.25±0.12	27.97±0.08	20.9±7.1	1	-1.04±0.13	0.10±0.07	24.75±0.15	-2.5±1.0
LAE25508	36.105297	-4.42287	42.52±0.11	28.05±0.10	59.1±23.3	1	-1.80±0.16	0.50±0.13	24.37±0.21	-1.1±0.4
LAE26131	36.476590	-4.41338	42.12±0.12	27.73±0.11	32.4±13.3	1	-1.35±0.15	0.23±0.10	25.23±0.21	-2.0±1.7
LAE26308	36.521510	-4.41145	42.31±0.13	27.24±0.19	223.7±170.5	1	-2.68±0.24	-0.04±0.41	25.06±0.30	-0.4±0.1
LAE26947	36.401936	-4.40294	42.36±0.08	27.69±0.08	38.9±10.7	1	-1.45±0.09	-0.20±0.10	24.69±0.15	-2.9±0.1
LAE28041	36.147012	-4.38820	42.61±0.10	28.29±0.08	31.2±9.6	1	-1.33±0.11	0.36±0.06	24.00±0.16	-1.9±0.5
LAE28534	36.261246	-4.38168	43.06±0.03	28.53±0.03	52.1±5.9	1	-1.70±0.05	0.25±0.04	22.99±0.06	-1.3±0.2
LAE28985	36.275809	-4.37465	42.48±0.06	27.72±0.08	76.2±20.2	1	-1.94±0.12	0.13±0.13	24.51±0.13	-2.5±1.0
LAE29112	36.574609	-4.37290	(42.50)	(27.09)	(417.3)	0	<-4.12	–	24.68±0.18	(-1.7)
LAE30621	36.335944	-4.35250	42.41±0.09	28.25±0.07	20.5±6.0	1	-1.09±0.10	0.23±0.06	24.36±0.14	-0.8±0.6
LAE31356	36.378076	-4.34067	42.46±0.08	27.72±0.11	68.3±22.5	1	-1.90±0.17	-0.01±0.20	24.55±0.15	-1.4±0.9
LAE31802	36.128128	-4.33464	(42.20)	(27.09)	(212.3)	1	<-3.45	–	25.34±0.17	(-1.7)

continued on next page

Table 3.2.: Catalog of LAE candidates

ID	R.A. (J2000)	Decl. (J2000)	$\log(L_{\mathrm{Ly}\alpha})$ [erg s^{-1}]	$\log(L_{1700})$ [erg s^{-1} Hz^{-1}]	$W_{0,\mathrm{Ly}\alpha}$ [Å]	LBG	$o3-g$	$g-r$	$o3$	β
LAE32293	36.376859	-4.32791	42.13±0.15	28.02±0.11	24.7±11.1	0	-1.19±0.16	0.57±0.08	25.11±0.22	-1.3±0.1
LAE33330	36.425224	-4.31357	42.41±0.10	27.71±0.12	75.3±30.5	1	-1.89±0.20	0.40±0.19	24.69±0.20	-3.6±1.6
LAE34533	36.392224	-4.29760	42.56±0.07	28.02±0.07	49.0±12.5	1	-1.66±0.10	0.19±0.09	24.24±0.14	-1.4±0.6
LAE35011	36.071438	-4.28969	42.33±0.13	28.07±0.10	23.6±9.5	1	-1.15±0.14	0.22±0.07	24.60±0.19	-1.8±0.1
LAE35344	36.578088	-4.28621	42.19±0.44	27.80±0.33	49.7±68.5	1	-1.03±0.14	0.61±0.06	25.17±0.82	-1.6±0.9
LAE35637	36.360586	-4.28129	42.07±0.14	27.99±0.09	18.3±7.5	1	-0.99±0.15	0.44±0.07	25.15±0.18	-1.8±0.5
LAE35739	36.566167	-4.27998	42.39±0.11	27.93±0.11	66.0±26.6	0	-1.87±0.17	0.68±0.12	24.73±0.21	-1.4±0.4
LAE35993	36.263103	-4.27687	42.59±0.06	27.32±0.16	194.9±71.6	1	-2.59±0.16	-0.53±0.40	24.34±0.13	-1.4±0.1
LAE36621	36.504879	-4.26776	42.12±0.16	28.11±0.10	17.5±8.0	1	-0.97±0.15	0.52±0.07	25.00±0.20	-1.7±0.3
LAE36658	36.557478	-4.26803	42.55±0.08	27.54±0.14	311.4±206.0	1	-2.86±0.23	0.19±0.36	24.47±0.19	0.3±1.9
LAE37505	36.255731	-4.25733	42.22±0.13	27.81±0.10	33.9±14.1	1	-1.40±0.11	0.17±0.09	25.00±0.23	-1.5±0.3
LAE37991	36.500602	-4.25212	42.76±0.04	27.89±0.06	87.3±14.6	1	-2.05±0.09	-0.03±0.14	23.84±0.07	-2.3±0.4
LAE38096	36.625888	-4.24970	42.41±0.07	27.48±0.12	125.8±47.7	1	-2.33±0.17	-0.04±0.26	24.76±0.16	-0.8±0.3
LAE38409	36.533597	-4.24540	42.34±0.06	27.29±0.15	320.2±206.4	1	-2.86±0.26	0.27±0.41	25.00±0.14	-0.9±0.8
LAE38991	36.598963	-4.23799	42.34±0.07	27.38±0.13	108.0±36.8	1	-2.19±0.18	-0.09±0.30	24.91±0.14	-2.2±2.4
LAE40397	36.449092	-4.21805	42.17±0.14	27.79±0.11	24.7±11.0	1	-1.15±0.16	0.02±0.12	25.02±0.22	-2.4±0.9
LAE40773	36.072466	-4.21316	42.73±0.06	27.90±0.07	79.1±18.4	1	-2.01±0.09	-0.16±0.12	23.89±0.12	-0.9±1.4
LAE41503	36.088564	-4.20889	42.93±0.04	28.35±0.04	53.5±7.1	1	-1.72±0.06	0.20±0.04	23.34±0.07	-1.5±0.4
LAE42838	36.164882	-4.20061	(42.80)	(27.31)	(944.1)	1	-3.23±0.32	-0.33±0.72	23.88±0.16	(-1.7)

Note: The spectroscopic redshifts are z=3.133, 3.124, 3.131, and 3.130 for LAE11899, LAE31361, LAE33092, and LAE34191, respectively. 'LBG' denotes whether this LAE also satisfies the LBG selection criteria; 1–yes, 0–no. In the cases where no significant continuum flux is detected, we use 2σ flux limit for calculating the colors. For sources where there are no β measurements (i.e., at least two broad bands are not detected), we use the median β value of the other sources, and give an estimate in parentheses. For sources not detected in g, a 3σ flux limit is used to estimate the continuum flux and equivalent width.

continued on next page

Three of the five spectroscopic sources in the 'D1UD01' structure satisfy our LAE selection; their IDs in the Toshikawa et al. (2016) [47] study are D1UD01-8, -9 and -6. Their Lyα EWs estimated from spectroscopy are 7.8, 21.0, 81.5Å, respectively. The remaining two, Toshikawa source ID D1UD01-7 and D1UD01-10, do not meet our LAE selection because they are too faint in the $o3$ band (S/N in the range of 4–5); however, their $o3 - g$ colors, -1.61 ± 0.10 and -1.33 ± 0.08, are consistent with the Lyα EWs, 36.2 and 34.3Å, measured from spectroscopy.

Sample Contamination At the central wavelength of the $o3$ filter (5024.9Å), the only plausible contaminants of our photometric LAE sample are [O II] emitters at $z \sim 0.35$, since our survey samples an inadequately small volume for [O III] emitters which would lie at $z \sim 0.01$. The adopted $o3-g$ color cut corresponds to the observed line EW of 83Å, much larger than the values measured for [O II] emitters, which mostly range in < 50Å [204, 205] at $z = 0.35$. The requirement that the galaxies have red $u-g$ colors provides an additional assurance that the Lyman break falls in the u band (i.e., the sources lie at $z > 2.7$).

Low-luminosity AGN with a broad Lyα emission line at $z > 2.7$ can potentially contaminate our LAE sample although the contamination is expected to be generally low (∼1%) [206–209]. We cross-correlate the source positions with the X-ray sources listed in the XMM survey in the field [210], and find no match. However, the brightest source in our sample (QSO30046, $o3$=21.06, r=21.69 mag) is detected in the *Spitzer* MIPS 24 μm data. QSO30046 is also observed by the VIMOS VLT Deep Survey (VVDS) [211] and classified as an AGN at $z_{\rm spec} = 3.86$. Given its redshift, the blue $o3-g$ color is owing to broad emission from Lyβ and O VI [212]. While we list its properties in Table 3.2, we remove this source from our LAE catalog.

We also cross-match our LAEs with spectroscopic redshift sources published by Toshikawa et al. (2016) [47] and those in the VVDS and VIMOS Ultra Deep Survey (VUDS) [213]. Four matches are found; three are part of the LBG overdensity reported by Toshikawa et al. (2016) [47] and the fourth lies at $z = 3.133$, but well outside it spatially. The relatively low number of matches is not surprising given that all these spectroscopic surveys are limited to sample only relatively bright sources (i.e., $i < 25$). In comparison, the mean i band magnitude of our LAE sample is ~ 26. Furthermore, the 'D1UD01' region is excluded from the UVUDS survey coverage.

3.4.2 Selection of LBG candidates

We also identify a sample of UV-luminous star-forming galaxies at $z \sim 3$ by applying the Lyman break color selection technique to the ugr data from the CFHTLS T0007 catalog. The technique can identify star-forming galaxies with a modest amount of dust by detecting spectral features produced by the Lyman limit at $\lambda_{\rm rest} = 912$Å and absorption by the intervening Lyα forest at $\lambda_{\rm rest} = 912 - 1216$Å. At $2.7 < z < 3.4$, both of these features fall between the u and g bands.

In the right panel of Fig.3.3, we show the expected redshift evolution of broad-band colors from $z = 2.7$ in steps of $\Delta z = 0.1$. Four reddening parameters are assumed, E$(B-V)$=0.0, 0.1, 0.2, and 0.3 (from left to right). The synthetic colors of lower-redshift galaxies are also computed using the Coleman et al. (1980) template [214] of S0 galaxies redshifted out to $z = 2$. As can be seen in the figure, most of the $z \sim 3.1$ sources are located at $u - g > 1.0$ while safely avoiding the locus of $z < 2$ galaxies. Based on these considerations, we adopt the following criteria which are identical to those used by Toshikawa et al. (2016) [47]:

$$\begin{aligned} u - g > 1.0 \quad \wedge \quad -1.0 < (g - r) < 1.2 \\ \wedge \;\; (u - g) > 1.5(g - r) + 0.75 \end{aligned} \tag{3.2}$$

In the left panel of Fig. 3.3, we show the locations of all the sources in the two-color diagram. For the sources undetected in the u band, we show lower limits by adopting the 2σ limiting magnitude (28.5 mag). We also require that the candidates be detected with more than 3σ (7σ) significance in the g (r) bands to ensure that their detection and color measurements are robust. A total of 6,913 galaxies are selected as our LBG candidates. 80 (86%) of the LAEs satisfy the adopted LBG criteria, with most of the remaining LAEs lying close to the selection criteria, confirming the similarity of the two populations. Our LBG catalog recovers 24 LBGs spectroscopically confirmed by Toshikawa et al. (2016) [47] including all five 'D1UD01' sources. Of 6,913 galaxies, 210 have spectroscopic redshifts measured from the VVDS and VUDS surveys and by Toshikawa et al. (2016) [47]. Of those, 27 lie at $z < 2.7$ yielding a contamination rate of 13%.

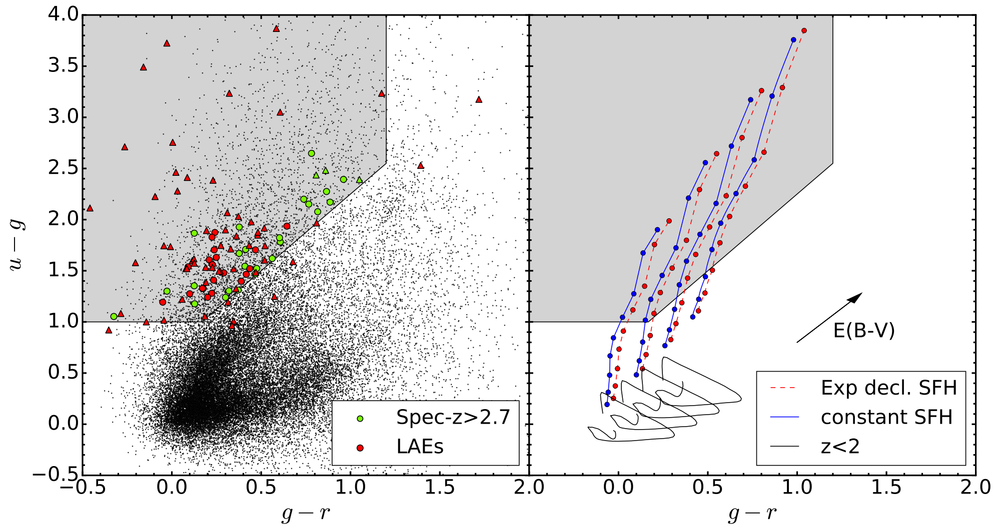

Fig. 3.3. *Left:* $u - g$ vs $g - r$ colors of all r-band detected sources are shown in dots together with the LBG selection indicated by a grey shaded region. Red symbols are photometric LAEs while green symbols are known spectroscopic sources at $z_{\rm spec} \geq 2.7$. All sources that are not detected in the u-band are shown as triangles using the 2σ limiting magnitude. *Right:* the redshift evolution of colors are illustrated for galaxies with dust reddening values. E$(B-V)$=0, 0.1, 0.2, 0.3 (from left to right). Galaxy's star formation rate is modeled to be constant (blue) or declining exponentially with time (red) as $\psi \propto \exp-(t/100\ \mathrm{Myr})$. Along a given track, source redshift increases from $z = 2.7$ upwards with the interval $\Delta z = 0.1$. Black lines show expected colors of local spiral galaxies when redshifted out to $z = 2$.

The majority of these 27 galaxies have redshifts close to $z = 2.7$, suggesting that they are simply scattered into the LBG window. To quantify the role of photometric scatter, we carry out realistic galaxy simulations similar to that described in [106]. First, we create SEDs spanning a wide range of physical parameters (age, reddening, and redshift) and compute input photometry of these SEDs in the observed passbands. Mock galaxies are inserted into the images, and detection and photometric measurements are performed using the identical manner as the real data. The galaxies which satisfy our LBG criteria are collated into the master list. The redshift distribution of LBG-selected mock galaxies in the magnitude range $r = 22 - 28$ (matching the optical brightness of our LBG sample) peaks at $z \sim 3.1$ with a FWHM of ~ 0.7. Of those, 12% lie at $z < 2.7$, nearly identical to the contamination rate of 13% estimated from spectroscopy.

We make a qualitative comparison of the T0007 catalog with the T16 catalog [47]. The major difference is a detection image which is a *gri*-based χ^2 image for the T0007 catalog and the i-band for the T16 catalog. The detection setting (including the threshold) is also different. Overall, we find that the T16 catalog is more inclusive of fainter objects with the median r-band magnitude of 26.5 mag, compared to 26.0 mag for the T0007 catalog. The two catalogs have 4,219 sources in common, which accounts for 61% and 54% of the T0007 and T16 catalogs, respectively.

3.4.3 Search of Lyα Blobs

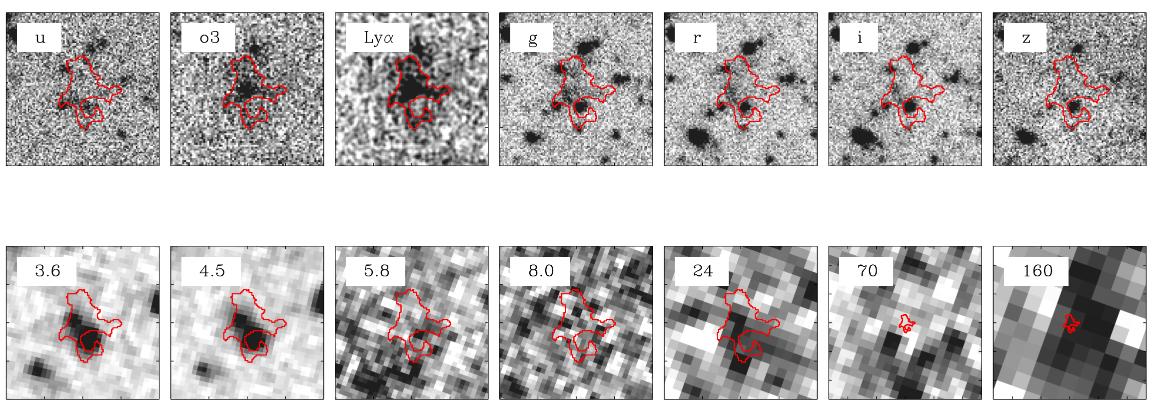

Fig. 3.4. Postage-stamp images of the LAB candidate LAB17139. In all panels, north is up and east is to the left. Each image is $20''$ on a side except for the 70 μm and 160 μm data which are $80''$ on a side. A red contour outlines the boundary of the Lyα isophote (see text).

We search for sources that are significantly extended in their Lyα emission; such sources are often referred to as a giant Lyα nebula or 'Lyα blob' (LAB, hereafter). The largest

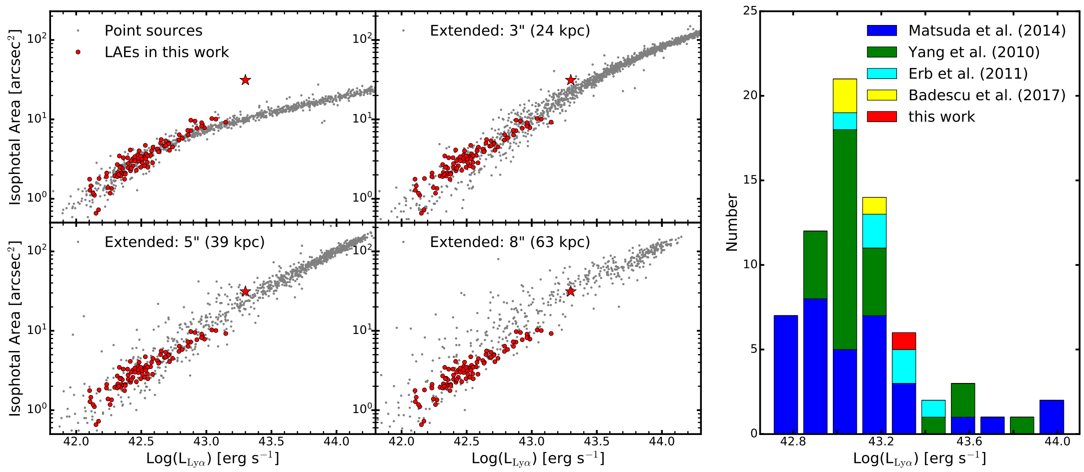

Fig. 3.5. *Left:* the relationship between Isophotal size and intrinsic Lyα luminosity are determined through image simulations assuming that the intrinsic light profile is point-like or falls off exponentially with a half-light radius of $3''$, $5''$, and $8''$. Grey points show simulated galaxies while red circles indicate the measurements from the LAEs in this study. The Lyα nebula, LAB17139, is marked as a red star in each panel. Given its observed luminosity and isophotal size, the half-light radius of LAB17139 is $\sim 40-55$ kpc (see text). *Right:* the distribution of Lyα luminosities of known giant Lyα nebulae in the literature. LAB17139 is once again marked in red.

LABs reported to date can be as large as > 100 kpc across [72]. Multiple discoveries of luminous LABs in and around galaxy overdensities [39, 71–73, 79, 196, 197, 215] have led to a claim that they may be a signpost for massive large-scale structures.

To enable a sensitive search, we first create a Lyα line image by estimating and subtracting out the continuum emission from the $o3$ image. Following the procedure described in [102], the line flux is expressed as $F_{\mathrm{Ly}\alpha} = af_{\mathrm{AB},o3} - bf_{\mathrm{AB},g}$, where f is the monochromatic flux density in the respective bands, and a and b are coefficients that depend on the corresponding bandwidth and optical depth of the intergalactic medium as well as the UV continuum slope. For example, at $z = 3.1$, with a UV slope β of -2.0, $a \sim 7.3 \times 10^{12}$ and $b \sim 7.7 \times 10^{12}$.

We run the SExtractor software on the Lyα image as a detection band and perform photometry on the $o3$ and g band data. For detection, we require a minimum area of 16 pixels above the threshold 1.5σ which corresponds to 27.81 mag arcsec^{-2} or 1.80×10^{-18} ergs s^{-1} cm^{-2} arcsec^{-2}. Our LAB search is slightly different from our LAE selection in that source detection is made on the Lyα image, and is tuned to be more sensitive to extended low surface-brightness sources. The same $o3 - g$ color cut (Equation 3.1) as our LAE selection is applied. Our search yields a single Lyα blob candidate in the entire field, which we name LAB17139. It is also identified as an LAE. At the Lyα luminosity of $\approx 10^{43.3}$ erg s^{-1}, it has the highest luminosity in our LAE sample. We estimate the isophotal area to be 31.2 arcsec^2. The postage-stamp images of LAB17139 are shown in Fig. 3.4, and its properties are listed in Table 3.2.

At the centroid of its Lyα emission, no apparent counterpart exists in any of the broad band data (gri). If its Lyα emission originates from a single galaxy, its continuum luminosity is fainter than r=28.6 mag (2σ). We do not find any plausible galaxy candidate in its vicinity that may lie at the same redshift. There are two UV bright sources just outside the isophote (one directly north and the other at the southwestern end); having the $u - g$ color of 0.57±0.19 and 0.90±0.12, neither of them satisfies our LBG selection. Therefore, it is unlikely they lie at the same redshift as LAB17139.

We search for its possible infrared counterpart utilizing two publicly available *Spitzer* observations in the D1 field, namely the *Spitzer* Wide-area InfraRed Extragalactic survey (SWIRE) [216], and the *Spitzer* Extragalactic Representative Volume Survey (SERVS) [217]. The former includes all IRAC and MIPS bands while the latter was taken as part of post-cryogenic IRAC observations (3.6 and 4.5μm bands only, which are deeper than the SWIRE counterpart). In Fig. 3.4, we show postage stamp images of these data centered on LAB17139.

A single IR-bright source is identified within the LAB isophote which lies $\approx$1.2$''$ away from the center of LAB17139; the source is securely detected in the 3.6 and 4.5μm bands and marginally detected in the MIPS 24μm, but not in the 70μm band. In the optical (gri) images, the source appears very diffuse and spans at least 2$''$. If it is a single source, it is likely an interloper as it is too large to lie at $z > 3$. Given its clear positional offset from the centroid of the LAB, it is unlikely that the source is solely responsible for the

Lyα emission. Thus, the physical association of this diffuse source and LAB17139 remains unclear. Further observations are needed to give a definite answer.

Intrinsic Size of LAB17139 We investigate the intrinsic size of LAB17139 by carrying out extensive image simulations. First, we insert artificial point sources with a range of luminosities into the Lyα image after convolving them with the image PSF, and recover them using the same detection setting as our LAB search. On the top left panel of Fig. 3.5, we show how measured isophotal size correlates with luminosity for point sources (grey symbols). It is evident that the majority of our LAEs follow the same sequence except for a few highest luminosity LAEs. On the other hand, LAB17139 lies well above the point-source locus: i.e., its high luminosity is insufficient to explain its large size.

Having established that the source is extended, we repeat the simulation but this time assuming that the radial profile of the source declines exponentially: $S(r) \propto \exp\left[-1.6783(r/r_s)\right]$. In Fig. 3.5, we show the luminosity-isophotal area scaling relation for the sources with half-light radii of $3''$ ($r_s = 1.8''$), $5''$ ($r_s = 3.0''$), and $8''$ ($r_s = 4.8''$); at $z = 3.13$, these values correspond to 24, 39, and 63 kpc, respectively. At a fixed line luminosity, the scatter in the recovered isophotal area increases with sizes as expected due to lower surface brightness. Nevertheless, Fig. 3.5 shows that a unique scaling relation exists at a fixed intrinsic size.

Utilizing this trend, with luminosities fixed in the simulation, we estimate that the half-light radius of LAB17139 must lie in the range of 39–55 kpc, provided that its surface brightness falls exponentially. Based on the average stack of 11 Lyα blobs at $z = 2.65$, Steidel et al. (2011) [218] reported the exponential scalelength of r_s=27.6 kpc, which corresponds to a half-light radius of 46.4 kpc. Thus, we conclude that LAB17139 has a similar size to $z \sim 2.6$ LABs.

In Fig. 3.5 (right), we also show the line luminosity distribution of known Lyα blobs in the literature [71, 79, 197, 219]. LAB17139 lies at a relatively high luminosity regime. The size distribution of LABs is more difficult to characterize because measured isophotal size of an LAB is determined by the combination of intrinsic source brightness, redshift, and imaging sensitivity. For example, given everything equal, the same source can have larger isophotal size as the imaging depth increases. In order to construct the intrinsic size distribution of Lyα nebulae, image simulations such as the one adopted here are needed to be run on each of the relevant dataset.

3.5 Sky Distribution of Galaxies

3.5.1 A significant overdensity of LAEs at $z = 3.13$

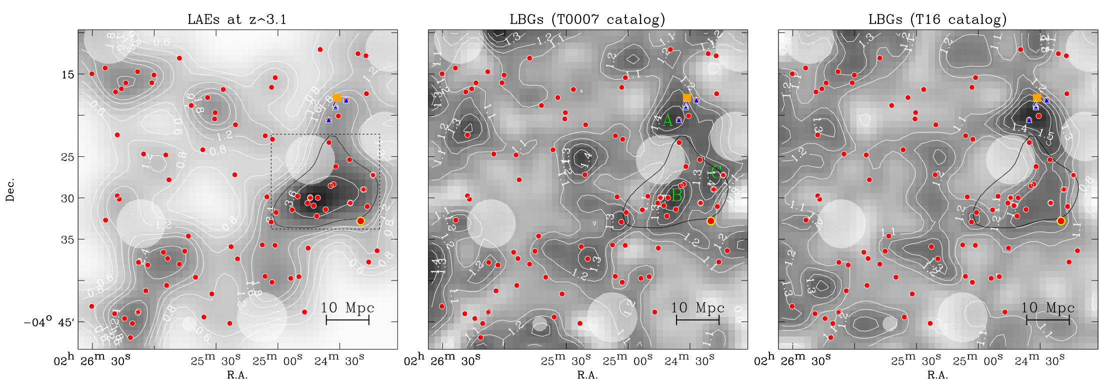

Fig. 3.6. *Left:* a smoothed density map of z=3.13 LAEs. Red circles show the LAE candidates while blue triangles indicate the five spectroscopically confirmed LBGs. The contours are constructed by smoothing the positions of the LAE candidates with a Gaussian kernel of FWHM=10 Mpc, and the contour labels show surface density levels relative to the field. The solid black line outlines the LAEs overdensity region. Pixels near bright saturated stars are masked out (hatched regions), and do not contribute to the overdensity estimate (see text). A large Lyα nebula (yellow open circle) and the brightest K_S band source (orange square) are also shown. *Middle and Right:* similarly constructed density maps using LBGs selected from the official CFHTLS catalog (middle) and the T16 catalog (right), respectively. For smoothing, a Gaussian kernel of FWHM=6 Mpc is used (see text for discussion). Three LBG overdensities are labelled as 'A', 'B', and 'C'. Positions of individual LBGs are not shown for clarity; other symbols are identical to those in the left panel.

The LAE distribution in the sky appears to be highly inhomogeneous, suggesting that there may be overdense structures. To quantify their spatial distribution, we start by estimating the mean LAE density. After removing the regions near saturated stars (hatched regions in Fig. 3.6), the effective area is 1,156 arcmin^2 over which 93 LAEs are distributed. Thus, we calculate the LAE surface density to be $\bar{\Sigma}$=0.08$\pm$0.01 arcmin^{-2} where the error reflects the Poisson noise.

To create a LAE density map, we place point sources in the masked regions whose numbers are commensurate with that expected at random locations to avoid producing artificial under-densities. On the positional map containing 93 LAEs and point sources, we apply a Gaussian kernel of a FWHM of 10 Mpc (5.1$'$: $\sigma = 4.25$ Mpc). A similar smoothing scale has been used to identify LAE overdensities in the literature [45, 79]. The resultant map is shown in the left panel of Fig. 3.6 as contour lines and grey shades. The contour line values represent the local surface density relative to the mean value. The positions of individual LAEs are also shown.

The highest LAE overdensity is located $\sim$5$'$ west of the field center. Twenty one galaxies are enclosed within the black contour (2.4$\bar{\Sigma}$ iso-density line), within which the effective area is 72.8 arcmin^2 (275 Mpc^2). We choose this region as the LAE overdensity. Scaling from the mean LAE surface density (0.08 arcmin^2), the expected number of galaxies within this region is 5.8 ± 2.4. Thus, the region contains 3.6 times more galaxies than expected ($\delta_\Sigma \equiv (\Sigma - \bar{\Sigma})/\bar{\Sigma} = 2.6 \pm 0.8$).

We recompute the mean density after excluding those in the LAE overdensity, and obtain $\bar{\Sigma}$=0.067 ± 0.008 arcmin^{-2}; this estimate is insensitive to inclusion or exclusion of the 'D1UD01' region which contains only a few LAEs. The revised overdensity is $\delta_\Sigma = 3.28 \pm 0.94$. Interestingly, LAB17139 is located at the outskirts of the LAE overdensity (see § 5.4 for more discussion).

We test the robustness of our overdensity estimate by computing the number of LAEs expected in our survey assuming the field Lyα luminosity functions at $z \sim 3.1$ [207, 220].

The expected number of LAEs in a magnitude bin $[m_k, m_k + \Delta m]$ and redshift bin $[z_j, z_j + \Delta z]$ is:

$$N_{\rm LAE}(z_j, m_k) = V_j p(m_k) S(z_j) \int_{L_k} \phi(L) dL, \tag{3.3}$$

where $S(z)$ is the normalized redshift selection function, defined from the effective filter transmission $T(\lambda)$ of the $o3$ filter expressed as $S(z_j) \equiv T(1215.67 \times (1 + z_j))/\max(T)$, V_j is the effective comoving volume, $p(m_k)$ is the completeness limit of the $o3$ image in the magnitude bin, which is derived from our image simulations of point sources. For our calculation, we use $\Delta z = 0.003$ and $\Delta m = 0.1$ mag. The total number of LAEs is thus calculated as $N_{\rm LAE} = \sum_j \sum_k N_{\rm LAE}(z_j, m_k)$.

The expected number of LAEs in our field is 71±8 using the best-fit parameters from [220] and 102±10 using the values from [207]. As for the errors, we assume Poisson statistics, which are underestimated as they do not include cosmic variance. The observed number of LAEs in our survey field is consistent with that expected in an average field. Using these values as the field LAE density, the overdensity outlined by the black contour in Fig. 3.6 is $\delta_\Sigma = 2.2 - 3.6$, consistent with our previous estimate.

The significance of the newly discovered LAE overdensity is comparable to those found in known structures in the literature. Kurk et al. (2000) [221] reported an LAE overdensity of $\delta_\Sigma = 3$ around a radio galaxy at $z = 2.16$ [68]. Another radio galaxy at $z = 4.1$ is associated with an LAE overdensity of $\delta_\Sigma = 3.7$ [68, 222]. The line-of-sight distances probed by these surveys are similar to this study ($\Delta z \approx 0.04 - 0.05$). Lee et al. (2014) [45] reported two structures with similar LAE overdensities, which were later confirmed spectroscopically as protoclusters [46].

3.5.2 LAE vs LBG distributions

If the LAE overdensity we discovered at $z \sim 3.13$ represents a genuine protocluster, the same region is expected to be traced by non-LAEs at the same redshift. Existing observations suggest that LAEs represent a subset of star-forming galaxies likely observed through sightlines with the lowest optical depths [223] and otherwise obey similar scaling relations as UV color-selected star-forming galaxies [45, 224]. However, some LAEs appear to have lower metallicities, higher ionization parameters [225–227], and less massive with younger ages [50–52] than non-LAEs.

Isolating non-LAEs at the same redshift is a formidable task. In principle, similar to the LAE selection, one can look for narrow-band 'deficit' sources to find galaxies with strong Lyα absorption [39]. However, the depth of our imaging data is inadequate for this method to be effective. Alternatively, one can use the surface density of LBGs as a proxy to search for high overdensity regions. Using the Millennium simulations, Chiang et al. (2013) [37]

demonstrated that the progenitors of the most massive galaxy clusters reside in regions of elevated densities even at the redshift smoothing scale of $\Delta z \leq 0.2 - 0.3$. Observationally, several confirmed protoclusters are discovered initially as LBG overdense regions [45, 47].

To investigate the possibility of LBG overdensities, we use two LBG samples, namely, our fiducial LBG sample selected from the T0007 catalog, and the T16 catalog constructed by Toshikawa et al. (2016) [47]. The number of LBGs in these catalogs are slightly different: 6,913 and 7,793, respectively, which mainly reflects the differences in their source detection setting as discussed in Section 3.4.2.

Similar to the LAE density map, we smooth the positions of each LBG using a Gaussian kernel. In determining the size of a smoothing kernel, two factors need to be taken into consideration: the source surface density and the volume within which a galaxy overdensity is enclosed. For instance, using a kernel size smaller than the typical distance between two nearest neighbors is undesired as most 'overdensities' will consist of a single galaxy. On the other hand, using too large a kernel size effectively averages out cosmic volumes that are much greater than a typical size of a galaxy overdensity, thereby washing away the very signal one is searching for.

In the case of LBGs, the source density is sufficiently high (and the distance to the nearest neighbor small) that the cosmic volume consideration becomes the main determinant of the kernel size. Toshikawa et al. (2016) [47] used a tophat filter with a diameter 1.5 Mpc (physical) in their search of $z \sim 3-6$ LBG overdensities. The size was justified as a typical angular size enclosing protoclusters in cosmological simulations [37]. At $z = 3.13$, this corresponds to 6.2 Mpc.

In the middle and right panels of Fig. 3.6, we show the resultant LBG maps using a smoothing FWHM of 6 Mpc. Grey scales and contour lines indicate the density fluctuations together with the positions of the LAEs (red circles), and five spectroscopic sources at $z = 3.13$ (blue triangles).

Several overdensities are present but each with a much lower significance than our LAE overdensity. This is not surprising considering the line of sight distances sampled by them. Our image simulation suggests that the FWHM in the redshift selection function, at $r \approx 24.5$, is $\Delta z = 0.7$ corresponding to 666 Mpc. Using the $o3$ filter FWHM, the LAE redshift range is z=3.109–3.155, spanning just 44 Mpc in the line-of-sight distance, more than an order of magnitude smaller than that of the LBGs. It is easy to understand that, even in a sightline of a massive protocluster, LBGs with no physical association with the structure will outnumber those in it.

In both LBG density maps (T0007 and T16 LBG samples), smaller overdensities as well as underdense regions spanning ≥ 20 Mpc are found in identical locations, and the largest and most significant overdensity structures are found at the western end of the field. In the T0007 map, the region consists of three adjacent overdensities labelled as 'A', 'B', and 'C' in Figure 3.6. In the T16 map, the overdensity A is noticeably more pronounced while the B and C overdensities, which are merged into a single overdensity, appear less significant.

The LAE overdensity largely coincides with the 'B+C' region, and stretches toward the 'A' region where a concentration of four LAEs lies. It is intriguing that in the 'A' region, which Toshikawa et al. (2016) [47] found to be the most significant LBG overdensity, relatively few LAEs are found. Assuming that all LAE candidates lie at $z = 3.13$, there are a total of just six galaxies in the 'A' region (including the spectroscopic sources that barely escape the LAE selection). In comparison, the LAE overdensity contains 21 LAEs. Extending the overdensity region slightly would include additional two LAEs and one Lyα nebula (Section 3.4.3).

Comparing the LAE and LBG maps, it is evident that their sky distributions are disparate. Other than the main LAE overdensity, none of the LAE density peaks coincides with the LBG overdensities. This likely suggests that there is only a single large-scale structure that exists at $z = 3.13$, and smaller LAE overdensities are a product of Poisson fluctuations, or alternatively, belong to much less significant cosmic structures than the one which the main LAE overdensity inhabits.

Next, we make a quantitative comparison of the LBG and LAE distributions in the general LAE overdensity region. To this end, we perform a series of two-dimensional Kolmogorov-Smirnov tests [143, 144]. We define a rectangular region enclosing the LAE overdensity as outlined in the left panel of Fig. 3.6 whose area is 115 arcmin^2. Running the 2D K-S test in the LBG and LAE distributions yields the p value of 0.28 (0.20) using the fiducial (T16) LBG samples. The large p value indicates the similarity of the two distributions.

As the 2D K-S test is less reliable than the one-dimensional test, we perform a control test to interpret the p values. First, we create two random samples that are uniformly distributed in the rectangular region, each matching the number of LAEs and LBGs in our samples, and calculate the corresponding p value. The process is repeated 1,000 times and the p value is recorded each time. We obtain a median (mean) p value of 0.23 (0.27). Second, we assume that the underlying distribution is a two-dimensional Gaussian function with σ=5′ centered at the middle of the rectangle, and repeat the test, obtaining similarly large p values (median and mean value of 0.27 and 0.31).

Finally, we test the similarity of the two galaxy samples in the entire field by moving the rectangle to random locations. Whenever a masked region falls within the subfield, we randomly populate the area with the expected number of point sources therein before performing the test. The median (mean) p-value is 4.5×10^{-15} (9×10^{-4}). These tests give strong support to the possibility that the cosmic structure traced by the LAE overdensity is also well populated by LBGs at a level not observed in other parts of the survey field.

All in all, our analyses strongly suggest a presence of a significantly overdense cosmic structure, which includes 21 LAEs, 5 spectroscopically confirmed $z = 3.13$ LBGs, and one luminous Lyα nebula. A large number of LBGs exist in the general region although, without spectroscopy, it is difficult to know how many of them truly belong to the structure. A segregation of the highest LAE and LBG overdensity is also curious. We discuss possible implications of our results in Section 3.6.4.

3.6 Discussion

3.6.1 Descendant mass of the protocluster

The present-day mass of the LAE overdensity

Given that the $o3$ filter samples ≈44 Mpc in the line-of-sight direction, a surface overdensity computed based on the angular distribution of galaxies should scale closely with a given intrinsic galaxy overdensity with a minimal contamination from fore- and background interlopers. In this section, we estimate the true galaxy overdensities, and infer their descendant (present-day) masses.

Based on the Millennium Runs, Chiang et al. (2013) [37] calibrated the relationship between galaxy overdensity (δ_g) and present-day mass $M_{z=0}$ at a given redshift. Galaxy overdensity is measured in a (15 Mpc)^3 volume ($\delta_{g,15}$ hereafter) using the galaxies whose host halos have the bias value of $b \approx 2$. This value is comparable to that typically measured for LAEs [45, 50, 168], which lie at similar redshift and are of comparable line luminosities to those in our sample. Thus, it is safe for us to apply the Chiang et al. calibration without further corrections.

The transverse area enclosing the LAE overdensity is 275 Mpc^2, reasonably close to that of (15 Mpc)^2 used by [37]. However, the line-of-sight distance sampled by the $o3$ filter is ~3 times larger than their sampled volume. Generally, averaging over a larger volume reduces the magnitude of the overdensity. We correct this effect using their Figure 13 where they show how, for a fixed $\delta_{g,15}$, measured (surface) overdensity drops with increasing redshift uncertainty Δz. Correcting the measured overdensity (§ 3.5.1) accordingly results in $\delta_{g,15} = 5.5 \pm 1.6$. Inferred from Figure 10 of [37], the corresponding descendant mass at $z = 0$ is $M_{\rm tot} \approx (0.6 - 1.3) \times 10^{15} M_\odot$. The estimated overdensity well exceeds the value $\delta_{g,15} = 3.14$, above which there is >80% confidence that it will evolve into a galaxy cluster by $z = 0$. These considerations lend confidence that the newly identified LAE overdensity is a genuine massive protocluster.

Alternatively, a more empirical method may be employed similar to that taken by [38]. If all mass enclosed within the overdensity will be gravitationally bound and virialized by $z = 0$, the total mass can be expressed as:

$$M_{z=0} = (1 + \delta_m)\langle\rho\rangle V_{\rm true} \tag{3.4}$$

where $\langle\rho\rangle$ is the mean density of the universe, and $V_{\rm true}$ is the true volume of the overdensity. The matter overdensity δ_m is related to the galaxy overdensity through the bias parameter as $1+b\delta_m = C(1+\delta_g)$ where C represents the correction factor for the effect of redshift-space distortion. The true volume $V_{\rm true}$ is underestimated by the same factor as $V_{\rm true} = V_{\rm obs}/C$. In the simplest case of spherical collapse, it is expressed as:

$$C(\delta_m, z) = 1 + \Omega_m^{4/7}(z)[1 - (1 + \delta_m)^{1/3}]. \tag{3.5}$$

Equation 3.5 and the equation relating the matter and galaxy overdensity can be evaluated iteratively to determine C and δ_m. The observed overdensity is $\delta_g = 3.3 \pm 0.9$ and the estimated survey volume of $V_{\rm obs} = 1.21 \times 10^4$ Mpc^3. The bias value is assumed to be $b \approx 2$ [45,50,168]. We obtain the matter overdensity in the range of $\delta_m = 0.8 - 1.3$; thus the total mass enclosed in this overdensity is $M_{z=0} \approx (1.0 - 1.5) \times 10^{15}\ M_\odot$, in good agreement with the simulation-based estimate. We conclude the LAE overdensity will evolve into a Coma-like cluster by the present-day epoch.

The structure and descendant mass of the LBG overdensity

As discussed in Section 3.5.2, there appear to be multiple LBG overdensities; these regions are marked as 'A', 'B', and 'C' in Figure 3.6. The 'B' and 'C' overdensities are merged into one in the T16 catalog, and lie in a region largely overlapping with the LAE overdensity, hinting at their physical association. On the other hand, the 'A' overdensity – ≈ 15 Mpc away from the LAE overdensity – may be a separate system and is largely devoid of LAEs therein. As such, we consider the 'B+C' and 'A' as two separate structures and evaluate their significance.

The LBG color criteria (§ 3.4.2) typically result in a relatively wide redshift selection, $\Delta z = 0.4 - 0.6$. The redshift range of spectroscopic sources yields the median redshift of $z = 3.2$ with the standard deviation 0.6, in a reasonable agreement with the FWHM Δz estimated from our photometric simulations (Section 3.5.2). This very wide Δz makes it challenging to directly use the Chiang et al. (2013) [37] calibration. Instead, we use an alternative method described in [224] to estimate the intrinsic galaxy overdensity as follows.

We create a mock field, which is of the same size as our survey field and contains a single protocluster with a galaxy overdensity δ_g. The protocluster overdensity is assumed to extend a transverse size of the LBG overdensity ('A') and 15 Mpc in the line-of-sight distance. We divide the redshift range $z = [2.7, 3.4]$ into 35 bins each with $\Delta z = 0.02$ ($\sim$19 Mpc). The number of galaxies belonging to the protocluster is then expressed as $N_{\rm proto} = (1 + \delta_g)N_{\rm all}/(35 + \delta_g)$ where $N_{\rm all}$ is the total number of LBGs in the field. We populate the remainder $(N_{\rm all} - N_{\rm proto})$ at random in the redshift and angular space. As for the protocluster galaxies, they are also randomly distributed but are confined within the overdensity region. Based on the galaxy positions, we construct the surface density map in the identical manner to the real data, and estimate the mean overdensity within the protocluster region. We repeat the procedure 10,000 times while varying the intrinsic overdensity δ_g in the range of 1–30, and obtain a relationship between the observed surface density and the intrinsic overdensity.

For the level of observed overdensity for the 'A' and 'B+C' regions, we choose the $1.3\bar{\Sigma}$ iso-density contour based on our fiducial LBG catalog; the transverse area of these regions are 36 and 27 arcmin^2, respectively; the 'B' and 'C' contours are disjoint and we simply add the enclosed regions. Using our simulation as described above, the intrinsic overdensities of the 'A' and 'B+C' regions are δ_g of $(18.4-28.4)$ and $(14.4-23.0)$, respectively. We assume that their galaxy bias is $b_{\rm LBG} \approx 2.6$, i.e., slightly higher than that of the LAEs [40, 228]. Using Equation 3.4 again, we obtain the total masses of these structures $(0.6-1.0)\times10^{15}M_\odot$ and $(0.4-0.6)\times10^{15}M_\odot$, respectively. Increasing the bias value to $b_g = 3$ would decrease the mass by 13%; decreasing it to a value similar to the LAE bias would have the opposite effect on the mass. Generally, our mass estimate is relatively insensitive to a specific choice of isodensity value. This is because lowering the density contrast tends to increase the effective area at a lower overall density enhancement, while raising it has the opposite effect.

We repeat our mass estimates using the T16 catalog which yields slightly different levels and angular extent of the overdensities. The resultant masses for the two structures are $(0.8-1.1)\times10^{15}M_\odot$ and $(0.4-0.6)\times10^{15}M_\odot$. The 'A' structure has $\approx 20\%$ larger mass, reflecting its more pronounced density contrast in the T16 catalog; the estimate for the 'B+C' region is consistent with the earlier estimate.

3.6.2 The physical properties of LAEs and their environmental dependence

We investigate whether local environment influences the properties of the LAEs. To this end, we define two LAE subsamples according to their measured galaxy surface density. The 'overdensity' sample includes 21 LAEs within the black contour shown in Fig. 3.6 as well as three of the Toshikawa et al. (2016) [47] galaxies that we recover as LAEs. The remaining 69 LAEs belong to the 'field' sample.

Apart from the line luminosities and EWs (§ 3.3.2), we also convert the measured UV continuum slope, β, to the extinction parameter E$(B-V)$ assuming the dust reddening law of local starburst galaxies [110]. For the sources with relatively robust β measurements

($\Delta\beta < 0.9$), we also derive dust-corrected SFRs by correcting the continuum luminosity accordingly using the Kennicutt et al. (1998) [229] calibration. In the overdensity and field sample, 21 (88%) and 42 (61%) LAEs have the SFR estimates. The difference stems from the fact that the former sample is on average more UV-luminous (see later). However, our SFR estimates are only approximate given a relatively large uncertainty in the measured UV slopes; increasing (decreasing) β value by $\Delta\beta = 0.4$ (which is well within a typical uncertainty) would lead to a 41% increase (58% decrease) in the SFR estimate.

The mean properties of each subsample are listed in Table 3.3 with the errors corresponding to the standard deviation of the mean, and the overall distributions of these parameters are illustrated in Fig. 3.7. In both, we show our results for the full sample containing 93 LAEs (top), and for the 63 LAEs with reliable SFR estimates (bottom). We find that our conclusions do not change depending on which sample we consider.

In terms of both line and continuum luminosities, we find a possible enhancement for the LAEs in the overdensity regions compared to those in the field. The enhancement in UV luminosity is 74±32% if we compare all LAEs in both samples, and 58±22% if only the LAEs with robust β measurements are considered. As for Lyα line luminosity, the enhancement relative to the field is 32±15% and 55±18% for all LAEs and those with β measurements, respectively. The median EW and E$(B-V)$ values are comparable in both samples.

To assess the similarity of the overall distribution of the physical quantities between the two samples, we perform the one-dimensional K-S test. The p values obtained for each distribution are indicated in Fig. 3.7. The values obtained for the Lyα and UV luminosity distributions lie around $p \sim 0.05$ corresponding to a 2σ in the confidence level. As for the EWs and UV slopes β, the distributions are statistically indistinguishable for the two environmental bins. All in all, our results suggest that the level of star formation activity, as probed by two indicators at rest-frame UV wavelength, may be enhanced in the LAEs residing in high-density environment compared to those in the average field.

The same trend is visualized in Fig. 3.8. In the left panel, we show the LAE positions overlaid with a two-dimensional Voronoi tessellated map of the whole field [230, 231]. Each LAE is embedded in a Voronoi polygon with an area A_V, and its 2D density scales inversely with the radius of the equivalent circular region defined as $r_V \equiv \sqrt{A_V/\pi}$. The map is

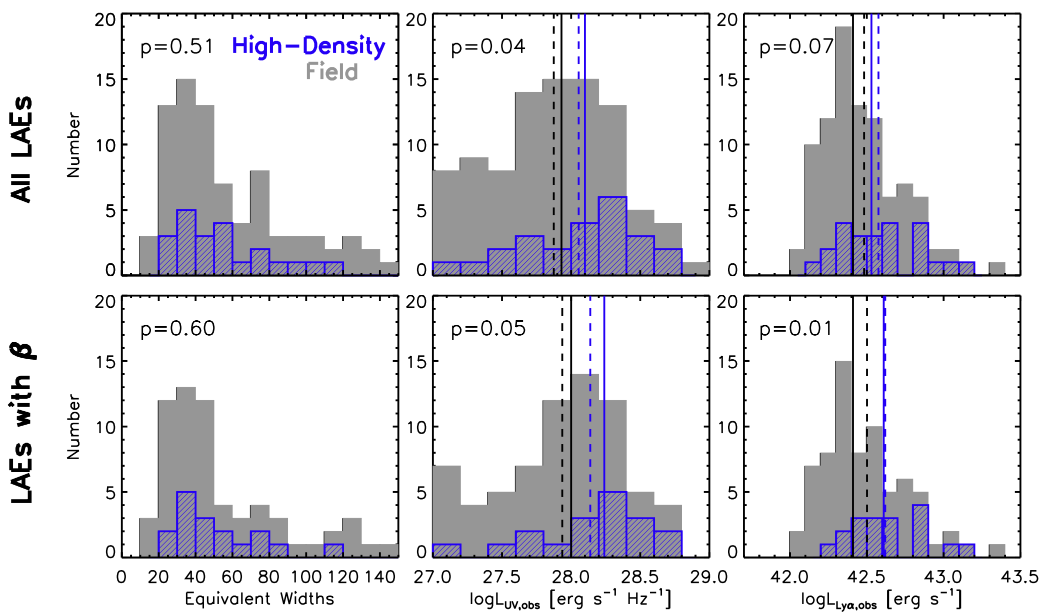

Fig. 3.7. Histograms of rest-frame equivalent widths (left), observed UV luminosity (middle), and observed Lyα luminosity (right) of two subsamples. Blue hatched and grey histograms represent high-density LAEs and field LAEs, respectively. The median p values obtained from the Kolmogorov-Smirnov test are shown in each panel. The vertical solid lines are the mean values while the dashed lines are the median values.

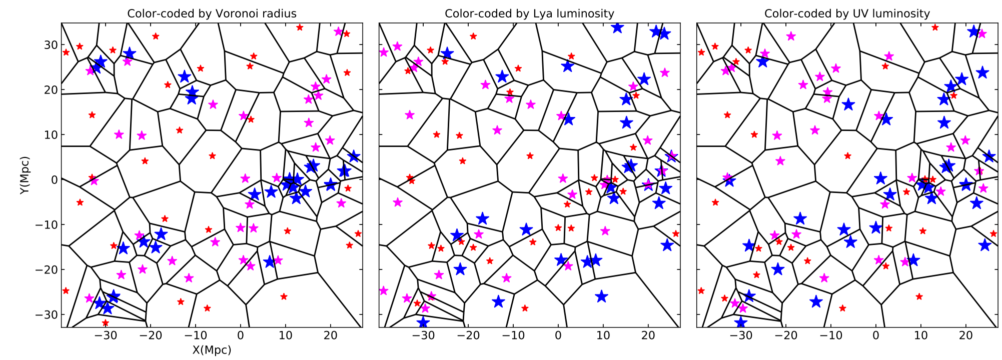

Fig. 3.8. Voronoi tessellated maps of the LAE positions. The LAE sample is divided by Voronoi radius (left), Lyα luminosity (middle), and UV luminosity (right) of each LAE. In all panels, blue, pink and red colors are used for the top, middle, and bottom third, corresponding to $r_V \leq 3.2$, $3.2 < r_V \leq 4.85$, and $r_V > 4.85$ in Voronoi radius, $\log(L_{\mathrm{Ly}\alpha}) > 42.60$, $42.38 < \log(L_{\mathrm{Ly}\alpha}) \leq 42.60$, and $\log(L_{\mathrm{Ly}\alpha}) \leq 42.38$ in line luminosity, and $\log(L_{\mathrm{UV}}) > 28.06$, $27.68 < \log(L_{\mathrm{UV}}) \leq 28.06$, and $\log(L_{\mathrm{UV}}) \leq 27.68$ in UV luminosity. The correlation between these parameters is evident as a large fraction of UV-/Lyα-luminous galaxies are found in the LAE overdensity region.

color-coded by the 2D density, with the size of each star increases with increasing density. The LAE overdensity stands out as a region with the highest concentration of blue stars.

In the other two panels of Fig. 3.8, we show the same tessellated LAE map but the LAEs are color-coded by Lyα (middle) and UV luminosity (right), respectively. A large fraction of blue stars representing a top third populate the combined region of the LBG and LAE overdensities. The trend is particularly evident for the case of continuum luminosity (right panel). Of the total 30 blue stars, 17 (57%) reside within the LAE overdensity region. No radial dependence is found for the luminosity enhancement within the group although our sample may be too small to discern any trend.

The higher UV- and Lyα mean luminosities observed for protocluster LAEs is curious and cannot be fully explained by the level of overdensity. If the protocluster LAEs obey the same UV or Lyα luminosity function as measured in the field but are simply scaled up by a factor of $(1 + \delta_g)$, the expected mean or median values would be identical to those in the field. Thus, our results tentatively suggest a mild widespread enhancement of star formation in the protocluster LAEs.

One possible explanation for the higher luminosity value may be that the luminosity function (and SFR function) is more 'top-heavy' in protocluster environment, producing a larger fraction of UV-luminous galaxies. This may be brought on by faster-growing halos as suggested by [36], or by a different star formation efficiency in clusters whereby a galaxy is more luminous at a fixed halo mass (Y.-K. Chiang, in private communication). Alternatively, it is also possible that protocluster LAEs simply have different ages and/or metallicity than elsewhere; however, the overall similarities in observed colors and EWs in the two environmental bins studied here argues agains this possibility.

Our result is seemingly at odds with some of the existing studies which found that galaxies in dense environment largely grow at a similar rate as those in average fields [34, 224], perhaps with an exception at the massive end [33]. However, it is worth noting that these studies focused on more UV-luminous, LBG-like galaxies that are, on average, a factor of $> 5 - 10$ more massive than the LAE population studied in this work. To discern a clearer trend and to study how it depends on galaxy's luminosity and stellar mass, and on galaxy types (LBGs, LAEs, etc.), a more comprehensive study is needed.

It is interesting to speculate a potential implication of our result in the cosmological context. By following the structures identified as cluster-sized dark matter halos at $z = 0$ in the Millennium simulations, Chiang et al. (2017) [36] estimated that the fractional contribution to the total star formation rate density (SFRD) from galaxies that will end up in clusters increases dramatically with redshift, from only a few percent at $z = 0.5 - 1.0$, to ≈20–30% at $z = 2 - 4$, and to nearly 50% at $z > 8$. This change is mainly driven by large cosmic volumes occupied by protoclusters well before their final coalescence (see their Figure 1) as well as high galaxy overdensities and the top-heavy halo mass function therein [36].

If the observed higher luminosity of protocluster LAEs has an astrophysical origin (e.g., a higher efficiency in converting gas into stars) rather than a cosmological one, it would follow that the total contribution to the cosmic SFRD from protoclusters would be even greater than the Chiang et al. (2017) [36] estimate. Separating out these effects will be challenging, however, and will require a much larger sample of protoclusters and a better characterization of halo statistics in different environments.

3.6.3 Search of progenitors of a brightest cluster galaxy

Brightest cluster galaxies (BCGs) are the most massive galaxies in galaxy clusters. In the local universe, they are typically elliptical galaxies residing near the cluster center defined by X-ray emission peak [232]. Identification and characterization of their progenitors ('proto-BCGs') at high redshift would illuminate the early stages of their formation.

At $z \sim 3$, the rest-frame optical/near-IR luminosity ($0.5-1.6\mu$m) tracing the total stellar content is redshifted into the K_S band and beyond. Thus, the most effective search should be based on the photometric properties at infrared wavelengths. Although the D1 field was imaged in the near-IR JHK_S bands by the WIRCam Deep Survey [233], the newly discovered galaxy overdensities unfortunately lie near the edge of its coverage (see their Figure 2 for the coverage map). ≈20% of the area enclosing the 'A' and 'B+C' structures has no K_S band coverage while an additional 10% of the area has only partial coverage (<50% of the full exposure 4.7 hr). A more comprehensive search of massive galaxies in this region based on the Spitzer IRAC 3.6μm detection will be presented in the future (J. Toshikawa et al., in prep, K. Shi et al., in prep).

In this work, we opt to base our proto-BCG search on our existing LBG catalog instead, focusing on UV-luminous galaxies that already have a large stellar content. We require that a given galaxy must have the r-band magnitude $r \leq 24$ (roughly corresponding to $\geq 1.6L^{*}_{\mathrm{UV},z\sim3}$ [171]). In addition, to further constrain its stellar mass, it should also be well detected in the K_S band catalog. A total of 80 galaxies satisfy these criteria, corresponding to a surface density of 0.06$\pm$0.01 arcmin^{-2}. We caution that our following discussion is limited by the incomplete coverage of the K_S band data, and only future deeper target survey can give us a more complete census of different galaxy constituents within this protocluster.

In the top panel of Fig. 3.9, we show the $J-K_S$ colors vs K_S band magnitudes for all selected sources. The majority have $K_S > 22.5$ and relatively blue $J-K_S$ colors. Using the EZGal software [119], we also compute the expected color and luminosity evolution assuming several different star formation histories. The stellar population synthesis models from [234] and local starburst-like dust reddening curve [110] are adopted for the calculation. The model magnitudes are normalized to a lower redshift ($z = 1.8$) $M_\star$ cluster galaxy in the 3.6μm band [58], assuming passive evolution from $z \sim 3.1$ to $z \sim 1.8$. The model tracks represent the time evolution of the galaxy.

Of the 80 galaxies, only four reside in the combined LBG and LAE overdensity region. The area covered by the WIRDS data is 93.7 arcmin^2 , and thus the expected number therein is 6 ± 2. The K_S-brightest galaxy ($K_S = 21.05$), which we dub G411155, is shown as a red circle in the left panel of Fig. 3.9. Its location is also marked in Fig. 3.6 (orange square). G411155 is the reddest LBG in the entire field ($J-K_S = 1.92$), and would easily meet a typical color selection for distant red galaxies (DRGs) at high redshift ($J-K_S > 1.4$) [112, 235]. G411155 is very bright in the IRAC 8μm and the MIPS 24μm bands, having the flux densities of 0.13 mJy and 1.43 mJy, respectively. The remaining three galaxies have relatively modest K_S band brightness ($K_S = 23-24$) and are bluer ($J-K_S < 1.4$). None of the five galaxies has a X-ray or radio counterpart [210, 236].

Using the catalogs from [233] and [216], we extract the multi-wavelength photometry ($ugrizJHK_S$[3.6][4.5][5.8][8.0][24][70][160]) of G411155 using the Kron-like total fluxes. We perform the SED fitting with the CIGALE software [107] using both galaxy and AGN templates. Star formation histories are modeled as an exponentially declining function with the characteristic timescale τ values of 100 Myr to 1 Gyr. AGN models from [237] are used as templates.

In Fig. 3.9 (bottom), we show the best-fit SED model together with the photometric measurements. In the inset, we also show the photometric redshift probability density which peaks at $z \sim 3.1$. The best-fit physical parameters suggest that G411155 has a short star-forming time scale with the luminosity-weighted age of ≈200 Myr. The model fit also suggests a dust-obscured AGN component which dominates the infrared energy budget: 70% of the total IR luminosity originates from the AGN. The galaxy is already ultramassive at $M_{\rm star} \approx 2 \times 10^{11} M_\odot$, and it continues to form stars at a rate SFR $\sim 500 M_\odot {\rm yr}^{-1}$!

We compare our proto-BCG candidate with those found in the literature. Lemaux et al. (2014) [33] identified a proto-BCG candidate in a $z \sim 3.3$ protocluster. It contains a powerful Type I AGN (relatively unobscured by dust with broad lines) with a K_S band magnitude of 20.67 ($z - K_S = 0.1$) with the estimated stellar mass and age of $\sim 8 \times 10^{10} M_\odot$ and ~ 300 Myr. The SFR inferred from the total IR luminosity is $\sim 750\ M_\odot {\rm yr}^{-1}$. Although we do not have a spectrum for G411155, these two proto-BCG candidates have comparable physical properties.

Near the center of a protocluster at $z = 3.09$, Kubo et al. (2015,2016) [150, 164] discovered a dense group of massive galaxies consisting of seven K_S bright ($K_S \sim 22 - 24$) and red galaxies ($J - K_S > 1.1$) with a combined stellar mass of $\approx 6 \times 10^{11} M_\odot$. They argued that the group is likely in the merger phase which will evolve into a BCG observed in the local universe. Wang et al. (2016) [149] reported an overdensity of 11 massive ($\geq 10^{11} M_\odot$) DRGs within a compact core (80 kpc) in another $z = 2.51$ structure, and speculated that their findings may signify a rapid buildup of a cluster core. Identifying and studying similar systems in a larger sample of protoclusters will elucidate evolutionary stages of cluster BCGs.

Finally, G411155 lies very close to the spectroscopic sources at $z = 3.13$, in particular four sources two of which are also LAEs, as illustrated in Fig. 3.6. Given its photometric redshift (see inset of Fig. 3.9), it is possible that these galaxies are members of the same group, which is falling towards the center of its parent halo located ≈1 Mpc (physical) away from it. Given its optical brightness, it should be relatively easy to measure its redshift and thereby unambiguously determine its physical association with these sources.

3.6.4 On the possible configuration of the structures and their constituents

The observational data presented in this work paints an incomplete picture leaving several unanswered questions. First, the spatial segregation between the LAE- and LBG-traced structure is puzzling because the spectroscopically confirmed sources in the latter lie at the same redshift as the former. If the galaxies in the LBG overdensity trace a single structure, the implication would be that the structure 'A' genuinely lacks Lyα-emitting galaxies whereas the structure 'B+C' is populated by both LAEs and LBGs (and one large Lyα nebula).

Secondly, the projected end-to-end size of the combined structure is ≈ 30 Mpc, much larger than the theoretical expectations (the projected diameter of what would end up fully virialized by $z = 0$ ranges in 15–20 Mpc [37]); recent size estimates of several confirmed protoclusters agree with this prediction [46, 79]. If the two overdensities belong to the same underlying structure, it follows that they will form into a more massive cluster of $M_{\rm tot} \approx 2 \times 10^{15} M_\odot$ by present-day, making it a large massive cosmic structure rarely seen in observations.

If 'A' and 'B+C' represent two separate systems, we speculate several physical scenarios consistent with the current observational constraints. First, we may be witnessing a baryonic response to the well-known *halo assembly bias*: i.e., the spatial distribution of dark matter halos depends not only on mass but their formation time and other dynamical properties such as concentration and spin [238–241]. The 'B+C' structure may have formed more recently than the 'A', and thus is traced by numerous young and low-mass galaxies many of which are observed as LAEs. In comparison, as an older and more settled system, the 'A' protocluster may be dominated by more massive star-forming galaxies, which are observed as LBGs. In this conjecture, it follows that both LAE- or LBG-based protocluster searches would be sensitive to different evolutionary stages (or ages) of cluster formation in which the former (latter) method favors younger (older) structures.

One corollary to this hypothesis would be that the presence of galaxies with old stellar populations should be predominantly found in the LBG-selected structures but not in LAE-traced ones. Observationally, several studies reported an excess number of old and/or massive galaxies in the region of LBG or photo-z overdensities [20, 149, 224]; however, there is little to no observation that conclusively determined the presence of massive old galaxies in LAE-dominated ones. Validation of such a scenario requires a statistical approach where large samples of LBG- and LAE-selected overdensities are identified independently, and compared for the level of their cohabitation.

Alternatively, the spectroscopically confirmed sources embedded in the 'A' region may be spatially disjoint from the majority of LBGs therein, and are part of a small group falling in towards the 'B+C' structure. The 'A' region then could represent just another protocluster with no physical association with the LAE overdensity. Only extensive spectroscopy in all of the 'A+B+C' regions can elucidate the true configurations of these structures.

Finally, we contemplate on the significance of the Lyα nebula in the context of protocluster formation. As described in § 3.4.3, our search of the entire field resulted in a single LAB. The fact that it is located at the southwestern end of the LAE overdensity ('B+C') is significant.

There is mounting evidence that luminous Lyα nebulae are preferentially found in dense environments. Matsuda et al. (2014) [71] identified 35 Lyα nebulae candidates in an LAE and LBG rich protocluster at $z = 3.09$, and reported that the LAEs and LABs trace one another. Yang et al. (2010) [197] conducted a systematic search for LABs in four separate fields, each comparable in size to our survey field. The number of LAB they identified in each field ranged in 1–16; they argued that high cosmic variance implies a very large galaxy bias expected for group-sized halos. Small groups of galaxies are observed to be embedded in several luminous blobs [72, 242–244] in agreement with the assessment from [197].

It is notable that LAB17139 lies at the periphery of the 'B+C' overdensity traced by LAEs. Recently, Badescu et al. (2017) [79] compiled the LAE/LAB data for five protoclusters at $z = 2.3$ and $z = 3.1$, and showed that LABs are preferentially found in the outskirts of each of the LAE overdensities. They speculated that these blobs may be signposts for group-sized halos (harboring galaxy 'proto-groups') falling in towards the cluster-sized parent halo traced by LAEs where Lyα-lit gas traces the stripped gas from galaxy-galaxy interactions.

A significant variation of their numbers implies a relatively short timescale for the LAB phenomenon; that combined with their preferred locations at the outskirts requires a physical explanation involving the proto-cluster environment. The kinematics of protocluster galaxies showing relatively low velocity dispersions[2] and in multiple groupings (< 400 km s^{-1} [46]) indicate that the structure is far from virialization.

If a galaxy overdensity is a superposition of multiple overdensities in physical proximity, LAB's preferred location at their outskirts may signify their first group-group interactions enabling a host of galaxy-galaxy interactions which in turn bring about starbursts, AGN, and stripped gas lighting up an extended region surrounding these galaxies.

3.7 Summary

In this paper, we initially set out to investigate a large-scale structure around a significant LBG overdensity in the CFHTLS D1 field. A subset of these galaxies were targeted by Toshikawa et al. (2016) [47], and five are confirmed to lie at $z_{\rm spec} = 3.13$. At this redshift, Lyα emission is conveniently redshifted into a zero-redshift [O III] filter, providing a rare opportunity to examine how the same structure is populated by galaxies of different spectral types, thereby evaluating the efficiency of different search techniques for high-redshift protoclusters. To this end, we have obtained new deep observations using the Mosaic $o3$ filter; by combining the data with the existing broad-band observations, 93 LAE candidates are identified at $z = 3.11 - 3.15$.

The angular distribution of these LAEs is clearly non-uniform, revealing a prominent overdensity at the western end of the field containing 21 galaxies along with a luminous Lyα nebula. The angular size and level of the LAE overdensity are consistent with those observed for several confirmed protoclusters. However, our comparison of the LAE and LBG distributions has resulted in a surprising discovery: the LAE-rich region is spatially offset from the LBG-rich region. In the latter, there is a general dearth of LAEs while the

[2] Matsuda et al. (2005) [86] reported a much larger velocity dispersion of $\sim$1100 km s^{-1} for the SSA22a protocluster at $z = 3.09$; however, the spectroscopic LAEs have at least three separate groups. We estimate that the velocity dispersion of each group does not exceed 500 km s-1 [46].

LAE overdensity is also populated by LBG candidates. Our findings paint a more complex picture of cluster formation in which the halo assembly bias may play a significant role in determining a dominant type of galaxy constituents therein. Based on our investigations, we conclude the following:

- We report a significant LAE overdensity located $10'$ south of the five spectroscopic sources at $z = 3.13$. The observed surface density therein is higher than that expected in an average field by a factor of 3.3 ± 0.9. The total mass enclosed in the overdensity is estimated to be $M_{\rm tot} \approx (1.0 - 1.5) \times 10^{15} M_{\odot}$, implying that the LAE overdensity traces a massive structure that will evolve into a galaxy cluster similar to the present-day Coma.

- We analyze the LBG overdensity based on the existing deep broad-band observations to evaluate its significance and contemplate on its possible relationship with the LAE-traced protocluster. Given the angular extent and the level of overdensity, we conclude that it will also evolve into a Coma-sized galaxy cluster. If the two overdensites lie at the same redshift, their dynamical timescale is short enough that they would merge into a single more massive cluster by the present-day epoch.

- If the spatial segregation of the LAE and LBG-rich structures is interpreted as a manifestation of the halo assembly bias, it follows that different search techniques would be biased accordingly to the formation age of the host halo. With multiple upcoming wide-field surveys will be targeting both types of galaxies (e.g., Hobby-Eberly telescope dark energy experiment, Large synoptic survey telescope), testing this hypothesis will be within reach in the next decade. Such studies will lead us to deeper understanding of early stages of galaxy formation in dense cluster environments, and help us optimize search techniques to reliably identify and study progenitors of massive galaxy clusters.

- We find tentative evidence that the median SFR is higher for Lyα-emitting galaxies in protocluster environment. When our LAE candidates are split accordingly to their 2D environment, the LAEs residing in the overdensity consistently have larger Lyα and UV luminosities – by $\sim 40\%$ and $\sim 70\%$, respectively – than the rest, in agreement with our previous study based on another protocluster [46]. The enhancement appears to be widespread within the overdensity region with no clear radial dependence. The difference cannot be explained by the galaxy overdensity alone, and may require either a top-heavy mass function or a higher star formation efficiency for protocluster halos.

- Our search for Lyα nebulae in the entire field yields a single nebula with the total Lyα luminosity $\approx 2 \times 10^{43}$ erg s^{-1} and the half-light radius (assuming an exponentially declining profile) of at least $5''$ (39 kpc at $z = 3.13$). Its location at the outer edge of the LAE overdensity may support a physical picture advocated by [79], that Lyα nebulae trace group-sized halos falling in towards the protocluster center. The large variations seen in the observed number of Lyα nebulae around protoclusters hint at the short-lived nature of the phenomenon, perhaps brought on by galaxy-galaxy interactions.

- We have also identified a brightest cluster galaxy candidate located $\approx 2'$ from the center of the LBG overdensity. The galaxy is one of the brightest LBGs in our sample, and has already assembled a stellar mass of $\approx 2 \times 10^{11} M_{\odot}$. A full SED modeling suggests that a highly dust-obscured AGN dominates its mid-infrared flux at $\lambda_{\rm obs} > 8\mu$m while still active star formation is responsible for a fairly reddened rest-frame UV and optical part of its SED. While the AGN-driven quenching of star formation in an already massive cluster galaxy fits the general expectation of how and when cluster galaxies formed, further validation is needed to determine whether it is physically associated with the galaxy overdensity.

Table 3.3.
Key physical properties of LAEs in different environments

	N	$W_{0,\mathrm{Ly}\alpha}$ [Å]	$\log(L_{\mathrm{UV,obs}})$ [erg s^{-1} Hz^{-1}]	$\log(L_{\mathrm{Ly}\alpha\mathrm{,obs}})$ [erg s^{-1}]	E$(B-V)$	SFR$_{\mathrm{UV,cor}}$ [M$_\odot$ yr^{-1}]
All Galaxies						
Overdensity	24	75 (57) $\pm$ 16	28.05 (28.08) $\pm$ 0.08	42.57 (42.53) $\pm$ 0.05	-	-
Field	69	104 (53) $\pm$ 16	27.81 (27.84) $\pm$ 0.06	42.45 (42.38) $\pm$ 0.04	-	-
All	93	96 (55) $\pm$ 13	27.87 (27.93) $\pm$ 0.05	42.52 (42.42) $\pm$ 0.03	-	-
Galaxies with β Measurements						
Overdensity	21	52 (49) $\pm$ 5	28.20 (28.24) $\pm$ 0.07	42.67 (42.65) $\pm$ 0.05	0.11 (0.06) $\pm$ 0.03	15 (6) $\pm$ 6
Field	42	62 (46) $\pm$ 9	28.00 (27.99) $\pm$ 0.06	42.48 (42.38) $\pm$ 0.05	0.13 (0.14) $\pm$ 0.02	10 (5) $\pm$ 2
All	63	59 (47) $\pm$ 6	28.06 (28.05) $\pm$ 0.05	42.52 (42.42) $\pm$ 0.04	0.13 (0.10) $\pm$ 0.02	11 (5) $\pm$ 2

Note: The values represent means of key physical properties (medians in the brackets) with uncertainties for each sample.

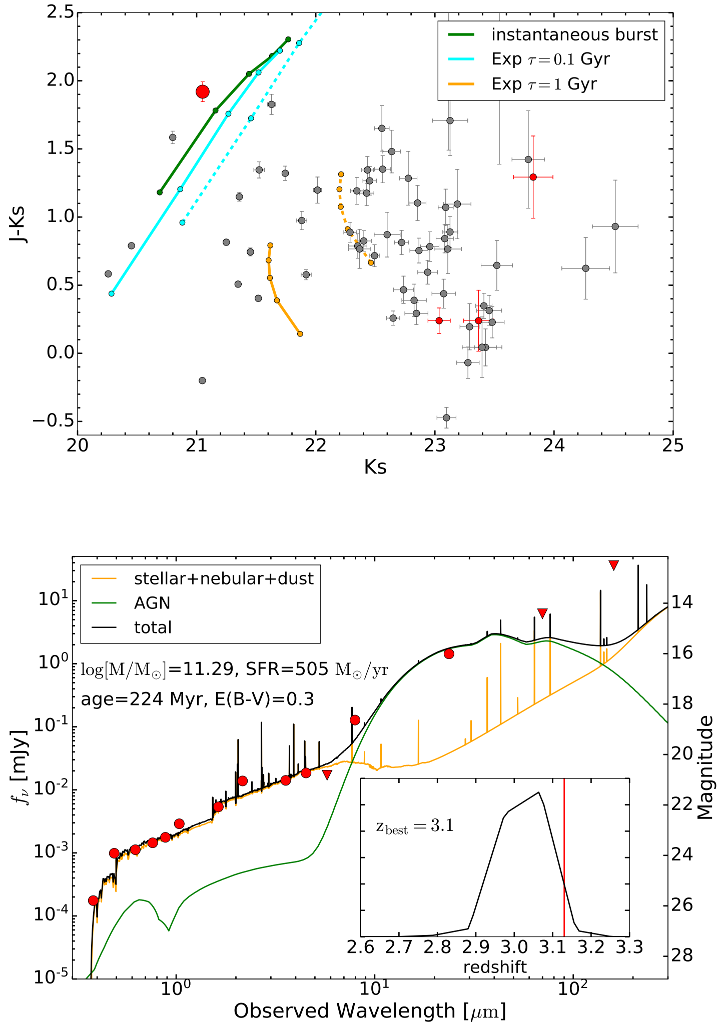

Fig. 3.9. *Top:* A color-magnitude diagram of UV-luminous LBGs with K_S band detection ($r \leq 24$: grey circles). The proto-BCG candidate, G411155 (large red circle), is the reddest LBG and also one of the brightest in the K_S band. Three other LBGs near the LAE/LBG overdensities are shown as smaller red circles. Colored lines represent galaxies that formed through an instantaneous burst (green), and with an exponentially declining SF history with τ values of 100 Myr (cyan) and 1 Gyr (yellow); all are observed at $z = 3.1$ with the population age of 0.2 Gyr (bottom) to 1.0 Gyr with a stepsize of 0.2 Gyr. For the exponentially declining models, we also show the color tracks assuming the reddening E$(B-V) = 0.2$ as dashed lines. *Bottom:* The best-fit SED model of G411155 is shown in black together with the photometric measurements (red symbols) and best-fit parameters. The galaxy (stars+gas+dust) and AGN components are shown in orange and green, respectively. In the inset, we show the photometric redshift probability density. The red vertical line marks $z = 3.13$, the redshift of the spectroscopic sources within the LBG overdensity.

4. SUMMARY AND OUTLOOK

4.1 Summary

Understanding galaxy formation and evolution is a crucially important task in modern astronomy. Galaxy clusters, as the densest structures observed in the Universe, provide us a unique laboratory to study how galaxy formation proceed in the dense environments. To directly witness the initial stage of cluster formation, it is necessary to search and study progenitors of clusters, namely protoclusters at high redshift ($z > 2$), when the cosmic star-formation rate density was at its peak and most of the stellar mass was assembled into individual galaxies. In this thesis, I have presented our search and investigations on two protoclusters at $z = 3.78$ and $z = 3.13$ respectively, focusing on their galaxy constituents and environmental impacts. Based on these studies, I summarize our results below.

In Chapter 2, we present a detailed census of galaxies in and around a spectroscopically confirmed protocluster PC 217.96+32.3 at $z = 3.78$. Utilizing the SED-fitting technique on multiwavelength data, we identify various types of galaxies in the protocluster field. The star-forming galaxies whose photometric redshifts are consistent with the protocluster redshift form a large overdensity in the field, which is estimated to evolve into a Coma-like cluster ($\sim 10^{15}$ $M_\odot$) by present day. However, the overdensity region is spatially offset from the previously confirmed LAE members by several Mpc. It is speculated that PC 217.96+32.3 may be larger than previously thought, half of which is missed by the LAE selection. Alternatively, the newly discovered overdensity may represent another protocluster not associated with PC 217.96+32.3. However, cosmological simulations suggested that both scenarios are unlikely ($< 1\%$) in our survey volume, which calls for future spectroscopic observations on these photometric redshift selected galaxies.

We also identify a large excess of massive ($\geq 10^{11}$ $M_\odot$) quiescent and post-starburst galaxies exhibiting a strong Balmer/4000 Å break (BBGs) in the protocluster field, suggesting that massive galaxies already quenched their star-formation as early as $z \sim 4$ with a formation epoch beyond $z > 5$. In addition, the BBGs show the largest overdensity as compared to less massive LAEs and LBGs, indicating they are more biased tracers of the underlying dark matter distribution, thus highlight the importance of using low mass galaxies such as LAEs to identify protoclusters more robustly.

Comparing the physical properties (e.g., stellar mass, star-formation rate) between the galaxies within the protocluster region and those outside, we do not find obvious differences between the two groups, suggesting that the environmental impacts are minimal at this redshift, or alternatively the high dense environment produces extremely dusty starburst galaxies which are completely missed by our selection of protocluster galaxy candidates. Only future deep infrared and submillimeter survey on this field can give us a definite answer.

In Chapter 3, motivated by a previous discovery of a massive protocluster at $z = 3.13$, we conduct a LAE survey in the protocluster field to examine how the same structure is populated by lower mass LAEs. The identified LAEs form a significant overdensity which is predicted to evolve into a Coma-like cluster by present day. However, the LBG overdensity identified from existing data is spatially segregated from the LAE overdensity. It is argued that the discrepancy may signal the role of halo assembly bias in galaxy formation within clusters, that is, the properties of galaxies depend not only on the underlying halo mass, but also on its formation time. Therefore, the LBGs overdensity may represent an older and more settled system while the LAE overdensity is traced by young and less massive galaxy population, which would suggest that different search techniques may be biased according to the formation age of the host dark matter halo.

We also find a luminous Lyα nebula located at the edge of the LAE overdensity, supporting the idea that Lyα nebulae may trace group-sized halos falling into the protocluster center. A brightest cluster galaxy candidate is also identified in the LBG overdense region. The galaxy is one of the brightest LBGs in our sample with a mass of 2×10^{11} $M_{\odot}$. SED fitting suggests that it is dominated by a high dust-obscured AGN in its infrared wavelength. It is young and still actively forming stars, likely indicating an early and accelerated mass assembly of cluster galaxies, consistent with existing studies.

By studying the LAE properties within and outside the protocluster region, we find tentative evidence that the star-formation activity is enhanced in the protocluster environment, which may indicate that the fractional contribution of the protocluster galaxies to the total star-formation rate density would be higher than previously thought.

All in all, our studies on the two protoclusters give us an opportunity to witness the early stage of cluster formation, when the Universe was only $\sim$2 billion years old. By using different selection techniques, we identify various types of galaxies in the protocluster fields. These galaxies form into large overdensities which would later become massive clusters by present day. Intriguingly, both studies show a discrepancy between the spatial distributions of different galaxy populations. It is possible that different selection techniques we used may be biased by their covered redshift range, or by the intrinsic difference of the formation age of the underlying dark matter halo. We also investigate the environmental impacts on galaxy properties in the two protoclusters. In the $z = 3.78$ protocluster study, we do not find obvious evidence of environmental effects on the protocluster galaxies, while for the other protocluster at $z = 3.13$ we find weak evidence for the enhancement of star-formation of protocluster galaxies. At a first glance, the results from the two studies seem contradictory. However, it is worth noting that the former study focuses on UV-luminous, LBG-like galaxies while the latter on UV-faint, less massive LAEs. Therefore to discern a clearer environmental trend and to study how it depends on galaxy's luminosity and stellar mass as well as galaxy types, a more comprehensive study is needed. Nevertheless, our studies shed light on the formation of galaxies in the dense protocluster environments and paint a picture of how different types of galaxies populate the underlying large-scale structure.

4.2 Outlook

While this thesis uncovers some interesting properties about the protoclusters and their galaxy constituents as well as the environmental impacts, there remain some unanswered questions. In this section I briefly discuss these questions and potential future work as the extension of this thesis.

First and foremost, most of our studies are based on photometric observations, which result in large redshift uncertainties in our galaxy samples. In our first work, the photo-z protocluster galaxies are selected using SED fitting, with typical redshift uncertainties

$\Delta z \sim 0.4$. We found that there is an offset between the photo-z overdensity and LAE overdensity, but the exact reason is unclear. Due to the large redshift uncertainties, the significant photo-z overdensity could be contaminated by the foreground or background interlopers. Therefore to illuminate this problem, future spectroscopic observations on these photo-z galaxies are needed to confirm their redshifts and to further determine the significance of this photo-z overdensity. The same is true for our second work, where only a few of the LBGs have spectroscopic redshifts, preventing us from uncovering the relation between the LBG overdensity and LAE overdenisty. In addition, spectroscopy of the Balmer-break galaxies can also help us verify their redshifts and stellar population properties.

Second, in our $z = 3.13$ protocluster study, the field is covered by both the existing near-IR (JHK_S) and IR bands ([3.6][4.5][5.8][8.0]). The brightest cluster galaxy candidate we discovered is selected from our LBG sample, due to the uneven coverage of the K_S band data. However, the entire field is covered by the IR bands, so it is possible to conduct a more comprehensive study of the galaxy constituents in this protocluster based on the 3.6μm detection. Similar to our first work, I plan to do a census of its galaxy constituents using the SED-fitting technique, to determine galaxy properties and to search for potential photo-z overdensity and compare with that of LAEs and LBGs. I would also like to search for quiescent galaxy candidates in this protocluster, exploring the possible early quenching effect in this protocluster field.

Finally, future powerful telescopes such as James Webb Space Telescope (JWST) will illuminate how protocluster galaxies form and evolve while other upcoming surveys such as Dark Energy Spectroscopic Instrument (DESI) and The Large Synoptic Survey Telescope (LSST) will discover more similarly massive protoclusters. With the help of these telescopes and surveys, we will be able to further understand the early stage of cluster formation as well as galaxy formation within these protoclusters.

REFERENCES

REFERENCES

[1] A. H. Guth, "Inflationary universe: A possible solution to the horizon and flatness problems," *Phys. Rev. D*, vol. 23, pp. 347–356, Jan 1981. [Online]. Available: https://link.aps.org/doi/10.1103/PhysRevD.23.347

[2] A. D. Linde, *Phy. Lett.*, vol. B108, p. 389, 1982.

[3] A. D. Linde, "Chaotic inflation," *Physics Letters B*, vol. 129, pp. 177–181, Sep. 1983.

[4] A. Albrecht and P. J. Steinhardt, "Cosmology for grand unified theories with radiatively induced symmetry breaking," *Phys. Rev. Lett.*, vol. 48, pp. 1220–1223, Apr 1982. [Online]. Available: https://link.aps.org/doi/10.1103/PhysRevLett.48.1220

[5] P. J. E. Peebles, "Recombination of the Primeval Plasma," *ApJ*, vol. 153, p. 1, Jul. 1968.

[6] A. A. Penzias and R. W. Wilson, "A Measurement of Excess Antenna Temperature at 4080 Mc/s." *ApJ*, vol. 142, pp. 419–421, Jul. 1965.

[7] D. N. Spergel, R. Bean, O. Doré, M. R. Nolta, C. L. Bennett, J. Dunkley, G. Hinshaw, N. Jarosik, E. Komatsu, L. Page, H. V. Peiris, L. Verde, M. Halpern, R. S. Hill, A. Kogut, M. Limon, S. S. Meyer, N. Odegard, G. S. Tucker, J. L. Weiland , E. Wollack, and E. L. Wright, "Three-Year Wilkinson Microwave Anisotropy Probe (WMAP) Observations: Implications for Cosmology," *The Astrophysical Journal Supplement Series*, vol. 170, pp. 377–408, Jun 2007.

[8] J. H. Jeans, "The Stability of a Spherical Nebula," *Philosophical Transactions of the Royal Society of London Series A*, vol. 199, pp. 1–53, 1902.

[9] S. D. M. White and M. J. Rees, "Core condensation in heavy halos - A two-stage theory for galaxy formation and clustering," *MNRAS*, vol. 183, pp. 341–358, May 1978.

[10] A. G. Riess, A. V. Filippenko, P. Challis, A. Clocchiatti, A. Diercks, P. M. Garnavich, R. L. Gilliland, C. J. Hogan, S. Jha, R. P. Kirshner, B. Leibundgut, M. M. Phillips, D. Reiss, B. P. Schmidt, R. A. Schommer, R. C. Smith, J. Spyromilio, C. Stubbs, N. B. Suntzeff, and J. Tonry, "Observational Evidence from Supernovae for an Accelerating Universe and a Cosmological Constant," *AJ*, vol. 116, pp. 1009–1038, Sep 1998.

[11] S. Perlmutter, G. Aldering, G. Goldhaber, R. A. Knop, P. Nugent, P. G. Castro, S. Deustua, S. Fabbro, A. Goobar, D. E. Groom, I. M. Hook, A. G. Kim, M. Y. Kim, J. C. Lee, N. J. Nunes, R. Pain, C. R. Pennypacker, R. Quimby, C. Lidman, R. S. Ellis, M. Irwin, R. G. McMahon, P. Ruiz-Lapuente, N. Walton, B. Schaefer, B. J. Boyle, A. V. Filippenko, T. Matheson, A. S. Fruchter, N. Panagia, H. J. M. Newberg, W. J. Couch, and T. S. C. Project, "Measurements of Ω and Λ from 42 High-Redshift Supernovae," *ApJ*, vol. 517, no. 2, pp. 565–586, Jun 1999.

[12] Planck Collaboration, P. A. R. Ade, N. Aghanim, C. Armitage-Caplan, M. Arnaud, M. Ashdown, F. Atrio-Barandela, J. Aumont, C. Baccigalupi, A. J. Banday, and et al., "Planck 2013 results. XVI. Cosmological parameters," *ArXiv e-prints*, Mar. 2013.

[13] M. Boylan-Kolchin, V. Springel, S. D. M. White, A. Jenkins, and G. Lemson, "Resolving cosmic structure formation with the Millennium-II Simulation," *MNRAS*, vol. 398, pp. 1150–1164, Sep 2009.

[14] R. S. Somerville and J. R. Primack, "Semi-analytic modelling of galaxy formation: the local Universe," *MNRAS*, vol. 310, pp. 1087–1110, Dec. 1999.

[15] G. Kauffmann, J. M. Colberg, A. Diaferio, and S. D. M. White, "Clustering of galaxies in a hierarchical universe - I. Methods and results at z=0," *MNRAS*, vol. 303, pp. 188–206, Feb. 1999.

[16] J. Silk and M. J. Rees, "Quasars and galaxy formation," *A&A*, vol. 331, pp. L1–L4, Mar. 1998.

[17] A. C. Fabian, "Observational Evidence of Active Galactic Nuclei Feedback," *Annual Review of Astronomy and Astrophysics*, vol. 50, pp. 455–489, Sep 2012.

[18] A. Dressler, "Galaxy morphology in rich clusters - Implications for the formation and evolution of galaxies," *ApJ*, vol. 236, pp. 351–365, Mar. 1980.

[19] T. Goto, C. Yamauchi, Y. Fujita, S. Okamura, M. Sekiguchi, I. Smail, M. Bernardi, and P. L. Gomez, "The morphology-density relation in the Sloan Digital Sky Survey," *MNRAS*, vol. 346, pp. 601–614, Dec. 2003.

[20] C. C. Steidel, K. L. Adelberger, A. E. Shapley, D. K. Erb, N. A. Reddy, and M. Pettini, "Spectroscopic Identification of a Protocluster at z=2.300: Environmental Dependence of Galaxy Properties at High Redshift," *ApJ*, vol. 626, pp. 44–50, Jun. 2005.

[21] P. G. van Dokkum and R. P. van der Marel, "The Star Formation Epoch of the Most Massive Early-Type Galaxies," *ApJ*, vol. 655, pp. 30–50, Jan. 2007.

[22] P. R. M. Eisenhardt, M. Brodwin, A. H. Gonzalez, S. A. Stanford, D. Stern, P. Barmby, M. J. I. Brown, K. Dawson, A. Dey, M. Doi, A. Galametz, B. T. Jannuzi, C. S. Kochanek, J. Meyers, T. Morokuma, and L. A. Moustakas, "Clusters of Galaxies in the First Half of the Universe from the IRAC Shallow Survey," *ApJ*, vol. 684, pp. 905–932, Sep. 2008.

[23] N. A. Hatch, J. D. Kurk, L. Pentericci, B. P. Venemans, E. Kuiper, G. K. Miley, and H. J. A. Röttgering, "Hα emitters in z $\sim$ 2 protoclusters: evidence for faster evolution in dense environments," *MNRAS*, vol. 415, pp. 2993–3005, Aug. 2011.

[24] K. Husband, M. N. Bremer, J. P. Stott, and D. N. A. Murphy, "Early quenching of massive protocluster galaxies around z = 2.2 radio galaxies," *MNRAS*, vol. 462, pp. 421–428, Oct. 2016.

[25] R. Shimakawa, T. Kodama, M. Hayashi, J. X. Prochaska, I. Tanaka, Z. Cai, T. L. Suzuki, K.-i. Tadaki, and Y. Koyama, "MAHALO Deep Cluster Survey I. Accelerated and enhanced galaxy formation in the densest regions of a protocluster at z = 2.5," *MNRAS*, vol. 473, pp. 1977–1999, Jan. 2018.

[26] R. C. W. Houghton, "Revisiting the original morphology-density relation," *MNRAS*, vol. 451, pp. 3427–3436, Aug 2015.

[27] D. Elbaz, E. Daddi, D. Le Borgne, M. Dickinson, D. M. Alexander, R.-R. Chary, J.-L. Starck, W. N. Brandt, M. Kitzbichler, E. MacDonald, M. Nonino, P. Popesso, D. Stern, and E. Vanzella, "The reversal of the star formation-density relation in the distant universe," *A&A*, vol. 468, pp. 33–48, Jun. 2007.

[28] M. C. Cooper, J. A. Newman, B. J. Weiner, R. Yan, C. N. A. Willmer, K. Bundy, A. L. Coil, C. J. Conselice, M. Davis, S. M. Faber, B. F. Gerke, P. Guhathakurta, D. C. Koo, and K. G. Noeske, "The DEEP2 Galaxy Redshift Survey: the role of galaxy environment in the cosmic star formation history," *MNRAS*, vol. 383, pp. 1058–1078, Jan. 2008.

[29] K.-V. H. Tran, C. Papovich, A. Saintonge, M. Brodwin, J. S. Dunlop, D. Farrah, K. D. Finkelstein, S. L. Finkelstein, J. Lotz, R. J. McLure, I. Momcheva, and C. N. A. Willmer, "Reversal of Fortune: Confirmation of an Increasing Star Formation-Density Relation in a Cluster at z = 1.62," *ApJL*, vol. 719, pp. L126–L129, Aug. 2010.

[30] Y. Koyama, I. Smail, J. Kurk, J. E. Geach, D. Sobral, T. Kodama, F. Nakata, A. M. Swinbank, P. N. Best, M. Hayashi, and K.-i. Tadaki, "On the evolution and environmental dependence of the star formation rate versus stellar mass relation since z $\sim$ 2," *MNRAS*, vol. 434, pp. 423–436, Sep. 2013.

[31] J. S. Santos, B. Altieri, M. Tanaka, I. Valtchanov, A. Saintonge, M. Dickinson, S. Foucaud, T. Kodama, T. D. Rawle, and K. Tadaki, "Star formation in the cluster CLG0218.3-0510 at z = 1.62 and its large-scale environment: the infrared perspective," *MNRAS*, vol. 438, pp. 2565–2577, Mar. 2014.

[32] N. Welikala, M. Béthermin, D. Guery, M. Strandet, K. A. Aird, M. Aravena, M. L. N. Ashby, M. Bothwell, A. Beelen, L. E. Bleem, C. de Breuck, M. Brodwin, J. E. Carlstrom, S. C. Chapman, T. M. Crawford, H. Dole, O. Doré, W. Everett, I. Flores-Cacho, A. H. Gonzalez, J. González-Nuevo, T. R. Greve, B. Gullberg, Y. D. Hezaveh, G. P. Holder, W. L. Holzapfel, R. Keisler, G. Lagache, J. Ma, M. Malkan, D. P. Marrone, L. M. Mocanu, L. Montier, E. J. Murphy, N. P. H. Nesvadba, A. Omont, E. Pointecouteau, J. L. Puget, C. L. Reichardt, K. M. Rotermund, D. Scott, P. Serra, J. S. Spilker, B. Stalder, A. A. Stark, K. Story, K. Vanderlinde, J. D. Vieira, and A. Weiß, "Probing star formation in the dense environments of z $\sim$ 1 lensing haloes aligned with dusty star-forming galaxies detected with the South Pole Telescope," *MNRAS*, vol. 455, pp. 1629–1646, Jan. 2016.

[33] B. C. Lemaux, O. Cucciati, L. A. M. Tasca, O. Le Fèvre, G. Zamorani, P. Cassata, B. Garilli, V. Le Brun, D. Maccagni, L. Pentericci, R. Thomas, E. Vanzella, E. Zucca, R. Amorín, S. Bardelli, P. Capak, L. P. Cassarà, M. Castellano, A. Cimatti, J. G. Cuby, S. de la Torre, A. Durkalec, A. Fontana, M. Giavalisco, A. Grazian, N. P. Hathi, O. Ilbert, C. Moreau, S. Paltani, B. Ribeiro, M. Salvato, D. Schaerer, M. Scodeggio, V. Sommariva, M. Talia, Y. Taniguchi, L. Tresse, D. Vergani, P. W. Wang, S. Charlot, T. Contini, S. Fotopoulou, R. R. Gal, D. D. Kocevski, C. López-Sanjuan, L. M. Lubin, Y. Mellier, T. Sadibekova, and N. Scoville, "VIMOS Ultra-Deep Survey (VUDS): Witnessing the assembly of a massive cluster at z ˜ 3.3," *A&A*, vol. 572, p. A41, Dec. 2014.

[34] B. C. Lemaux, O. Le Fèvre, O. Cucciati, B. Ribeiro, L. A. M. Tasca, G. Zamorani, O. Ilbert, R. Thomas, S. Bardelli, P. Cassata, N. P. Hathi, J. Pforr, V. Smolčić, I. Delvecchio, M. Novak, S. Berta, H. J. McCracken, A. Koekemoer, R. Amorín, B. Garilli, D. Maccagni, D. Schaerer, and E. Zucca, "The VIMOS Ultra-Deep Survey: Emerging from the dark, a massive proto-cluster at z 4.57," *A&A*, vol. 615, p. A77, Jul. 2018.

[35] P. Madau and M. Dickinson, "Cosmic Star-Formation History," *Annual Review of Astronomy and Astrophysics*, vol. 52, pp. 415–486, Aug 2014.

[36] Y.-K. Chiang, R. A. Overzier, K. Gebhardt, and B. Henriques, "Galaxy Protoclusters as Drivers of Cosmic Star Formation History in the First 2 Gyr," *ApJL*, vol. 844, p. L23, Aug. 2017.

[37] Y.-K. Chiang, R. Overzier, and K. Gebhardt, "Ancient Light from Young Cosmic Cities: Physical and Observational Signatures of Galaxy Proto-clusters," *ApJ*, vol. 779, p. 127, Dec. 2013.

[38] C. C. Steidel, K. L. Adelberger, M. Dickinson, M. Giavalisco, M. Pettini, and M. Kellogg, "A Large Structure of Galaxies at Redshift Z approximately 3 and Its Cosmological Implications," *ApJ*, vol. 492, pp. 428–438, Jan. 1998.

[39] C. C. Steidel, K. L. Adelberger, A. E. Shapley, M. Pettini, M. Dickinson, and M. Giavalisco, "Lyα Imaging of a Proto-Cluster Region at z=3.09," *ApJ*, vol. 532, pp. 170–182, Mar. 2000.

[40] O. Cucciati, G. Zamorani, B. C. Lemaux, S. Bardelli, A. Cimatti, O. Le Fèvre, P. Cassata, B. Garilli, V. Le Brun, D. Maccagni, L. Pentericci, L. A. M. Tasca, R. Thomas, E. Vanzella, E. Zucca, R. Amorin, P. Capak, L. P. Cassarà, M. Castellano, J. G. Cuby, S. de la Torre, A. Durkalec, A. Fontana, M. Giavalisco, A. Grazian, N. P. Hathi, O. Ilbert, C. Moreau, S. Paltani, B. Ribeiro, M. Salvato, D. Schaerer, M. Scodeggio, V. Sommariva, M. Talia, Y. Taniguchi, L. Tresse, D. Vergani, P. W. Wang, S. Charlot, T. Contini, S. Fotopoulou, C. López- Sanjuan, Y. Mellier, and N. Scoville, "Discovery of a rich proto-cluster at z = 2.9 and associated diffuse cold gas in the VIMOS Ultra-Deep Survey (VUDS)," *A&A*, vol. 570, p. A16, Oct. 2014.

[41] O. Cucciati, B. C. Lemaux, G. Zamorani, O. Le Fèvre, L. A. M. Tasca, N. P. Hathi, K.-G. Lee, S. Bardelli, P. Cassata, B. Garilli, V. Le Brun, D. Maccagni, L. Pentericci, R. Thomas, E. Vanzella, E. Zucca, L. M. Lubin, R. Amorin, L. P. Cassarà, A. Cimatti, M. Talia, D. Vergani, A. Koekemoer, J. Pforr, and M. Salvato, "The progeny of a cosmic titan: a massive multi-component proto-supercluster in formation at z = 2.45 in VUDS," *A&A*, vol. 619, p. A49, Nov. 2018.

[42] L. Jiang, J. Wu, F. Bian, Y.-K. Chiang, L. C. Ho, Y. Shen, Z.-Y. Zheng, J. I. Bailey, G. A. Blanc, J. D. Crane, X. Fan, M. Mateo, E. W. Olszewski, G. A. Oyarzún, R. Wang, and X.-B. Wu, "A giant protocluster of galaxies at redshift 5.7," *Nature Astronomy*, vol. 2, pp. 962–966, Oct. 2018.

[43] J. Toshikawa, N. Kashikawa, K. Ota, T. Morokuma, T. Shibuya, M. Hayashi, T. Nagao, L. Jiang, M. A. Malkan, E. Egami, K. Shimasaku, K. Motohara, and Y. Ishizaki, "Discovery of a Protocluster at z ˜ 6," *ApJ*, vol. 750, p. 137, May 2012.

[44] R. E. Mostardi, A. E. Shapley, D. B. Nestor, C. C. Steidel, N. A. Reddy, and R. F. Trainor, "Narrowband Lyman-continuum Imaging of Galaxies at z $\sim$ 2.85," *ApJ*, vol. 779, p. 65, Dec. 2013.

[45] K.-S. Lee, A. Dey, S. Hong, N. Reddy, C. Wilson, B. T. Jannuzi, H. Inami, and A. H. Gonzalez, "Discovery of a Very Large Structure at z = 3.78," *ApJ*, vol. 796, p. 126, Dec. 2014.

[46] A. Dey, K.-S. Lee, N. Reddy, M. Cooper, H. Inami, S. Hong, A. H. Gonzalez, and B. T. Jannuzi, "Spectroscopic Confirmation of a Protocluster at z $\sim$ 3.786," *ApJ*, vol. 823, p. 11, May 2016.

[47] J. Toshikawa, N. Kashikawa, R. Overzier, M. A. Malkan, H. Furusawa, S. Ishikawa, M. Onoue, K. Ota, M. Tanaka, Y. Niino, and H. Uchiyama, "A Systematic Survey of Protoclusters at z ˜ 3-6 in the CFHTLS Deep Fields," *ApJ*, vol. 826, p. 114, Aug. 2016.

[48] A. E. Shapley, C. C. Steidel, K. L. Adelberger, M. Dickinson, M. Giavalisco, and M. Pettini, "The Rest-Frame Optical Properties of z˜=3 Galaxies," *ApJ*, vol. 562, pp. 95–123, Nov. 2001.

[49] M. Giavalisco, "Lyman-Break Galaxies," *Annual Review of Astronomy and Astrophysics*, vol. 40, pp. 579–641, 2002.

[50] E. Gawiser, H. Francke, K. Lai, K. Schawinski, C. Gronwall, R. Ciardullo, R. Quadri, A. Orsi, L. F. Barrientos, G. A. Blanc, G. Fazio, J. J. Feldmeier, J.-s. Huang, L. Infante, P. Lira, N. Padilla, E. N. Taylor, E. Treister, C. M. Urry, P. G. van Dokkum, and S. N. Virani, "Lyα-Emitting Galaxies at z = 3.1: L* Progenitors Experiencing Rapid Star Formation," *ApJ*, vol. 671, pp. 278–284, Dec. 2007.

[51] L. Guaita, V. Acquaviva, N. Padilla, E. Gawiser, N. A. Bond, R. Ciardullo, E. Treister, P. Kurczynski, C. Gronwall, P. Lira, and K. Schawinski, "Lyα-emitting Galaxies at z = 2.1: Stellar Masses, Dust, and Star Formation Histories from Spectral Energy Distribution Fitting," *ApJ*, vol. 733, p. 114, Jun. 2011.

[52] N. P. Hathi, O. Le Fèvre, O. Ilbert, P. Cassata, L. A. M. Tasca, B. C. Lemaux, B. Garilli, V. Le Brun, D. Maccagni, L. Pentericci, R. Thomas, E. Vanzella, G. Zamorani, E. Zucca, R. Amorín, S. Bardelli, L. P. Cassarà, M. Castellano, A. Cimatti, O. Cucciati, A. Durkalec, A. Fontana, M. Giavalisco, A. Grazian, L. Guaita, A. Koekemoer, S. Paltani, J. Pforr, B. Ribeiro, D. Schaerer, M. Scodeggio, V. Sommariva, M. Talia, L. Tresse, D. Vergani, P. Capak, S. Charlot, T. Contini, J. G. Cuby, S. de la Torre, J. Dunlop, S. Fotopoulou, C. López-Sanjuan, Y. Mellier, M. Salvato, N. Scoville, Y. Taniguchi, and P. W. Wang, "The VIMOS Ultra Deep Survey: Lyα emission and stellar populations of star-forming galaxies at 2 $<$ z $<$ 2.5," *A&A*, vol. 588, p. A26, Apr. 2016.

[53] R. J. McLure, J. S. Dunlop, L. de Ravel, M. Cirasuolo, R. S. Ellis, M. Schenker, B. E. Robertson, A. M. Koekemoer, D. P. Stark, and R. A. A. Bowler, "A robust sample of galaxies at redshifts 6.0<z<8.7: stellar populations, star formation rates and stellar masses," *MNRAS*, vol. 418, pp. 2074–2105, Dec. 2011.

[54] S. A. Stanford, P. R. Eisenhardt, and M. Dickinson, "The Evolution of Early Type Galaxies in Distant Clusters," *ApJ*, vol. 492, pp. 461–479, Jan. 1998.

[55] J. P. Blakeslee, M. Franx, M. Postman, P. Rosati, B. P. Holden, G. D. Illingworth, H. C. Ford, N. J. G. Cross, C. Gronwall, N. Benítez, R. J. Bouwens, T. J. Broadhurst, M. Clampin, R. Demarco, D. A. Golimowski, G. F. Hartig, L. Infante, A. R. Martel, G. K. Miley, F. Menanteau, G. R. Meurer, M. Sirianni, and R. L. White, "Advanced Camera for Surveys Photometry of the Cluster RDCS 1252.9-2927: The Color-Magnitude Relation at z = 1.24," *ApJL*, vol. 596, pp. L143–L146, Oct. 2003.

[56] D. Thomas, C. Maraston, R. Bender, and C. Mendes de Oliveira, “The Epochs of Early-Type Galaxy Formation as a Function of Environment,” *ApJ*, vol. 621, pp. 673–694, Mar. 2005.

[57] M. Bolzonella, K. Kovač, L. Pozzetti, E. Zucca, O. Cucciati, S. J. Lilly, Y. Peng, A. Iovino, G. Zamorani, D. Vergani, L. A. M. Tasca, F. Lamareille, P. Oesch, K. Caputi, P. Kampczyk, S. Bardelli, C. Maier, U. Abbas, C. Knobel, M. Scodeggio, C. M. Carollo, T. Contini, J.-P. Kneib, O. Le Fèvre, V. Mainieri, A. Renzini, A. Bongiorno, G. Coppa, S. de la Torre, L. de Ravel, P. Franzetti, B. Garilli, J.-F. Le Borgne, V. Le Brun, M. Mignoli, R. Pelló, E. Perez-Montero, E. Ricciardelli, J. D. Silverman, M. Tanaka, L. Tresse, D. Bottini, A. Cappi, P. Cassata, A. Cimatti, L. Guzzo, A. M. Koekemoer, A. Leauthaud, D. Maccagni, C. Marinoni, H. J. McCracken, P. Memeo, B. Meneux, C. Porciani, R. Scaramella, H. Aussel, P. Capak, C. Halliday, O. Ilbert, J. Kartaltepe, M. Salvato, D. Sanders, C. Scarlata, N. Scoville, Y. Taniguchi, and D. Thompson, “Tracking the impact of environment on the galaxy stellar mass function up to z ˜ 1 in the 10 k zCOSMOS sample,” *A&A*, vol. 524, p. A76, Dec. 2010.

[58] C. L. Mancone, A. H. Gonzalez, M. Brodwin, S. A. Stanford, P. R. M. Eisenhardt, D. Stern, and C. Jones, “The Formation of Massive Cluster Galaxies,” *ApJ*, vol. 720, pp. 284–298, Sep. 2010.

[59] A. Fritz, M. Scodeggio, O. Ilbert, M. Bolzonella, I. Davidzon, J. Coupon, B. Garilli, L. Guzzo, G. Zamorani, U. Abbas, C. Adami, S. Arnouts, J. Bel, D. Bottini, E. Branchini, A. Cappi, O. Cucciati, G. De Lucia, S. de la Torre, P. Franzetti, M. Fumana, B. R. Granett, A. Iovino, J. Krywult, V. Le Brun, O. Le Fèvre, D. Maccagni, K. Małek, F. Marulli, H. J. McCracken, L. Paioro, M. Polletta, A. Pollo, H. Schlagenhaufer, L. A. M. Tasca, R. Tojeiro, D. Vergani, A. Zanichelli, A. Burden, C. Di Porto, A. Marchetti, C. Marinoni, Y. Mellier, L. Moscardini, R. C. Nichol, J. A. Peacock, W. J. Percival, S. Phleps, and M. Wolk, “The VIMOS Public Extragalactic Redshift Survey (VIPERS):. A quiescent formation of massive red-sequence galaxies over the past 9 Gyr,” *A&A*, vol. 563, p. A92, Mar. 2014.

[60] G. F. Snyder, M. Brodwin, C. M. Mancone, G. R. Zeimann, S. A. Stanford, A. H. Gonzalez, D. Stern, P. R. M. Eisenhardt, M. J. I. Brown, A. Dey, B. Jannuzi, and S. Perlmutter, “Assembly of the Red Sequence in Infrared-selected Galaxy Clusters from the IRAC Shallow Cluster Survey,” *ApJ*, vol. 756, p. 114, Sep. 2012.

[61] M. Aaronson and E. W. Olszewski, “Optical counterparts of unidentified IRAS point sources Infrared luminous galaxies,” *Nature*, vol. 309, pp. 414–417, May 1984.

[62] D. B. Sanders and I. F. Mirabel, “Luminous Infrared Galaxies,” *Annual Review of Astronomy and Astrophysics*, vol. 34, p. 749, 1996.

[63] P. F. Hopkins, T. J. Cox, D. Kereš, and L. Hernquist, “A Cosmological Framework for the Co-Evolution of Quasars, Supermassive Black Holes, and Elliptical Galaxies. II. Formation of Red Ellipticals,” *ApJS*, vol. 175, pp. 390–422, Apr. 2008.

[64] R. A. Overzier, “The realm of the galaxy protoclusters. A review,” *A&A Rv*, vol. 24, p. 14, Nov. 2016.

[65] B. P. Venemans, H. J. A. Röttgering, G. K. Miley, J. D. Kurk, C. De Breuck, R. A. Overzier, W. J. M. van Breugel, C. L. Carilli, H. Ford, T. Heckman, L. Pentericci, and P. McCarthy, “Properties of Lyα emitters around the radio galaxy MRC 0316 257',” *A&A*, vol. 431, pp. 793–812, Mar. 2005.

[66] G. K. Miley, R. A. Overzier, A. W. Zirm, H. C. Ford, J. Kurk, L. Pentericci, J. P. Blakeslee, M. Franx, G. D. Illingworth, M. Postman, P. Rosati, H. J. A. Röttgering, B. P. Venemans, and E. Helder, "The Spiderweb Galaxy: A Forming Massive Cluster Galaxy at z ˜ 2," *ApJL*, vol. 650, pp. L29–L32, Oct. 2006.

[67] M. Kajisawa, T. Kodama, I. Tanaka, T. Yamada, and R. Bower, "Protoclusters with evolved populations around radio galaxies at z ˜ 2.5," *MNRAS*, vol. 371, pp. 577–582, Sep. 2006.

[68] B. P. Venemans, H. J. A. Röttgering, G. K. Miley, W. J. M. van Breugel, C. de Breuck, J. D. Kurk, L. Pentericci, S. A. Stanford, R. A. Overzier, S. Croft, and H. Ford, "Protoclusters associated with z $>$ 2 radio galaxies . I. Characteristics of high redshift protoclusters," *A&A*, vol. 461, pp. 823–845, Jan. 2007.

[69] N. A. Hatch, C. De Breuck, A. Galametz, G. K. Miley, R. A. Overzier, H. J. A. Röttgering, M. Doherty, T. Kodama, J. D. Kurk, N. Seymour, B. P. Venemans, J. Vernet, and A. W. Zirm, "Galaxy protocluster candidates around z$\sim$ 2.4 radio galaxies," *MNRAS*, vol. 410, pp. 1537–1549, Jan. 2011.

[70] G. Noirot, D. Stern, S. Mei, D. Wylezalek, E. A. Cooke, C. De Breuck, A. Galametz, N. A. Hatch, J. Vernet, M. Brodwin, P. Eisenhardt, A. H. Gonzalez, M. Jarvis, A. Rettura, N. Seymour, and S. A. Stanford, "HST Grism Confirmation of 16 Structures at 1.4$<$z$<$2.8 from the Clusters Around Radio-Loud AGN (CARLA) Survey," *ApJ*, vol. 859, p. 38, May 2018.

[71] Y. Matsuda, T. Yamada, T. Hayashino, H. Tamura, R. Yamauchi, M. Ajiki, S. S. Fujita, T. Murayama, T. Nagao, K. Ohta, S. Okamura, M. Ouchi, K. Shimasaku, Y. Shioya, and Y. Taniguchi, "A Subaru Search for Lyα Blobs in and around the Protocluster Region At Redshift z = 3.1," *AJ*, vol. 128, pp. 569–584, Aug. 2004.

[72] A. Dey, C. Bian, B. T. Soifer, K. Brand, M. J. I. Brown, F. H. Chaffee, E. Le Floc'h, G. Hill, J. R. Houck, B. T. Jannuzi, M. Rieke, D. Weedman, M. Brodwin, and P. Eisenhardt, "Discovery of a Large ˜200 kpc Gaseous Nebula at z ˜ 2.7 with the Spitzer Space Telescope," *ApJ*, vol. 629, pp. 654–666, Aug. 2005.

[73] M. K. M. Prescott, N. Kashikawa, A. Dey, and Y. Matsuda, "The Overdense Environment of a Large Lyα Nebula at z $\sim$ 2.7," *ApJL*, vol. 678, p. L77, May 2008.

[74] B. D. Lehmer, D. M. Alexander, S. C. Chapman, I. Smail, F. E. Bauer, W. N. Brandt, J. E. Geach, Y. Matsuda, J. R. Mullaney, and A. M. Swinbank, "The Chandra Deep Protocluster Survey: point-source catalogues for a 400-ks observation of the z = 3.09 protocluster in SSA22," *MNRAS*, vol. 400, pp. 299–316, Nov. 2009.

[75] P. L. Capak, D. Riechers, N. Z. Scoville, C. Carilli, P. Cox, R. Neri, B. Robertson, M. Salvato, E. Schinnerer, L. Yan, G. W. Wilson, M. Yun, F. Civano, M. Elvis, A. Karim, B. Mobasher, and J. G. Staguhn, "A massive protocluster of galaxies at a redshift of z˜5.3," *Nature*, vol. 470, pp. 233–235, Feb. 2011.

[76] C. M. Casey, "The Ubiquity of Coeval Starbursts in Massive Galaxy Cluster Progenitors," *ApJ*, vol. 824, p. 36, Jun. 2016.

[77] C.-L. Hung, C. M. Casey, Y.-K. Chiang, P. L. Capak, M. J. Cowley, B. Darvish, G. G. Kacprzak, K. Kovač, S. J. Lilly, T. Nanayakkara, L. R. Spitler, K.-V. H. Tran, and T. Yuan, "Large-scale Structure around a z=2.1 Cluster," *ApJ*, vol. 826, p. 130, Aug. 2016.

[78] Z. Cai, X. Fan, Y. Yang, F. Bian, J. X. Prochaska, A. Zabludoff, I. McGreer, Z.-Y. Zheng, R. Green, S. Cantalupo, B. Frye, E. Hamden, L. Jiang, N. Kashikawa, and R. Wang, "Discovery of an Enormous Lyα Nebula in a Massive Galaxy Overdensity at z = 2.3," *ApJ*, vol. 837, p. 71, Mar. 2017.

[79] T. Bădescu, Y. Yang, F. Bertoldi, A. Zabludoff, A. Karim, and B. Magnelli, "Discovery of a Protocluster Associated with a Lyα Blob Pair at z = 2.3," *ApJ*, vol. 845, p. 172, Aug. 2017.

[80] E. E. Rigby, N. A. Hatch, H. J. A. Röttgering, B. Sibthorpe, Y. K. Chiang, R. Overzier, R. Herbonnet, S. Borgani, D. L. Clements, H. Dannerbauer, C. De Breuck, G. De Lucia, J. Kurk, F. Maschietto, G. Miley, A. Saro, N. Seymour, and B. Venemans, "Searching for large-scale structures around high-redshift radio galaxies with Herschel," *MNRAS*, vol. 437, pp. 1882–1893, Jan. 2014.

[81] Y. Kato, Y. Matsuda, I. Smail, A. M. Swinbank, B. Hatsukade, H. Umehata, I. Tanaka, T. Saito, D. Iono, Y. Tamura, K. Kohno, D. K. Erb, B. D. Lehmer, J. E. Geach, C. C. Steidel, D. M. Alexander, T. Yamada, and T. Hayashino, "Herschel protocluster survey: a search for dusty star-forming galaxies in protoclusters at z = 2-3," *MNRAS*, vol. 460, pp. 3861–3872, Aug. 2016.

[82] M. Kubo, Y. K. Uchimoto, T. Yamada, M. Kajisawa, T. Ichikawa, Y. Matsuda, M. Akiyama, T. Hayashino, M. Konishi, T. Nishimura, K. Omata, R. Suzuki, I. Tanaka, T. Yoshikawa, D. M. Alexander, G. G. Fazio, J.-S. Huang, and B. D. Lehmer, "The Formation of the Massive Galaxies in the SSA22 z = 3.1 Protocluster," *ApJ*, vol. 778, p. 170, Dec. 2013.

[83] Planck Collaboration, N. Aghanim, B. Altieri, M. Arnaud, M. Ashdown, J. Aumont, C. Baccigalupi, A. J. Banday, R. B. Barreiro, N. Bartolo, E. Battaner, A. Beelen, K. Benabed, A. Benoit-Lévy, J.-P. Bernard, M. Bersanelli, M. Bethermin, P. Bielewicz, L. Bonavera, J. R. Bond, J. Borrill, F. R. Bouchet, F. Boulanger, C. Burigana, E. Calabrese, R. Canameras, J.-F. Cardoso, A. Catalano, A. Chamballu, R.-R. Chary, H. C. Chiang, P. R. Christensen, D. L. Clements, S. Colombi, F. Couchot, B. P. Crill, A. Curto, L. Danese, K. Dassas, R. D. Davies, R. J. Davis, P. de Bernardis, A. de Rosa, G. de Zotti, J. Delabrouille, J. M. Diego, H. Dole, S. Donzelli, O. Doré, M. Douspis, A. Ducout, X. Dupac, G. Efstathiou, F. Elsner, T. A. Enßlin, E. Falgarone, I. Flores-Cacho, O. Forni, M. Frailis, A. A. Fraisse, E. Franceschi, A. Frejsel, B. Frye, S. Galeotta, S. Galli, K. Ganga, M. Giard, E. Gjerløw, J. González-Nuevo, K. M. Górski, A. Gregorio, A. Gruppuso, D. Guéry, F. K. Hansen, D. Hanson, D. L. Harrison, G. Helou, C. Hernández-Monteagudo, S. R. Hildebrandt, E. Hivon, M. Hobson, W. A. Holmes, W. Hovest, K. M. Huffenberger, G. Hurier, A. H. Jaffe, T. R. Jaffe, E. Keihänen, R. Keskitalo, T. S. Kisner, R. Kneissl, J. Knoche, M. Kunz, H. Kurki-Suonio, G. Lagache, J.-M. Lamarre, A. Lasenby, M. Lattanzi, C. R. Lawrence, E. Le Floc'h, R. Leonardi, F. Levrier, M. Liguori, P. B. Lilje, M. Linden-Vørnle, M. López-Caniego, P. M. Lubin, J. F. Macías-Pérez, T. MacKenzie, B. Maffei, N. Mandolesi, M. Maris, P. G. Martin, C. Martinache, E. Martínez-González, S. Masi, S. Matarrese, P. Mazzotta, A. Melchiorri, A. Mennella, M. Migliaccio, A. Moneti, L. Montier, G. Morgante, D. Mortlock, D. Munshi, J. A. Murphy, P. Natoli, M. Negrello, N. P. H. Nesvadba, D. Novikov, I. Novikov, A. Omont, L. Pagano, F. Pajot, F. Pasian, O. Perdereau, L. Perotto, F. Perrotta, V. Pettorino, F. Piacentini, M. Piat, S. Plaszczynski, E. Pointecouteau, G. Polenta, L. Popa, G. W. Pratt, S. Prunet, J.-L. Puget, J. P. Rachen, W. T. Reach, M. Reinecke, M. Remazeilles, C. Renault, I. Ristorcelli, G. Rocha, G. Roudier, B. Rusholme, M. Sandri, D. Santos, G. Savini, D. Scott, L. D. Spencer, V. Stolyarov, R. Sunyaev, D. Sutton, J.-F. Sygnet, J. A. Tauber, L. Terenzi, L. Toffolatti, M. Tomasi, M. Tristram, M. Tucci, G. Umana, L. Valenziano, J. Valiviita, I. Valtchanov, B. Van Tent, J. D. Vieira, P. Vielva, L. A. Wade, B. D. Wandelt, I. K. Wehus, N. Welikala, A. Zacchei, and A. Zonca, "Planck intermediate results. XXVII. High-redshift infrared galaxy overdensity candidates and lensed sources discovered by Planck and confirmed by Herschel-SPIRE," *A&A*, vol. 582, p. A30, Oct. 2015.

[84] B. C. Lemaux, O. Le Fèvre, O. Cucciati, B. Ribeiro, L. A. M. Tasca, G. Zamorani, O. Ilbert, R. Thomas, S. Bardelli, P. Cassata, N. P. Hathi, J. Pforr, V. Smolčić, I. Delvecchio, M. Novak, S. Berta, H. J. McCracken, A. Koekemoer, R. Amorín, B. Garilli, D. Maccagni, D. Schaerer, and E. Zucca, "The VIMOS Ultra-Deep Survey: Emerging from the dark, a massive proto-cluster at z 4.57," *A&A*, vol. 615, p. A77, Jul. 2018.

[85] S. I. Muldrew, N. A. Hatch, and E. A. Cooke, "What are protoclusters? - Defining high-redshift galaxy clusters and protoclusters," *MNRAS*, vol. 452, pp. 2528–2539, Sep. 2015.

[86] Y. Matsuda, T. Yamada, T. Hayashino, H. Tamura, R. Yamauchi, T. Murayama, T. Nagao, K. Ohta, S. Okamura, M. Ouchi, K. Shimasaku, Y. Shioya, and Y. Taniguchi, "Large-Scale Filamentary Structure around the Protocluster at Redshift z = 3.1," *ApJL*, vol. 634, pp. L125–L128, Dec. 2005.

[87] N. Kashikawa, T. Kitayama, M. Doi, T. Misawa, Y. Komiyama, and K. Ota, "The Habitat Segregation between Lyman Break Galaxies and Lyα Emitters around a QSO at z ˜ 5," *ApJ*, vol. 663, pp. 765–773, Jul. 2007.

[88] T. Goto, Y. Utsumi, S. Kikuta, S. Miyazaki, K. Shiki, and T. Hashimoto, "No Ly α emitters detected around a QSO at z = 6.4: Suppressed by the QSO?," *MNRAS*, vol. 470, pp. L117–L121, Sep. 2017.

[89] Z. Cai, E. Hamden, M. Matuszewski, J. X. Prochaska, Q. Li, S. Cantalupo, F. A. Battaia, C. Martin, J. D. Neill, D. OSullivan, R. Wang, A. Moore, and P. Morrissey, "Keck/palomar cosmic web imagers reveal an enormous ly nebula in an extremely overdense quasi-stellar object pair field at z=2.45," *The Astrophysical Journal Letters*, vol. 861, no. 1, p. L3, 2018. [Online]. Available: http://stacks.iop.org/2041-8205/861/i=1/a=L3

[90] B. T. Jannuzi and A. Dey, "The NOAO Deep Wide-Field Survey," in *Photometric Redshifts and the Detection of High Redshift Galaxies*, ser. Astronomical Society of the Pacific Conference Series, R. Weymann, L. Storrie-Lombardi, M. Sawicki, and R. Brunner, Eds., vol. 191, 1999, p. 111.

[91] M. L. N. Ashby, D. Stern, M. Brodwin, R. Griffith, P. Eisenhardt, S. Kozłowski, C. S. Kochanek, J. J. Bock, C. Borys, K. Brand, M. J. I. Brown, R. Cool, A. Cooray, S. Croft, A. Dey, D. Eisenstein, A. H. Gonzalez, V. Gorjian, N. A. Grogin, R. J. Ivison, J. Jacob, B. T. Jannuzi, A. Mainzer, L. A. Moustakas, H. J. A. Röttgering, N. Seymour, H. A. Smith, S. A. Stanford, J. R. Stauffer, I. Sullivan, W. van Breugel, S. P. Willner, and E. L. Wright, "The Spitzer Deep, Wide-field Survey," *ApJ*, vol. 701, pp. 428–453, Aug. 2009.

[92] E. Komatsu, K. M. Smith, J. Dunkley, C. L. Bennett, B. Gold, G. Hinshaw, N. Jarosik, D. Larson, M. R. Nolta, L. Page, D. N. Spergel, M. Halpern, R. S. Hill, A. Kogut, M. Limon, S. S. Meyer, N. Odegard, G. S. Tucker, J. L. Weiland, E. Wollack, and E. L. Wright, "Seven-year Wilkinson Microwave Anisotropy Probe (WMAP) Observations: Cosmological Interpretation," *ApJS*, vol. 192, p. 18, Feb. 2011.

[93] J. B. Oke and J. E. Gunn, "Secondary standard stars for absolute spectrophotometry," *ApJ*, vol. 266, pp. 713–717, Mar. 1983.

[94] G. H. Jacoby, M. Liang, D. Vaughnn, R. Reed, and T. Armandroff, "New wide-field corrector for the Kitt Peak Mayall 4-m telescope," in *Optical Astronomical Instrumentation*, ser. Proc. SPIE, S. D'Odorico, Ed., vol. 3355, Jul. 1998, pp. 721–734.

[95] A. Dey, D. Rabinowitz, A. Karcher, C. Bebek, C. Baltay, D. Sprayberry, F. Valdes, B. Stupak, J. Donaldson, W. Emmet, T. Hurteau, B. Abareshi, B. Marshall, D. Lang, M. Fitzpatrick, P. Daly, D. Joyce, D. Schlegel, H. Schweiker, L. Allen, B. Blum, and M. Levi, "Mosaic3: a red-sensitive upgrade for the prime focus camera at the Mayall 4m telescope," in *Ground-based and Airborne Instrumentation for Astronomy VI*, ser. Proc. SPIE, vol. 9908, Aug. 2016, p. 99082C.

[96] S. Miyazaki, Y. Komiyama, S. Kawanomoto, Y. Doi, H. Furusawa, T. Hamana, Y. Hayashi, H. Ikeda, Y. Kamata, H. Karoji, M. Koike, T. Kurakami, S. Miyama, T. Morokuma, F. Nakata, K. Namikawa, H. Nakaya, K. Nariai, Y. Obuchi, Y. Oishi, N. Okada, Y. Okura, P. Tait, T. Takata, Y. Tanaka, M. Tanaka, T. Terai, D. Tomono, F. Uraguchi, T. Usuda, Y. Utsumi, Y. Yamada, H. Yamanoi, H. Aihara, H. Fujimori, S. Mineo, H. Miyatake, M. Oguri, T. Uchida, M. M. Tanaka, N. Yasuda, M. Takada, H. Murayama, A. J. Nishizawa, N. Sugiyama, M. Chiba, T. Futamase, S.-Y. Wang, H.-Y. Chen, P. T. P. Ho, E. J. Y. Liaw, C.-F. Chiu, C.-L. Ho, T.-C. Lai, Y.-C. Lee, D.-Z. Jeng, S. Iwamura, R. Armstrong, S. Bickerton, J. Bosch, J. E. Gunn, R. H. Lupton, C. Loomis, P. Price, S. Smith, M. A. Strauss, E. L. Turner, H. Suzuki, Y. Miyazaki, M. Muramatsu, K. Yamamoto, M. Endo, Y. Ezaki, N. Ito, N. Kawaguchi, S. Sofuku, T. Taniike, K. Akutsu, N. Dojo, K. Kasumi, T. Matsuda, K. Imoto, Y. Miwa, M. Suzuki, K. Takeshi, and H. Yokota, "Hyper Suprime-Cam: System design and verification of image quality," *PASJ*, vol. 70, p. S1, Jan. 2018.

[97] J. Bosch, R. Armstrong, S. Bickerton, H. Furusawa, H. Ikeda, M. Koike, R. Lupton, S. Mineo, P. Price, T. Takata, M. Tanaka, N. Yasuda, Y. AlSayyad, A. C. Becker, W. Coulton, J. Coupon, J. Garmilla, S. Huang, K. S. Krughoff, D. Lang, A. Leauthaud, K.-T. Lim, N. B. Lust, L. A. MacArthur, R. Mandelbaum, H. Miyatake, S. Miyazaki, R. Murata, S. More, Y. Okura, R. Owen, J. D. Swinbank, M. A. Strauss, Y. Yamada, and H. Yamanoi, "The Hyper Suprime-Cam software pipeline," *PASJ*, vol. 70, p. S5, Jan. 2018.

[98] K. C. Chambers, E. A. Magnier, N. Metcalfe, H. A. Flewelling, M. E. Huber, C. Z. Waters, L. Denneau, P. W. Draper, D. Farrow, D. P. Finkbeiner, C. Holmberg, J. Koppenhoefer, P. A. Price, R. P. Saglia, E. F. Schlafly, S. J. Smartt, W. Sweeney, R. J. Wainscoat, W. S. Burgett, T. Grav, J. N. Heasley, K. W. Hodapp, R. Jedicke, N. Kaiser, R.-P. Kudritzki, G. A. Luppino, R. H. Lupton, D. G. Monet, J. S. Morgan, P. M. Onaka, C. W. Stubbs, J. L. Tonry, E. Banados, E. F. Bell, R. Bender, E. J. Bernard, M. T. Botticella, S. Casertano, S. Chastel, W.-P. Chen, X. Chen, S. Cole, N. Deacon, C. Frenk, A. Fitzsimmons, S. Gezari, C. Goessl, T. Goggia, B. Goldman, E. K. Grebel, N. C. Hambly, G. Hasinger, A. F. Heavens, T. M. Heckman, R. Henderson, T. Henning, M. Holman, U. Hopp, W.-H. Ip, S. Isani, C. D. Keyes, A. Koekemoer, R. Kotak, K. S. Long, J. R. Lucey, M. Liu, N. F. Martin, B. McLean, E. Morganson, D. N. A. Murphy, M. A. Nieto-Santisteban, P. Norberg, J. A. Peacock, E. A. Pier, M. Postman, N. Primak, C. Rae, A. Rest, A. Riess, A. Riffeser, H. W. Rix, S. Roser, E. Schilbach, A. S. B. Schultz, D. Scolnic, A. Szalay, S. Seitz, B. Shiao, E. Small, K. W. Smith, D. Soderblom, A. N. Taylor, A. R. Thakar, J. Thiel, D. Thilker, Y. Urata, J. Valenti, F. Walter, S. P. Watters, S. Werner, R. White, W. M. Wood-Vasey, and R. Wyse, "The Pan-STARRS1 Surveys," *ArXiv e-prints*, Dec. 2016.

[99] R. G. Autry, R. G. Probst, B. M. Starr, K. M. Abdel-Gawad, R. D. Blakley, P. N. Daly, R. Dominguez, E. A. Hileman, M. Liang, E. T. Pearson, R. A. Shaw, and D. Tody, "NEWFIRM: the widefield IR imager for NOAO 4-m telescopes," in *Instrument Design and Performance for Optical/Infrared Ground-based Telescopes*, ser. Proc. SPIE, M. Iye and A. F. M. Moorwood, Eds., vol. 4841, Mar. 2003, pp. 525–539.

[100] R. G. Probst, J. R. George, P. N. Daly, K. Don, and M. Ellis, "First light with NEWFIRM," in *Ground-based and Airborne Instrumentation for Astronomy II*, ser. Proc. SPIE, vol. 7014, Jul. 2008, p. 70142S.

[101] E. Bertin, "Automated Morphometry with SExtractor and PSFEx," in *Astronomical Data Analysis Software and Systems XX*, ser. Astronomical Society of the Pacific Conference Series, I. N. Evans, A. Accomazzi, D. J. Mink, and A. H. Rots, Eds., vol. 442, Jul. 2011, p. 435.

[102] R. Xue, K.-S. Lee, A. Dey, N. Reddy, S. Hong, M. K. M. Prescott, H. Inami, B. T. Jannuzi, and A. H. Gonzalez, "The Diversity of Diffuse Lyα Nebulae around Star-forming Galaxies at High Redshift," *ApJ*, vol. 837, p. 172, Mar. 2017.

[103] E. Bertin and S. Arnouts, "Sextractor: Software for source extraction." *A&AS*, vol. 117, p. 393, Jun. 1996.

[104] E. Merlin, A. Fontana, H. C. Ferguson, J. S. Dunlop, D. Elbaz, N. Bourne, V. A. Bruce, F. Buitrago, M. Castellano, C. Schreiber, A. Grazian, R. J. McLure, K. Okumura, X. Shu, T. Wang, R. Amorín, K. Boutsia, N. Cappelluti, A. Comastri, S. Derriere, S. M. Faber, and P. Santini, "T-PHOT: A new code for PSF-matched, prior-based, multiwavelength extragalactic deconfusion photometry," *A&A*, vol. 582, p. A15, Oct. 2015.

[105] V. G. Laidler, C. Papovich, N. A. Grogin, R. Idzi, M. Dickinson, H. C. Ferguson, B. Hilbert, K. Clubb, and S. Ravindranath, "TFIT: A Photometry Package Using Prior Information for Mixed-Resolution Data Sets," *PASP*, vol. 119, pp. 1325–1344, Nov. 2007.

[106] K.-S. Lee, H. C. Ferguson, T. Wiklind, T. Dahlen, M. E. Dickinson, M. Giavalisco, N. Grogin, C. Papovich, H. Messias, Y. Guo, and L. Lin, "How Do Star-forming Galaxies at z $>$ 3 Assemble Their Masses?" *ApJ*, vol. 752, p. 66, Jun. 2012.

[107] S. Noll, D. Burgarella, E. Giovannoli, V. Buat, D. Marcillac, and J. C. Muñoz-Mateos, "Analysis of galaxy spectral energy distributions from far-UV to far-IR with CIGALE: studying a SINGS test sample," *A&A*, vol. 507, pp. 1793–1813, Dec. 2009.

[108] K.-S. Lee, A. Dey, M. C. Cooper, N. Reddy, and B. T. Jannuzi, "Probing High-redshift Galaxy Formation at the Highest Luminosities: New Insights from DEIMOS Spectroscopy," *ApJ*, vol. 771, p. 25, Jul. 2013.

[109] G. Bruzual and S. Charlot, "Stellar population synthesis at the resolution of 2003," *MNRAS*, vol. 344, pp. 1000–1028, Oct. 2003.

[110] D. Calzetti, L. Armus, R. C. Bohlin, A. L. Kinney, J. Koornneef, and T. Storchi-Bergmann, "The Dust Content and Opacity of Actively Star-forming Galaxies," *ApJ*, vol. 533, pp. 682–695, Apr. 2000.

[111] E. E. Salpeter, "The Luminosity Function and Stellar Evolution." *ApJ*, vol. 121, p. 161, Jan. 1955.

[112] M. Franx, I. Labbé, G. Rudnick, P. G. van Dokkum, E. Daddi, N. M. Förster Schreiber, A. Moorwood, H.-W. Rix, H. Röttgering, A. van der Wel, P. van der Werf, and L. van Starkenburg, "A Significant Population of Red, Near-Infrared-selected High-Redshift Galaxies," *ApJL*, vol. 587, pp. L79–L82, Apr. 2003.

[113] I. Labbé, J. Huang, M. Franx, G. Rudnick, P. Barmby, E. Daddi, P. G. van Dokkum, G. G. Fazio, N. M. F. Schreiber, A. F. M. Moorwood, H.-W. Rix, H. Röttgering, I. Trujillo, and P. van der Werf, "IRAC Mid-Infrared Imaging of the Hubble Deep Field-South: Star Formation Histories and Stellar Masses of Red Galaxies at z$>$2," *ApJL*, vol. 624, pp. L81–L84, May 2005.

[114] G. B. Brammer and P. G. van Dokkum, "The Density and Spectral Energy Distributions of Red Galaxies at z ˜ 3.7," *ApJL*, vol. 654, pp. L107–L110, Jan. 2007.

[115] T. Wiklind, M. Dickinson, H. C. Ferguson, M. Giavalisco, B. Mobasher, N. A. Grogin, and N. Panagia, "A Population of Massive and Evolved Galaxies at z>˜5," *ApJ*, vol. 676, pp. 781–806, Apr. 2008.

[116] J.-S. Huang, X. Z. Zheng, D. Rigopoulou, G. Magdis, G. G. Fazio, and T. Wang, "Four IRAC Sources with an Extremely Red H - [3.6] Color: Passive or Dusty Galaxies at z > 4.5?" *ApJL*, vol. 742, p. L13, Nov. 2011.

[117] H. Nayyeri, B. Mobasher, S. Hemmati, S. De Barros, H. C. Ferguson, T. Wiklind, T. Dahlen, M. Dickinson, M. Giavalisco, A. Fontana, M. Ashby, G. Barro, Y. Guo, N. P. Hathi, S. Kassin, A. Koekemoer, S. Willner, J. S. Dunlop, D. Paris, and T. A. Targett, "A Study of Massive and Evolved Galaxies at High Redshift," *ApJ*, vol. 794, p. 68, Oct. 2014.

[118] K. Mawatari, T. Yamada, G. G. Fazio, J.-S. Huang, and M. L. N. Ashby, "Possible identification of massive and evolved galaxies at z > 5," *PASJ*, vol. 68, p. 46, Jun. 2016.

[119] C. L. Mancone and A. H. Gonzalez, "EzGal: A Flexible Interface for Stellar Population Synthesis Models," *Publications of the Astronomical Society of the Pacific*, vol. 124, p. 606, Jun. 2012.

[120] M. Vaccari, "The Spitzer Data Fusion: Contents, Construction and Applications to Galaxy Evolution Studies," in *The Many Facets of Extragalactic Radio Surveys: Towards New Scientific Challenges*, Oct. 2015, p. 27.

[121] D. Stern, P. Eisenhardt, V. Gorjian, C. S. Kochanek, N. Caldwell, D. Eisenstein, M. Brodwin, M. J. I. Brown, R. Cool, A. Dey, P. Green, B. T. Jannuzi, S. S. Murray, M. A. Pahre, and S. P. Willner, "Mid-Infrared Selection of Active Galaxies," *ApJ*, vol. 631, pp. 163–168, Sep. 2005.

[122] J. L. Donley, A. M. Koekemoer, M. Brusa, P. Capak, C. N. Cardamone, F. Civano, O. Ilbert, C. D. Impey, J. S. Kartaltepe, T. Miyaji, M. Salvato, D. B. Sanders, J. R. Trump, and G. Zamorani, "Identifying Luminous Active Galactic Nuclei in Deep Surveys: Revised IRAC Selection Criteria," *ApJ*, vol. 748, p. 142, Apr. 2012.

[123] K.-S. Lee, A. Dey, N. Reddy, M. J. I. Brown, A. H. Gonzalez, B. T. Jannuzi, M. C. Cooper, X. Fan, F. Bian, E. Glikman, D. Stern, M. Brodwin, and A. Cooray, "The Average Physical Properties and Star Formation Histories of the UV-brightest Star-forming Galaxies at z ˜ 3.7," *ApJ*, vol. 733, pp. 99–+, Jun. 2011.

[124] A. Sajina, L. Yan, D. Fadda, K. Dasyra, and M. Huynh, "Spitzer- and Herschel-based Spectral Energy Distributions of 24 μm Bright z ˜ 0.3-3.0 Starbursts and Obscured Quasars," *ApJ*, vol. 757, p. 13, Sep. 2012.

[125] A. Kirkpatrick, A. Pope, A. Sajina, E. Roebuck, L. Yan, L. Armus, T. Díaz-Santos, and S. Stierwalt, "The Role of Star Formation and an AGN in Dust Heating of z = 0.3-2.8 Galaxies. I. Evolution with Redshift and Luminosity," *ApJ*, vol. 814, p. 9, Nov. 2015.

[126] D. Marchesini, K. E. Whitaker, G. Brammer, P. G. van Dokkum, I. Labbé, A. Muzzin, R. F. Quadri, M. Kriek, K.-S. Lee, G. Rudnick, M. Franx, G. D. Illingworth, and D. Wake, "The Most Massive Galaxies at $3.0 <= z < 4.0$ in the Newfirm Medium-band Survey: Properties and Improved Constraints on the Stellar Mass Function," *ApJ*, vol. 725, pp. 1277–1295, Dec. 2010.

[127] K. Glazebrook, C. Schreiber, I. Labbé, T. Nanayakkara, G. G. Kacprzak, P. A. Oesch, C. Papovich, L. R. Spitler, C. M. S. Straatman, K.-V. H. Tran, and T. Yuan, "A massive, quiescent galaxy at a redshift of 3.717," *Nature*, vol. 544, pp. 71–74, Apr. 2017.

[128] J. S. Dunlop, M. Cirasuolo, and R. J. McLure, "A systematic search for very massive galaxies at $z > 4$," *MNRAS*, vol. 376, pp. 1054–1064, Apr. 2007.

[129] B. Mobasher, M. Dickinson, H. C. Ferguson, M. Giavalisco, T. Wiklind, D. Stark, R. S. Ellis, S. M. Fall, N. A. Grogin, L. A. Moustakas, N. Panagia, M. Sosey, M. Stiavelli, E. Bergeron, S. Casertano, P. Ingraham, A. Koekemoer, I. Labbé, M. Livio, B. Rodgers, C. Scarlata, J. Vernet, A. Renzini, P. Rosati, H. Kuntschner, M. Kümmel, J. R. Walsh, R. Chary, P. Eisenhardt, N. Pirzkal, and D. Stern, "Evidence for a Massive Poststarburst Galaxy at z~6.5," *ApJ*, vol. 635, pp. 832–844, Dec. 2005.

[130] R.-R. Chary, H. I. Teplitz, M. E. Dickinson, D. C. Koo, E. Le Floc'h, D. Marcillac, C. Papovich, and D. Stern, "Hubble Ultra Deep Field-JD2: Mid-Infrared Evidence for a z ~ 2 Luminous Infrared Galaxy," *ApJ*, vol. 665, pp. 257–264, Aug. 2007.

[131] M. Sawicki, "The 1.6 Micron Bump as a Photometric Redshift Indicator," *AJ*, vol. 124, pp. 3050–3060, Dec. 2002.

[132] C. Mancini, I. Matute, A. Cimatti, E. Daddi, M. Dickinson, G. Rodighiero, M. Bolzonella, and L. Pozzetti, "Searching for massive galaxies at $z > 3.5$ in GOODS-North," *A&A*, vol. 500, pp. 705–723, Jun. 2009.

[133] Z. C. Marsan, D. Marchesini, G. B. Brammer, M. Stefanon, A. Muzzin, A. Fernández-Soto, S. Geier, K. N. Hainline, H. Intema, A. Karim, I. Labbé, S. Toft, and P. G. van Dokkum, "Spectroscopic Confirmation of an Ultra Massive and Compact Galaxy at $z = 3.35$: a Detailed Look at an Early Progenitor of Local Giant Ellipticals," *ApJ*, vol. 801, p. 133, Mar. 2015.

[134] M. Kriek, P. G. van Dokkum, I. Labbé, M. Franx, G. D. Illingworth, D. Marchesini, and R. F. Quadri, "An Ultra-Deep Near-Infrared Spectrum of a Compact Quiescent Galaxy at $z = 2.2$," *ApJ*, vol. 700, pp. 221–231, Jul. 2009.

[135] H. Shim, R.-R. Chary, M. Dickinson, L. Lin, H. Spinrad, D. Stern, and C.-H. Yan, "z ~ 4 Hα Emitters in the Great Observatories Origins Deep Survey: Tracing the Dominant Mode for Growth of Galaxies," *ApJ*, vol. 738, p. 69, Sep. 2011.

[136] D. P. Stark, M. A. Schenker, R. Ellis, B. Robertson, R. McLure, and J. Dunlop, "Keck Spectroscopy of $3 < z < 7$ Faint Lyman Break Galaxies: The Importance of Nebular Emission in Understanding the Specific Star Formation Rate and Stellar Mass Density," *ApJ*, vol. 763, p. 129, Feb. 2013.

[137] M. A. Schenker, R. S. Ellis, N. P. Konidaris, and D. P. Stark, "Contamination of Broadband Photometry by Nebular Emission in High-redshift Galaxies: Investigations with Keck's MOSFIRE Near-infrared Spectrograph," *ApJ*, vol. 777, p. 67, Nov. 2013.

[138] B. P. Holden, P. A. Oesch, V. G. González, G. D. Illingworth, I. Labbé, R. Bouwens, M. Franx, P. van Dokkum, and L. Spitler, "Rest-frame Optical Emission Lines in z $\sim$ 3.5 Lyman-break-selected Galaxies: The Ubiquity of Unusually High [OIII]/Hβ Ratios at 2 Gyr," *ApJ*, vol. 820, p. 73, Mar. 2016.

[139] M. A. Malkan, D. P. Cohen, M. Maruyama, N. Kashikawa, C. Ly, S. Ishikawa, K. Shimasaku, M. Hayashi, and K. Motohara, "Lyman-break Galaxies at z $\sim$ 3 in the Subaru Deep Field: Luminosity Function, Clustering, and [O III] Emission," *ApJ*, vol. 850, p. 5, Nov. 2017.

[140] D. P. Stark, R. S. Ellis, A. Bunker, K. Bundy, T. Targett, A. Benson, and M. Lacy, "The Evolutionary History of Lyman Break Galaxies Between Redshift 4 and 6: Observing Successive Generations of Massive Galaxies in Formation," *ApJ*, vol. 697, pp. 1493–1511, Jun. 2009.

[141] B. Salmon, C. Papovich, S. L. Finkelstein, V. Tilvi, K. Finlator, P. Behroozi, T. Dahlen, R. Davé, A. Dekel, M. Dickinson, H. C. Ferguson, M. Giavalisco, J. Long, Y. Lu, B. Mobasher, N. Reddy, R. S. Somerville, and R. H. Wechsler, "The Relation between Star Formation Rate and Stellar Mass for Galaxies at 3.5 <= z <= 6.5 in CANDELS," *ApJ*, vol. 799, p. 183, Feb. 2015.

[142] J. Kalirai, "Scientific discovery with the James Webb Space Telescope," *Contemporary Physics*, vol. 59, pp. 251–290, Jul. 2018.

[143] J. A. Peacock, "Two-dimensional goodness-of-fit testing in astronomy," *MNRAS*, vol. 202, pp. 615–627, Feb. 1983.

[144] G. Fasano and A. Franceschini, "A multidimensional version of the Kolmogorov-Smirnov test," *MNRAS*, vol. 225, pp. 155–170, Mar. 1987.

[145] E. Kuiper, B. P. Venemans, N. A. Hatch, G. K. Miley, and H. J. A. Rttgering, "A z 3 radio galaxy and its protocluster: evidence for a superstructure?" *Monthly Notices of the Royal Astronomical Society*, vol. 425, no. 2, pp. 801–813, 2012. [Online]. Available: http://dx.doi.org/10.1111/j.1365-2966.2012.20800.x

[146] K.-S. Lee, A. Dey, T. Matheson, K. Shi, C.-L. Hung, R. Xue, H. Inami, Y. Huang, K.-G. Lee, M. L. N. Ashby, B. Jannuzi, N. Reddy, S. Hong, W. Mo, and N. Malavasi, "Discovery of a Very Large ($\sim$20 kpc) Galaxy at z=3.72," *ApJ*, vol. 862, p. 24, Jul. 2018.

[147] C. Diener, S. J. Lilly, C. Ledoux, G. Zamorani, M. Bolzonella, D. N. A. Murphy, P. Capak, O. Ilbert, and H. McCracken, "A Protocluster at z = 2.45," *ApJ*, vol. 802, p. 31, Mar. 2015.

[148] Y.-K. Chiang, R. A. Overzier, K. Gebhardt, S. L. Finkelstein, C.-T. Chiang, G. J. Hill, G. A. Blanc, N. Drory, T. S. Chonis, G. R. Zeimann, A. Hagen, D. P. Schneider, S. Jogee, R. Ciardullo, and C. Gronwall, "Surveying Galaxy Proto-clusters in Emission: A Large-scale Structure at z = 2.44 and the Outlook for HETDEX," *ApJ*, vol. 808, p. 37, Jul. 2015.

[149] T. Wang, D. Elbaz, E. Daddi, A. Finoguenov, D. Liu, C. Schreiber, S. Martín, V. Strazzullo, F. Valentino, R. van der Burg, A. Zanella, L. Ciesla, R. Gobat, A. Le Brun, M. Pannella, M. Sargent, X. Shu, Q. Tan, N. Cappelluti, and Y. Li, "Discovery of a Galaxy Cluster with a Violently Starbursting Core at z = 2.506," *ApJ*, vol. 828, p. 56, Sep. 2016.

[150] M. Kubo, T. Yamada, T. Ichikawa, M. Kajisawa, Y. Matsuda, and I. Tanaka, "NIR Spectroscopic Observation of Massive Galaxies in the Protocluster at z = 3.09," *ApJ*, vol. 799, p. 38, Jan. 2015.

[151] O. Le Fèvre, L. A. M. Tasca, P. Cassata, B. Garilli, V. Le Brun, D. Maccagni, L. Pentericci, R. Thomas, E. Vanzella, G. Zamorani, E. Zucca, R. Amorin, S. Bardelli, P. Capak, L. Cassarà, M. Castellano, A. Cimatti, J. G. Cuby, O. Cucciati, S. de la Torre, A. Durkalec, A. Fontana, M. Giavalisco, A. Grazian, N. P. Hathi, O. Ilbert, B. C. Lemaux, C. Moreau, S. Paltani, B. Ribeiro, M. Salvato, D. Schaerer, M. Scodeggio, V. Sommariva, M. Talia, Y. Taniguchi, L. Tresse, D. Vergani, P. W. Wang, S. Charlot, T. Contini, S. Fotopoulou, C. López-Sanjuan, Y. Mellier, and N. Scoville, "The VIMOS Ultra-Deep Survey: ˜10 000 galaxies with spectroscopic redshifts to study galaxy assembly at early epochs 2 ¡ z $\sim$ 6," *A&A*, vol. 576, p. A79, Apr. 2015.

[152] T. Hayashino, Y. Matsuda, H. Tamura, R. Yamauchi, T. Yamada, M. Ajiki, S. S. Fujita, T. Murayama, T. Nagao, K. Ohta, S. Okamura, M. Ouchi, K. Shimasaku, Y. Shioya, and Y. Taniguchi, "Large-Scale Structure of Emission-Line Galaxies at z=3.1," *AJ*, vol. 128, pp. 2073–2079, Nov. 2004.

[153] T. Yamada, Y. Matsuda, K. Kousai, T. Hayashino, N. Morimoto, and M. Umemura, "Profiles of Lyα Emission Lines of the Emitters at z = 3.1," *ApJ*, vol. 751, p. 29, May 2012.

[154] M. W. Topping, A. E. Shapley, C. C. Steidel, S. Naoz, and J. R. Primack, "Understanding Large-scale Structure in the SSA22 Protocluster Region Using Cosmological Simulations," *ApJ*, vol. 852, p. 134, Jan. 2018.

[155] M. Ouchi, K. Shimasaku, S. Okamura, H. Furusawa, N. Kashikawa, K. Ota, M. Doi, M. Hamabe, M. Kimura, Y. Komiyama, M. Miyazaki, S. Miyazaki, F. Nakata, M. Sekiguchi, M. Yagi, and N. Yasuda, "Subaru Deep Survey. VI. A Census of Lyman Break Galaxies at z˜=4 and 5 in the Subaru Deep Fields: Clustering Properties," *ApJ*, vol. 611, pp. 685–702, Aug. 2004.

[156] K.-S. Lee, M. Giavalisco, O. Y. Gnedin, R. S. Somerville, H. C. Ferguson, M. Dickinson, and M. Ouchi, "The Large-Scale and Small-Scale Clustering of Lyman Break Galaxies at 3.5¡=z¡=5.5 from the GOODS Survey," *ApJ*, vol. 642, pp. 63–80, May 2006.

[157] H. Hildebrandt, J. Pielorz, T. Erben, L. van Waerbeke, P. Simon, and P. Capak, "CARS: the CFHTLS-Archive-Research Survey. II. Weighing dark matter halos of Lyman-break galaxies at z = 3-5," *A&A*, vol. 498, pp. 725–736, May 2009.

[158] A. Muzzin, D. Marchesini, M. Stefanon, M. Franx, H. J. McCracken, B. Milvang-Jensen, J. S. Dunlop, J. P. U. Fynbo, G. Brammer, I. Labbé, and P. G. van Dokkum, "The Evolution of the Stellar Mass Functions of Star-forming and Quiescent Galaxies to z = 4 from the COSMOS/UltraVISTA Survey," *ApJ*, vol. 777, p. 18, Nov. 2013.

[159] L. R. Spitler, C. M. S. Straatman, I. Labbé, K. Glazebrook, K.-V. H. Tran, G. G. Kacprzak, R. F. Quadri, C. Papovich, S. E. Persson, P. van Dokkum, R. Allen, L. Kawinwanichakij, D. D. Kelson, P. J. McCarthy, N. Mehrtens, A. J. Monson, T. Nanayakkara, G. Rees, V. Tilvi, and A. R. Tomczak, "Exploring the z = 3-4 Massive Galaxy Population with ZFOURGE: The Prevalence of Dusty and Quiescent Galaxies," *ApJL*, vol. 787, p. L36, Jun. 2014.

[160] T. Kodama, I. Tanaka, M. Kajisawa, J. Kurk, B. Venemans, C. De Breuck, J. Vernet, and C. Lidman, "The first appearance of the red sequence of galaxies in proto-clusters at 2 <˜ z <˜ 3," *MNRAS*, vol. 377, pp. 1717–1725, Jun. 2007.

[161] S. Mei, B. P. Holden, J. P. Blakeslee, P. Rosati, M. Postman, M. J. Jee, A. Rettura, M. Sirianni, R. Demarco, H. C. Ford, M. Franx, N. Homeier, and G. D. Illingworth, "Evolution of the Color-Magnitude Relation in High-Redshift Clusters: Early-Type Galaxies in the Lynx Supercluster at z ˜ 1.26," *ApJ*, vol. 644, pp. 759–768, Jun. 2006.

[162] Y.-j. Peng, S. J. Lilly, K. Kovač, M. Bolzonella, L. Pozzetti, A. Renzini, G. Zamorani, O. Ilbert, C. Knobel, A. Iovino, C. Maier, O. Cucciati, L. Tasca, C. M. Carollo, J. Silverman, P. Kampczyk, L. de Ravel, D. Sanders, N. Scoville, T. Contini, V. Mainieri, M. Scodeggio, J.-P. Kneib, O. Le Fèvre, S. Bardelli, A. Bongiorno, K. Caputi, G. Coppa, S. de la Torre, P. Franzetti, B. Garilli, F. Lamareille, J.-F. Le Borgne, V. Le Brun, M. Mignoli, E. Perez Montero, R. Pello, E. Ricciardelli, M. Tanaka, L. Tresse, D. Vergani, N. Welikala, E. Zucca, P. Oesch, U. Abbas, L. Barnes, R. Bordoloi, D. Bottini, A. Cappi, P. Cassata, A. Cimatti, M. Fumana, G. Hasinger, A. Koekemoer, A. Leauthaud, D. Maccagni, C. Marinoni, H. McCracken, P. Memeo, B. Meneux, P. Nair, C. Porciani, V. Presotto, and R. Scaramella, "Mass and Environment as Drivers of Galaxy Evolution in SDSS and zCOSMOS and the Origin of the Schechter Function," *ApJ*, vol. 721, pp. 193–221, Sep. 2010.

[163] M. Brodwin, S. A. Stanford, A. H. Gonzalez, G. R. Zeimann, G. F. Snyder, C. L. Mancone, A. Pope, P. R. Eisenhardt, D. Stern, S. Alberts, M. L. N. Ashby, M. J. I. Brown, R.-R. Chary, A. Dey, A. Galametz, D. P. Gettings, B. T. Jannuzi, E. D. Miller, J. Moustakas, and L. A. Moustakas, "The Era of Star Formation in Galaxy Clusters," *ApJ*, vol. 779, p. 138, Dec. 2013.

[164] M. Kubo, T. Yamada, T. Ichikawa, M. Kajisawa, Y. Matsuda, I. Tanaka, and H. Umehata, "An extremely dense group of massive galaxies at the centre of the protocluster at z = 3.09 in the SSA22 field," *MNRAS*, vol. 455, pp. 3333–3344, Jan. 2016.

[165] R. Smit, R. J. Bouwens, M. Franx, G. D. Illingworth, I. Labbé, P. A. Oesch, and P. G. van Dokkum, "The Star Formation Rate Function for Redshift z ˜ 4-7 Galaxies: Evidence for a Uniform Buildup of Star-forming Galaxies during the First 3 Gyr of Cosmic Time," *ApJ*, vol. 756, p. 14, Sep. 2012.

[166] M. Giavalisco and M. Dickinson, "Clustering Segregation with Ultraviolet Luminosity in Lyman Break Galaxies at z˜3 and Its Implications," *ApJ*, vol. 550, pp. 177–194, Mar. 2001.

[167] K. L. Adelberger, C. C. Steidel, M. Pettini, A. E. Shapley, N. A. Reddy, and D. K. Erb, "The Spatial Clustering of Star-forming Galaxies at Redshifts 1.4 ¡˜ z ¡˜ 3.5," *ApJ*, vol. 619, pp. 697–713, Feb. 2005.

[168] L. Guaita, E. Gawiser, N. Padilla, H. Francke, N. A. Bond, C. Gronwall, R. Ciardullo, J. J. Feldmeier, S. Sinawa, G. A. Blanc, and S. Virani, "Lyα-emitting Galaxies at z = 2.1 in ECDF-S: Building Blocks of Typical Present-day Galaxies?" *ApJ*, vol. 714, pp. 255–269, May 2010.

[169] H. Kusakabe, K. Shimasaku, R. Momose, M. Ouchi, K. Nakajima, T. Hashimoto, Y. Harikane, J. D. Silverman, and P. L. Capak, "The dominant origin of diffuse Lyα halos around LAEs explored by SED fitting and clustering analysis," *ArXiv e-prints*, Mar. 2018.

[170] R. J. Bouwens, G. D. Illingworth, M. Franx, and H. Ford, "UV Luminosity Functions at z˜4, 5, and 6 from the Hubble Ultra Deep Field and Other Deep Hubble Space Telescope ACS Fields: Evolution and Star Formation History," *ApJ*, vol. 670, pp. 928–958, Dec. 2007.

[171] N. A. Reddy and C. C. Steidel, "A Steep Faint-End Slope of the UV Luminosity Function at z ˜ 2-3: Implications for the Global Stellar Mass Density and Star Formation in Low-Mass Halos," *ApJ*, vol. 692, pp. 778–803, Feb. 2009.

[172] A. Alavi, B. Siana, J. Richard, M. Rafelski, M. Jauzac, M. Limousin, W. R. Freeman, C. Scarlata, B. Robertson, D. P. Stark, H. I. Teplitz, and V. Desai, "The Evolution of the Faint End of the UV Luminosity Function during the Peak Epoch of Star Formation ($1 < z < 3$)," *ApJ*, vol. 832, p. 56, Nov. 2016.

[173] H. Umehata, Y. Tamura, K. Kohno, B. Hatsukade, K. S. Scott, M. Kubo, T. Yamada, R. J. Ivison, R. Cybulski, I. Aretxaga, J. Austermann, D. H. Hughes, H. Ezawa, T. Hayashino, S. Ikarashi, D. Iono, R. Kawabe, Y. Matsuda, H. Matsuo, K. Nakanishi, T. Oshima, T. Perera, T. Takata, G. W. Wilson, and M. S. Yun, "AzTEC/ASTE 1.1-mm survey of SSA22: Counterpart identification and photometric redshift survey of submillimetre galaxies," *MNRAS*, vol. 440, pp. 3462–3478, Jun. 2014.

[174] J. Toshikawa, H. Uchiyama, N. Kashikawa, M. Ouchi, R. Overzier, Y. Ono, Y. Harikane, S. Ishikawa, T. Kodama, Y. Matsuda, Y.-T. Lin, M. Onoue, M. Tanaka, T. Nagao, M. Akiyama, Y. Komiyama, T. Goto, and C.-H. Lee, "GOLDRUSH. III. A systematic search for protoclusters at $z \sim 4$ based on the >100 deg^2 area," *PASJ*, vol. 70, p. S12, Jan. 2018.

[175] A. A. Dutton, F. C. van den Bosch, and A. Dekel, "On the origin of the galaxy star-formation-rate sequence: evolution and scatter," *MNRAS*, vol. 405, pp. 1690–1710, Jul. 2010.

[176] E. A. Cooke, N. A. Hatch, S. I. Muldrew, E. E. Rigby, and J. D. Kurk, "A $z = 2.5$ protocluster associated with the radio galaxy MRC 2104-242: star formation and differing mass functions in dense environments," *MNRAS*, vol. 440, pp. 3262–3274, Jun. 2014.

[177] C. Laigle, H. J. McCracken, O. Ilbert, B. C. Hsieh, I. Davidzon, P. Capak, G. Hasinger, J. D. Silverman, C. Pichon, J. Coupon, H. Aussel, D. Le Borgne, K. Caputi, P. Cassata, Y.-Y. Chang, F. Civano, J. Dunlop, J. Fynbo, J. S. Kartaltepe, A. Koekemoer, O. Le Fèvre, E. Le Floc'h, A. Leauthaud, S. Lilly, L. Lin, S. Marchesi, B. Milvang-Jensen, M. Salvato, D. B. Sanders, N. Scoville, V. Smolcic, M. Stockmann, Y. Taniguchi, L. Tasca, S. Toft, M. Vaccari, and J. Zabl, "The COSMOS2015 Catalog: Exploring the $1 < z < 6$ Universe with Half a Million Galaxies," *ApJS*, vol. 224, p. 24, Jun. 2016.

[178] Y. Koyama, T. Kodama, K.-i. Tadaki, M. Hayashi, I. Tanaka, and R. Shimakawa, "The Environmental Impacts on the Star Formation Main Sequence: An Hα Study of the Newly Discovered Rich Cluster at $z = 1.52$," *ApJ*, vol. 789, p. 18, Jul. 2014.

[179] G. Erfanianfar, P. Popesso, A. Finoguenov, D. Wilman, S. Wuyts, A. Biviano, M. Salvato, M. Mirkazemi, L. Morselli, F. Ziparo, K. Nandra, D. Lutz, D. Elbaz, M. Dickinson, M. Tanaka, M. B. Altieri, H. Aussel, F. Bauer, S. Berta, R. M. Bielby, N. Brandt, N. Cappelluti, A. Cimatti, M. C. Cooper, D. Fadda, O. Ilbert, E. Le Floch, B. Magnelli, J. S. Mulchaey, R. Nordon, J. A. Newman, A. Poglitsch, and F. Pozzi, "Non-linearity and environmental dependence of the star-forming galaxies main sequence," *MNRAS*, vol. 455, pp. 2839–2851, Jan. 2016.

[180] R. A. Overzier, R. J. Bouwens, N. J. G. Cross, B. P. Venemans, G. K. Miley, A. W. Zirm, N. Benítez, J. P. Blakeslee, D. Coe, R. Demarco, H. C. Ford, N. L. Homeier, G. D. Illingworth, J. D. Kurk, A. R. Martel, S. Mei, I. Oliveira, H. J. A. Röttgering, Z. I. Tsvetanov, and W. Zheng, "Lyman Break Galaxies, Lyα Emitters, and a Radio Galaxy in a Protocluster at z = 4.1," *ApJ*, vol. 673, pp. 143–162, Jan. 2008.

[181] C. M. Casey, A. Cooray, P. Capak, H. Fu, K. Kovac, S. Lilly, D. B. Sanders, N. Z. Scoville, and E. Treister, "A Massive, Distant Proto-cluster at z = 2.47 Caught in a Phase of Rapid Formation?" *ApJL*, vol. 808, p. L33, Aug. 2015.

[182] A. Kenter, S. S. Murray, W. R. Forman, C. Jones, P. Green, C. S. Kochanek, A. Vikhlinin, D. Fabricant, G. Fazio, K. Brand, M. J. I. Brown, A. Dey, B. T. Jannuzi, J. Najita, B. McNamara, J. Shields, and M. Rieke, "XBootes: An X-Ray Survey of the NDWFS Bootes Field. II. The X-Ray Source Catalog," *ApJS*, vol. 161, pp. 9–20, Nov. 2005.

[183] K. J. Duncan, M. J. Jarvis, M. J. I. Brown, and H. J. A. Röttgering, "Photometric redshifts for the next generation of deep radio continuum surveys - II. Gaussian processes and hybrid estimates," *MNRAS*, vol. 477, pp. 5177–5190, Jul. 2018.

[184] K. J. Duncan, M. J. I. Brown, W. L. Williams, P. N. Best, V. Buat, D. Burgarella, M. J. Jarvis, K. Małek, S. J. Oliver, H. J. A. Röttgering, and D. J. B. Smith, "Photometric redshifts for the next generation of deep radio continuum surveys - I. Template fitting," *MNRAS*, vol. 473, pp. 2655–2672, Jan. 2018.

[185] W. H. de Vries, R. Morganti, H. J. A. Röttgering, R. Vermeulen, W. van Breugel, R. Rengelink, and M. J. Jarvis, "Deep Westerbork 1.4 GHz Imaging of the Bootes Field," *AJ*, vol. 123, pp. 1784–1800, Mar. 2002.

[186] T. A. Marriage, V. Acquaviva, P. A. R. Ade, P. Aguirre, M. Amiri, J. W. Appel, L. F. Barrientos, E. S. Battistelli, J. R. Bond, B. Brown, B. Burger, J. Chervenak, S. Das, M. J. Devlin, S. R. Dicker, W. Bertrand Doriese, J. Dunkley, R. Dünner, T. Essinger-Hileman, R. P. Fisher, J. W. Fowler, A. Hajian, M. Halpern, M. Hasselfield, C. Hernández-Monteagudo, G. C. Hilton, M. Hilton, A. D. Hincks, R. Hlozek, K. M. Huffenberger, D. Handel Hughes, J. P. Hughes, L. Infante, K. D. Irwin, J. Baptiste Juin, M. Kaul, J. Klein, A. Kosowsky, J. M. Lau, M. Limon, Y.-T. Lin, R. H. Lupton, D. Marsden, K. Martocci, P. Mauskopf, F. Menanteau, K. Moodley, H. Moseley, C. B. Netterfield, M. D. Niemack, M. R. Nolta, L. A. Page, L. Parker, B. Partridge, H. Quintana, E. D. Reese, B. Reid, N. Sehgal, B. D. Sherwin, J. Sievers, D. N. Spergel, S. T. Staggs, D. S. Swetz, E. R. Switzer, R. Thornton, H. Trac, C. Tucker, R. Warne, G. Wilson, E. Wollack, and Y. Zhao, "The Atacama Cosmology Telescope: Sunyaev-Zel'dovich-Selected Galaxy Clusters at 148 GHz in the 2008 Survey," *ApJ*, vol. 737, p. 61, Aug. 2011.

[187] J. Einasto, M. Einasto, S. Gottlöber, V. Müller, V. Saar, A. A. Starobinsky, E. Tago, D. Tucker, H. Andernach, and P. Frisch, "A 120-Mpc periodicity in the three-dimensional distribution of galaxy superclusters," *Nature*, vol. 385, pp. 139–141, Jan 1997.

[188] M. Einasto, H. Lietzen, E. Tempel, M. Gramann, L. J. Liivamägi, and J. Einasto, "SDSS superclusters: morphology and galaxy content," *A&A*, vol. 562, p. A87, Feb. 2014.

[189] N. Visvanathan and A. Sandage, "The color-absolute magnitude relation for E and S0 galaxies. I - Calibration and tests for universality using Virgo and eight other nearby clusters," *ApJ*, vol. 216, pp. 214–226, Aug. 1977.

[190] R. G. Bower, J. R. Lucey, and R. S. Ellis, "Precision Photometry of Early Type Galaxies in the Coma and Virgo Clusters - a Test of the Universality of the Colour / Magnitude Relation - Part Two - Analysis," *MNRAS*, vol. 254, p. 601, Feb. 1992.

[191] S. Alberts, A. Pope, M. Brodwin, D. W. Atlee, Y.-T. Lin, A. Dey, P. R. M. Eisenhardt, D. P. Gettings, A. H. Gonzalez, B. T. Jannuzi, C. L. Mancone, J. Moustakas, G. F. Snyder, S. A. Stanford, D. Stern, B. J. Weiner, and G. R. Zeimann, "The evolution of dust-obscured star formation activity in galaxy clusters relative to the field over the last 9 billion years," *MNRAS*, vol. 437, pp. 437–457, Jan. 2014.

[192] B. C. Lemaux, A. R. Tomczak, L. M. Lubin, R. R. Gal, L. Shen, D. Pelliccia, P.-F. Wu, D. Hung, S. Mei, O. Le Fèvre, N. Rumbaugh, D. D. Kocevski, and G. K. Squires, "Persistence of the Color-Density Relation and Efficient Environmental Quenching to $z \sim 1.4$," *arXiv e-prints*, Dec. 2018.

[193] J. Toshikawa, H. Uchiyama, N. Kashikawa, M. Ouchi, R. Overzier, Y. Ono, Y. Harikane, S. Ishikawa, T. Kodama, Y. Matsuda, Y.-T. Lin, M. Onoue, M. Tanaka, T. Nagao, M. Akiyama, Y. Komiyama, T. Goto, and C.-H. Lee, "GOLDRUSH. III. A systematic search for protoclusters at z ~ 4 based on the >100 deg^2 area," *PASJ*, vol. 70, p. S12, Jan. 2018.

[194] L. Pentericci, J. D. Kurk, H. J. A. Röttgering, G. K. Miley, W. van Breugel, C. L. Carilli, H. Ford, T. Heckman, P. McCarthy, and A. Moorwood, "A search for clusters at high redshift. II. A proto cluster around a radio galaxy at z=2.16," *A&A*, vol. 361, pp. L25–L28, Sep. 2000.

[195] E. Kuiper, N. A. Hatch, B. P. Venemans, G. K. Miley, H. J. A. Röttgering, J. D. Kurk, R. A. Overzier, L. Pentericci, J. Bland-Hawthorn, and J. Cepa, "Discovery of a high-z protocluster with tunable filters: the case of 6C0140+326 at z= 4.4," *MNRAS*, vol. 417, pp. 1088–1097, Oct. 2011.

[196] K. Mawatari, T. Yamada, Y. Nakamura, T. Hayashino, and Y. Matsuda, "Characterization of the Distribution of the Lyα Emitters in the 53w002 Field at z = 2.4," *ApJ*, vol. 759, p. 133, Nov. 2012.

[197] Y. Yang, A. Zabludoff, D. Eisenstein, and R. Davé, "Strong Field-to-field Variation of Lyα Nebulae Populations at z ˜= 2.3," *ApJ*, vol. 719, pp. 1654–1671, Aug. 2010.

[198] R. Higuchi, M. Ouchi, Y. Ono, T. Shibuya, J. Toshikawa, Y. Harikane, T. Kojima, Y.-K. Chiang, E. Egami, N. Kashikawa, R. Overzier, A. Konno, A. K. Inoue, K. Hasegawa, S. Fujimoto, T. Goto, S. Ishikawa, K. Ito, Y. Komiyama, and M. Tanaka, "SILVERRUSH. VII. Subaru/HSC Identifications of 42 Protocluster Candidates at z $\sim$6-7 with the Spectroscopic Redshifts up to z=6.574: Implications for Cosmic Reionization," *arXiv e-prints*, p. arXiv:1801.00531, Jan 2018.

[199] S. D. J. Gwyn, "The Canada-France-Hawaii Telescope Legacy Survey: Stacked Images and Catalogs," *AJ*, vol. 143, p. 38, Feb. 2012.

[200] E. Bertin and S. Arnouts, "SExtractor: Software for source extraction." *A&AS*, vol. 117, pp. 393–404, Jun. 1996.

[201] P. Madau, "Radiative transfer in a clumpy universe: The colors of high-redshift galaxies," *ApJ*, vol. 441, pp. 18–27, Mar. 1995.

[202] I. Oteo, A. Bongiovanni, A. M. Pérez García, J. Cepa, A. Ederoclite, M. Sánchez-Portal, I. Pintos-Castro, R. Pérez-Martínez, S. Berta, B. Magnelli, P. Popesso, F. Pozzi, A. Poglitsch, D. Lutz, R. Genzel, L. Tacconi, N. Förster Schreiber, E. Sturm, D. Elbaz, H. Aussel, E. Daddi, P. Andreani, A. Cimatti, R. Maiolino, B. Altieri, and I. Valtchanov, "Herschel-PACS far-infrared detections of Lyman-α emitters at $2.0 < z < 3.5$," *A&A*, vol. 541, p. A65, May 2012.

[203] C. R. Bridge, A. Blain, C. J. K. Borys, S. Petty, D. Benford, P. Eisenhardt, D. Farrah, R. L. Griffith, T. Jarrett, C. Lonsdale, S. A. Stanford, D. Stern, C.-W. Tsai, E. L. Wright, and J. Wu, "A New Population of High-z, Dusty Lyα Emitters and Blobs Discovered by WISE: Feedback Caught in the Act?" *ApJ*, vol. 769, p. 91, Jun. 2013.

[204] D. W. Hogg, J. G. Cohen, R. Blandford, and M. A. Pahre, "The O II Luminosity Density of the Universe," *ApJ*, vol. 504, pp. 622–628, Sep. 1998.

[205] R. Ciardullo, C. Gronwall, J. J. Adams, G. A. Blanc, K. Gebhardt, S. L. Finkelstein, S. Jogee, G. J. Hill, N. Drory, U. Hopp, D. P. Schneider, G. R. Zeimann, and G. B. Dalton, "The HETDEX Pilot Survey. IV. The Evolution of [O II] Emitting Galaxies from z ˜ 0.5 to z ˜ 0," *ApJ*, vol. 769, p. 83, May 2013.

[206] E. Gawiser, P. G. van Dokkum, C. Gronwall, R. Ciardullo, G. A. Blanc, F. J. Castander, J. Feldmeier, H. Francke, M. Franx, L. Haberzettl, D. Herrera, T. Hickey, L. Infante, P. Lira, J. Maza, R. Quadri, A. Richardson, K. Schawinski, M. Schirmer, E. N. Taylor, E. Treister, C. M. Urry, and S. N. Virani, "The Physical Nature of Lyα-emitting Galaxies at z=3.1," *ApJL*, vol. 642, pp. L13–L16, May 2006.

[207] M. Ouchi, K. Shimasaku, M. Akiyama, C. Simpson, T. Saito, Y. Ueda, H. Furusawa, K. Sekiguchi, T. Yamada, T. Kodama, N. Kashikawa, S. Okamura, M. Iye, T. Takata, M. Yoshida, and M. Yoshida, "The Subaru/XMM-Newton Deep Survey (SXDS). IV. Evolution of Lyα Emitters from z = 3.1 to 5.7 in the 1 deg^2 Field: Luminosity Functions and AGN," *ApJS*, vol. 176, pp. 301–330, Jun. 2008.

[208] Z. Y. Zheng, J. X. Wang, S. L. Finkelstein, S. Malhotra, J. E. Rhoads, and K. D. Finkelstein, "X-ray Properties of the z ˜ 4.5 Lyα Emitters in the Chandra Deep Field South Region," *ApJ*, vol. 718, pp. 52–59, Jul. 2010.

[209] D. Sobral, S. Santos, J. Matthee, A. Paulino-Afonso, B. Ribeiro, J. Calhau, and A. A. Khostovan, "Slicing COSMOS with SC4K: the evolution of typical Ly α emitters and the Ly α escape fraction from z ~ 2 to 6," *MNRAS*, vol. 476, pp. 4725–4752, Jun. 2018.

[210] L. Chiappetti, M. Tajer, G. Trinchieri, D. Maccagni, L. Maraschi, L. Paioro, M. Pierre, J. Surdej, O. Garcet, E. Gosset, O. Le Fèvre, E. Bertin, H. J. McCracken, Y. Mellier, S. Foucaud, M. Radovich, V. Ripepi, and M. Arnaboldi, "The XMM-LSS survey. The XMDS/VVDS 4σ catalogue," *A&A*, vol. 439, pp. 413–425, Aug. 2005.

[211] O. Le Fèvre, P. Cassata, O. Cucciati, B. Garilli, O. Ilbert, V. Le Brun, D. Maccagni, C. Moreau, M. Scodeggio, L. Tresse, G. Zamorani, C. Adami, S. Arnouts, S. Bardelli, M. Bolzonella, M. Bondi, A. Bongiorno, D. Bottini, A. Cappi, S. Charlot, P. Ciliegi, T. Contini, S. de la Torre, S. Foucaud, P. Franzetti, I. Gavignaud, L. Guzzo, A. Iovino, B. Lemaux, C. López-Sanjuan, H. J. McCracken, B. Marano, C. Marinoni, A. Mazure, Y. Mellier, R. Merighi, P. Merluzzi, S. Paltani, R. Pellò, A. Pollo, L. Pozzetti, R. Scaramella, L. Tasca, D. Vergani, G. Vettolani, A. Zanichelli, and E. Zucca, "The VIMOS VLT Deep Survey final data release: a spectroscopic sample of 35 016 galaxies and AGN out to z ˜ 6.7 selected with $17.5 < i_{AB} < 24.75$," *A&A*, vol. 559, p. A14, Nov. 2013.

[212] D. E. Vanden Berk, G. T. Richards, A. Bauer, M. A. Strauss, D. P. Schneider, T. M. Heckman, D. G. York, P. B. Hall, X. Fan, G. R. Knapp, S. F. Anderson, J. Annis, N. A. Bahcall, M. Bernardi, J. W. Briggs, J. Brinkmann, R. Brunner, S. Burles, L. Carey, F. J. Castander, A. J. Connolly, J. H. Crocker, I. Csabai, M. Doi, D. Finkbeiner, S. Friedman, J. A. Frieman, M. Fukugita, J. E. Gunn, G. S. Hennessy, Ž. Ivezić, S. Kent, P. Z. Kunszt, D. Q. Lamb, R. F. Leger, D. C. Long, J. Loveday, R. H. Lupton, A. Meiksin, A. Merelli, J. A. Munn, H. J. Newberg, M. Newcomb, R. C. Nichol, R. Owen, J. R. Pier, A. Pope, C. M. Rockosi, D. J. Schlegel, W. A. Siegmund, S. Smee, Y. Snir, C. Stoughton, C. Stubbs, M. SubbaRao, A. S. Szalay, G. P. Szokoly, C. Tremonti, A. Uomoto, P. Waddell, B. Yanny, and W. Zheng, "Composite Quasar Spectra from the Sloan Digital Sky Survey," *AJ*, vol. 122, pp. 549–564, Aug. 2001.

[213] O. Le Fèvre, L. A. M. Tasca, P. Cassata, B. Garilli, V. Le Brun, D. Maccagni, L. Pentericci, R. Thomas, E. Vanzella, G. Zamorani, E. Zucca, R. Amorin, S. Bardelli, P. Capak, L. Cassarà, M. Castellano, A. Cimatti, J. G. Cuby, O. Cucciati, S. de la Torre, A. Durkalec, A. Fontana, M. Giavalisco, A. Grazian, N. P. Hathi, O. Ilbert, B. C. Lemaux, C. Moreau, S. Paltani, B. Ribeiro, M. Salvato, D. Schaerer, M. Scodeggio, V. Sommariva, M. Talia, Y. Taniguchi, L. Tresse, D. Vergani, P. W. Wang, S. Charlot, T. Contini, S. Fotopoulou, C. López-Sanjuan, Y. Mellier, and N. Scoville, "The VIMOS Ultra-Deep Survey: $\sim$10 000 galaxies with spectroscopic redshifts to study galaxy assembly at early epochs $2 < z < 6$," *A&A*, vol. 576, p. A79, Apr. 2015.

[214] G. D. Coleman, C.-C. Wu, and D. W. Weedman, "Colors and magnitudes predicted for high redshift galaxies," *ApJS*, vol. 43, pp. 393–416, Jul. 1980.

[215] P. Palunas, H. I. Teplitz, P. J. Francis, G. M. Williger, and B. E. Woodgate, "The Distribution of Lyα-Emitting Galaxies at z=2.38," *ApJ*, vol. 602, pp. 545–554, Feb. 2004.

[216] C. J. Lonsdale, H. E. Smith, M. Rowan-Robinson, J. Surace, D. Shupe, C. Xu, S. Oliver, D. Padgett, F. Fang, T. Conrow, A. Franceschini, N. Gautier, M. Griffin, P. Hacking, F. Masci, G. Morrison, J. O'Linger, F. Owen, I. Pérez-Fournon, M. Pierre, R. Puetter, G. Stacey, S. Castro, M. d. C. Polletta, D. Farrah, T. Jarrett, D. Frayer, B. Siana, T. Babbedge, S. Dye, M. Fox, E. Gonzalez-Solares, M. Salaman, S. Berta, J. J. Condon, H. Dole, and S. Serjeant, "SWIRE: The SIRTF Wide-Area Infrared Extragalactic Survey," *PASP*, vol. 115, pp. 897–927, Aug. 2003.

[217] J.-C. Mauduit, M. Lacy, D. Farrah, J. A. Surace, M. Jarvis, S. Oliver, C. Maraston, M. Vaccari, L. Marchetti, G. Zeimann, E. A. Gonzáles-Solares, J. Pforr, A. O. Petric, B. Henriques, P. A. Thomas, J. Afonso, A. Rettura, G. Wilson, J. T. Falder, J. E. Geach, M. Huynh, R. P. Norris, N. Seymour, G. T. Richards, S. A. Stanford, D. M. Alexander, R. H. Becker, P. N. Best, L. Bizzocchi, D. Bonfield, N. Castro, A. Cava, S. Chapman, N. Christopher, D. L. Clements, G. Covone, N. Dubois, J. S. Dunlop, E. Dyke, A. Edge, H. C. Ferguson, S. Foucaud, A. Franceschini, R. R. Gal, J. K. Grant, M. Grossi, E. Hatziminaoglou, S. Hickey, J. A. Hodge, J.-S. Huang, R. J. Ivison, M. Kim, O. LeFevre, M. Lehnert, C. J. Lonsdale, L. M. Lubin, R. J. McLure, H. Messias, A. Martínez-Sansigre, A. M. J. Mortier, D. M. Nielsen, M. Ouchi, G. Parish, I. Perez-Fournon, M. Pierre, S. Rawlings, A. Readhead, S. E. Ridgway, D. Rigopoulou, A. K. Romer, I. G. Rosebloom, H. J. A. Rottgering, M. Rowan-Robinson, A. Sajina, C. J. Simpson, I. Smail, G. K. Squires, J. A. Stevens, R. Taylor, M. Trichas, T. Urrutia, E. van Kampen, A. Verma, and C. K. Xu, "The Spitzer Extragalactic Representative Volume Survey (SERVS): Survey Definition and Goals," *PASP*, vol. 124, p. 714, Jul. 2012.

[218] C. C. Steidel, M. Bogosavljević, A. E. Shapley, J. A. Kollmeier, N. A. Reddy, D. K. Erb, and M. Pettini, "Diffuse Lyα Emitting Halos: A Generic Property of High-redshift Star-forming Galaxies," *ApJ*, vol. 736, p. 160, Aug. 2011.

[219] D. K. Erb, M. Bogosavljević, and C. C. Steidel, "Filamentary Large-scale Structure Traced by Six Lyα Blobs at z = 2.3," *ApJL*, vol. 740, p. L31, Oct. 2011.

[220] C. Gronwall, R. Ciardullo, T. Hickey, E. Gawiser, J. J. Feldmeier, P. G. van Dokkum, C. M. Urry, D. Herrera, B. D. Lehmer, L. Infante, A. Orsi, D. Marchesini, G. A. Blanc, H. Francke, P. Lira, and E. Treister, "Lyα Emission-Line Galaxies at z = 3.1 in the Extended Chandra Deep Field-South," *ApJ*, vol. 667, pp. 79–91, Sep. 2007.

[221] J. D. Kurk, H. J. A. Röttgering, L. Pentericci, G. K. Miley, W. van Breugel, C. L. Carilli, H. Ford, T. Heckman, P. McCarthy, and A. Moorwood, "A Search for clusters at high redshift. I. Candidate Lyalpha emitters near 1138-262 at z=2.2," *A&A*, vol. 358, pp. L1–L4, Jun. 2000.

[222] B. P. Venemans, J. D. Kurk, G. K. Miley, H. J. A. Röttgering, W. van Breugel, C. L. Carilli, C. De Breuck, H. Ford, T. Heckman, P. McCarthy, and L. Pentericci, "The Most Distant Structure of Galaxies Known: A Protocluster at z=4.1," *ApJL*, vol. 569, pp. L11–L14, Apr. 2002.

[223] A. E. Shapley, C. C. Steidel, M. Pettini, and K. L. Adelberger, "Rest-Frame Ultraviolet Spectra of z˜3 Lyman Break Galaxies," *ApJ*, vol. 588, pp. 65–89, May 2003.

[224] K. Shi, K.-S. Lee, A. Dey, Y. Huang, N. Malavasi, C.-L. Hung, H. Inami, M. Ashby, K. Duncan, R. Xue, N. Reddy, S. Hong, B. T. Jannuzi, M. C. Cooper, A. H. Gonzalez, H. J. A. Röttgering, P. N. Best, and C. Tasse, "A Census of Galaxy Constituents in a Coma Progenitor Observed at z>3," *ApJ*, vol. 871, p. 83, Jan. 2019.

[225] S. L. Finkelstein, G. J. Hill, K. Gebhardt, J. Adams, G. A. Blanc, C. Papovich, R. Ciardullo, N. Drory, E. Gawiser, C. Gronwall, D. P. Schneider, and K.-V. Tran, "The HETDEX Pilot Survey. III. The Low Metallicities of High-redshift Lyα Galaxies," *ApJ*, vol. 729, p. 140, Mar. 2011.

[226] K. Nakajima, M. Ouchi, K. Shimasaku, T. Hashimoto, Y. Ono, and J. C. Lee, "First Spectroscopic Evidence for High Ionization State and Low Oxygen Abundance in Lyα Emitters," *ApJ*, vol. 769, p. 3, May 2013.

[227] M. Song, S. L. Finkelstein, K. Gebhardt, G. J. Hill, N. Drory, M. L. N. Ashby, G. A. Blanc, J. Bridge, T. Chonis, R. Ciardullo, M. Fabricius, G. G. Fazio, E. Gawiser, C. Gronwall, A. Hagen, J.-S. Huang, S. Jogee, R. Livermore, B. Salmon, D. P. Schneider, S. P. Willner, and G. R. Zeimann, "The HETDEX Pilot Survey. V. The Physical Origin of Lyα Emitters Probed by Near-infrared Spectroscopy," *ApJ*, vol. 791, p. 3, Aug. 2014.

[228] R. Bielby, M. D. Hill, T. Shanks, N. H. M. Crighton, L. Infante, C. G. Bornancini, H. Francke, P. Héraudeau, D. G. Lambas, N. Metcalfe, D. Minniti, N. Padilla, T. Theuns, P. Tummuangpak, and P. Weilbacher, "The VLT LBG Redshift Survey - III. The clustering and dynamics of Lyman- break galaxies at z 3," *MNRAS*, vol. 430, pp. 425–449, Mar. 2013.

[229] R. C. Kennicutt, Jr., "Star Formation in Galaxies Along the Hubble Sequence," *Annual Review of Astronomy and Astrophysics*, vol. 36, pp. 189–232, 1998.

[230] C. Marinoni, M. Davis, J. A. Newman, and A. L. Coil, "Three-dimensional Identification and Reconstruction of Galaxy Systems within Flux-limited Redshift Surveys," *ApJ*, vol. 580, pp. 122–143, Nov. 2002.

[231] M. C. Cooper, J. A. Newman, D. S. Madgwick, B. F. Gerke, R. Yan, and M. Davis, "Measuring Galaxy Environments with Deep Redshift Surveys," *ApJ*, vol. 634, pp. 833–848, Dec. 2005.

[232] Y.-T. Lin and J. J. Mohr, "K-band Properties of Galaxy Clusters and Groups: Brightest Cluster Galaxies and Intracluster Light," *ApJ*, vol. 617, pp. 879–895, Dec. 2004.

[233] R. Bielby, P. Hudelot, H. J. McCracken, O. Ilbert, E. Daddi, O. Le Fèvre, V. Gonzalez-Perez, J.-P. Kneib, C. Marmo, Y. Mellier, M. Salvato, D. B. Sanders, and C. J. Willott, "The WIRCam Deep Survey. I. Counts, colours, and mass-functions derived from near-infrared imaging in the CFHTLS deep fields," *A&A*, vol. 545, p. A23, Sep. 2012.

[234] G. Bruzual and S. Charlot, "Stellar population synthesis at the resolution of 2003," *MNRAS*, vol. 344, pp. 1000–1028, Oct. 2003.

[235] P. G. van Dokkum, N. M. Förster Schreiber, M. Franx, E. Daddi, G. D. Illingworth, I. Labbé, A. Moorwood, H.-W. Rix, H. Röttgering, G. Rudnick, A. van der Wel, P. van der Werf, and L. van Starkenburg, "Spectroscopic Confirmation of a Substantial Population of Luminous Red Galaxies at Redshifts z>˜2," *ApJL*, vol. 587, pp. L83–L87, Apr. 2003.

[236] M. Bondi, P. Ciliegi, G. Zamorani, L. Gregorini, G. Vettolani, P. Parma, H. de Ruiter, O. Le Fevre, M. Arnaboldi, L. Guzzo, D. Maccagni, R. Scaramella, C. Adami, S. Bardelli, M. Bolzonella, D. Bottini, A. Cappi, S. Foucaud, P. Franzetti, B. Garilli, S. Gwyn, O. Ilbert, A. Iovino, V. Le Brun, B. Marano, C. Marinoni, H. J. McCracken, B. Meneux, A. Pollo, L. Pozzetti, M. Radovich, V. Ripepi, D. Rizzo, M. Scodeggio, L. Tresse, A. Zanichelli, and E. Zucca, "The VLA-VIRMOS Deep Field. I. Radio observations probing the mu Jy source population," *A&A*, vol. 403, pp. 857–867, Jun. 2003.

[237] J. Fritz, A. Franceschini, and E. Hatziminaoglou, "Revisiting the infrared spectra of active galactic nuclei with a new torus emission model," *MNRAS*, vol. 366, pp. 767–786, Mar. 2006.

[238] L. Gao, V. Springel, and S. D. M. White, "The age dependence of halo clustering," *MNRAS*, vol. 363, pp. L66–L70, Oct. 2005.

[239] R. H. Wechsler, A. R. Zentner, J. S. Bullock, A. V. Kravtsov, and B. Allgood, "The Dependence of Halo Clustering on Halo Formation History, Concentration, and Occupation," *ApJ*, vol. 652, pp. 71–84, Nov. 2006.

[240] Y. Li, H. J. Mo, and L. Gao, "On halo formation times and assembly bias," *MNRAS*, vol. 389, pp. 1419–1426, Sep. 2008.

[241] A. R. Zentner, A. P. Hearin, and F. C. van den Bosch, "Galaxy assembly bias: a significant source of systematic error in the galaxy-halo relationship," *MNRAS*, vol. 443, pp. 3044–3067, Oct. 2014.

[242] M. K. M. Prescott, A. Dey, M. Brodwin, F. H. Chaffee, V. Desai, P. Eisenhardt, E. Le Floc'h, B. T. Jannuzi, N. Kashikawa, Y. Matsuda, and B. T. Soifer, "Resolving the Galaxies within a Giant Lyα Nebula: Witnessing the Formation of a Galaxy Group?" *ApJ*, vol. 752, p. 86, Jun. 2012.

[243] Y. Yang, A. Zabludoff, K. Jahnke, D. Eisenstein, R. Davé, S. A. Shectman, and D. D. Kelson, "Gas Kinematics in Lyα Nebulae," *ApJ*, vol. 735, p. 87, Jul. 2011.

[244] Y. Yang, A. Zabludoff, K. Jahnke, and R. Davé, "The Properties of Lyα Nebulae: Gas Kinematics from Nonresonant Lines," *ApJ*, vol. 793, p. 114, Oct. 2014.